



TECHNISCHE  
UNIVERSITÄT  
WIEN

DISSERTATION

# Growth and characterization of (doped) calcium fluoride crystals for the nuclear spectroscopy of Th-229

ausgeführt zum Zwecke der Erlangung des akademischen Grades  
eines Doktors der Naturwissenschaften

unter der Leitung von  
Univ.Prof. Dr. Thorsten Schumm  
Atominstitut (E141)

eingereicht an der  
Technischen Universität Wien  
Fakultät für Physik

von

**DI Matthias Schreitl**  
Matrikelnummer 0325847

Wien, Mai 2016

---

M. Schreitl



# Contents

<b>Zusammenfassung</b>	<b>V</b>
<b>Abstract</b>	<b>VII</b>
<b>Acknowledgements</b>	<b>IX</b>
<b>1 Introduction</b>	<b>1</b>
1.1 The isomeric transition of $^{229}\text{Th}$	1
1.2 Possible application: a nuclear clock with $^{229}\text{Th}$	2
1.3 Experimental search for the isomeric transition of $^{229}\text{Th}$	4
1.3.1 Ion traps	4
1.3.2 Recoil nuclei	5
1.3.3 The solid-state approach: $^{229}\text{Th}$ implanted in a crystal	5
Broadenings and shifts of the isomeric transition in $\text{CaF}_2$	7
<b>2 Growth of (doped) calcium fluoride crystals</b>	<b>11</b>
2.1 Crystal growth from the melt: a general introduction	11
2.1.1 Crystal growth in crucibles	13
Vertical gradient freeze method (Tammann-Stöber method)	14
Bridgman-Stockbarger method	15
2.1.2 Crystal pulling from the melt	15
Nacken-Kyropoulos method	16
Czochralski method (Cz)	16
2.1.3 Comparison of the growth methods	17
2.2 The Furnace: design and principle of operation	19
2.2.1 General requirements for the growth of small $\text{CaF}_2$ crystals	19
2.2.2 Requirements to the temperature field and the phase boundary	20
2.2.3 Numerical simulation	20
2.2.4 Thermal insulation	22
Temperature profile: experimental verification	24
Shape of the interface: experimental verification	24
2.2.5 Crucible	25
2.2.6 Heating and temperature control	26
Thermoelements	28
2.2.7 Vacuum	28
Possible leaks	29
Out-gasing	29

2.2.8	Process control . . . . .	29
	Software safety measures . . . . .	30
2.2.9	Data recording and analysis . . . . .	30
2.2.10	Hazards and safety measures . . . . .	31
2.3	Process steps in the calcium fluoride growth . . . . .	32
2.3.1	Process planning . . . . .	33
2.3.2	Preparation of the furnace and the raw material . . . . .	33
2.3.3	Drying . . . . .	33
2.3.4	Scavenger process: chemical removal of oxygen . . . . .	34
2.3.5	Homogenizing and seeding . . . . .	35
2.3.6	Crystal growth . . . . .	38
2.3.7	Cool-down . . . . .	39
2.4	Parameters for successful seeding . . . . .	39
<b>3</b>	<b>Doping CaF<sub>2</sub> crystals</b>	<b>45</b>
3.1	Thorium-doped CaF <sub>2</sub> crystals . . . . .	45
3.1.1	Theoretical predictions for Th:CaF <sub>2</sub> . . . . .	46
	Computer models . . . . .	46
	Modeling results . . . . .	47
3.1.2	Chemical preparation of <sup>229</sup> ThF <sub>4</sub> as a dopant . . . . .	51
3.2	Uranium-doped CaF <sub>2</sub> crystals . . . . .	53
3.2.1	Indirect excitation of the <sup>229</sup> Th isomeric state in a bulk crystal	53
3.2.2	Growth of U:CaF <sub>2</sub> crystals . . . . .	55
	Chemical preparation of UF <sub>4</sub> as a dopant . . . . .	55
	Grown U:CaF <sub>2</sub> crystals . . . . .	56
3.2.3	Challenges of the experimental approach . . . . .	57
3.3	Zirconium-doped CaF <sub>2</sub> crystals . . . . .	58
3.4	Cerium-doped CaF <sub>2</sub> crystals . . . . .	59
3.5	Experimental determination of the doping concentration . . . . .	59
3.5.1	Experimental methods . . . . .	60
	Inductively coupled plasma mass spectrometry (ICPMS) . . . . .	60
	Gamma spectroscopy . . . . .	60
	Neutron activation analysis (NAA) . . . . .	62
3.5.2	Results . . . . .	65
	Czochralski-grown <sup>232</sup> Th:CaF <sub>2</sub> . . . . .	65
	VGF-grown <sup>232</sup> Th:CaF <sub>2</sub> . . . . .	67
	VGF-grown <sup>229</sup> Th:CaF <sub>2</sub> . . . . .	71
	VGF-grown Zr:CaF <sub>2</sub> . . . . .	78
<b>4</b>	<b>Optical crystal characterization</b>	<b>79</b>
4.1	VUV Transmission . . . . .	79
4.1.1	Absorption . . . . .	80
	Oxygen-induced absorption . . . . .	81
4.1.2	Scattering . . . . .	83

4.1.3	Reflection . . . . .	83
4.1.4	Transmission of (doped) CaF <sub>2</sub> crystals between 120-190 nm	84
	Spectrometer setup . . . . .	84
	Transmission spectra between 120-190 nm . . . . .	86
4.1.5	Energy-dependent transmission of laser pulses around 160 nm	91
4.2	Luminescence . . . . .	95
4.2.1	Preliminary measurements with short high-power laser pulses at 160 nm . . . . .	95
4.2.2	Photoluminescence . . . . .	99
4.2.3	Radioluminescence . . . . .	100
	Thermoluminescence . . . . .	104
	Cherenkov radiation . . . . .	105
4.3	Spectrally narrow features with a long life-time . . . . .	108
<b>5</b>	<b>Conclusion &amp; outlook</b>	<b>111</b>
	<b>List of Figures</b>	<b>116</b>
	<b>Bibliography</b>	<b>126</b>



## Zusammenfassung

Thorium-229 bietet einen in der Natur einzigartigen niederenergetischen Kernübergang. Das Isomer, d.h. der angeregte Zustand des Übergangs, liegt nur einige wenige eV über dem Grundzustand und macht somit Methoden aus der Atomphysik, wie Laseranregung, auf die Kernspektroskopie anwendbar. Man geht aktuell von einer Isomerenergie von  $7.8 \pm 0.5$  eV aus, was dem Wellenlängenbereich von 150 – 170 nm im Vakuum-Ultraviolett entspricht. Dieser Wert wurde indirekt mittels Gammaspektroskopie ermittelt, aber sowohl eine direkte Anregung des isomerischen Übergangs als auch die Detektion der photonischen Abregung des Isomers steht noch aus. Die Lebenszeit des Isomers hängt stark vom Ladungszustand und der chemischen Umgebung des  $^{229}\text{Th}$ -Atoms (Ions) ab. Abschätzungen für einen isolierten Atomkern ergeben Lebenszeiten von einigen 1000 Sekunden, was einer natürlichen Linienbreite im Millihertz-Bereich entspricht. Mögliche Anwendung des isomerischen Übergangs umfassen eine optische Atomkernuhr mit bisher unerreichter Präzision, optische Gammalaser und die Messung möglicher Variationen von Fundamentalkonstanten mit höchster Genauigkeit.

Die Ionisierungsenergie des neutralen Thorium-Atoms ist niedriger als die erwartete Energie des Isomers. Experimente müssen aus diesem Grund mit dem Ion durchgeführt werden. Unser experimenteller Ansatz gründet auf dem Einbau von  $\text{Th}^{4+}$  in das Ionengitter von Calciumfluorid-Kristallen, wo es ein  $\text{Ca}^{2+}$ -Ion ersetzt.  $\text{CaF}_2$  bietet ein kubisches Kristallgitter und eine UV-Transparenz hinunter bis 125 nm. Der Einbau einer großen Zahl an Thorium-Atomen ( $> 10^{14}$ ) ist im Vergleich zu Ionenfallen möglich, wodurch die spektroskopische Suche nach dem Kernübergang erheblich erleichtert wird. Numerische Kristallmodelle wurden angewendet, um die chemische Umgebung des Dotierungsstoffes im Kristall und die Auswirkungen des Dotierungsstoffes auf die Bandlücke zu bestimmen. Die UV-Transparenz wird laut diesen Simulationen nur geringfügig verringert, was ein weiteres Indiz für die Durchführbarkeit des experimentellen Ansatzes liefert.

Im Zuge dieser Arbeit wurde eine Kristallzüchtungsanlage zur Herstellung kleiner, hoch-dotierter Calciumfluorid-Kristalle entwickelt. Das vertical gradient freeze Verfahren, bei dem ein Temperaturgradient entlang der vertikalen Achse des Züchtungstiegels eingestellt wird, fand dabei Anwendung. Das Rohmaterial für die Züchtung wird zuerst chemisch gereinigt, um Sauerstoffkontaminationen zu entfernen, und anschließend aufgeschmolzen. Als schwierigster Teil des Züchtungsprozesses erweist sich die Ankeimphase, bei der das komplette Calciumfluorid-Pulver, aber nur ein Teil des Keimkristalls geschmolzen werden soll. Genaue Temperatursteuerung erlaubt die kontrollierte Verschiebung der Phasengrenze,

um so den Kristall von unten nach oben wachsen zu lassen (“vertical gradient freeze”).

Hohe Dotierungskonzentrationen im Bereich von 0.1 – 1% wurden in Th:CaF<sub>2</sub> Kristallen realisiert. Absolute Konzentrationen und die Verteilung des Dotierungsstoffes konnten mittels Neutronaktivierungsanalyse und Gamma-spektroskopie bestimmt werden.

Mittels UV-Spektroskopie konnte gezeigt werden, dass Thorium-dotierte Calciumfluorid-Kristalle im UV-Bereich noch ausreichend transparent sind, was eine Kernanregung mittels Laser oder Synchrotron bzw. die Detektion des durch die Abregung des Isomers emittierten Gammaphotons ermöglicht. Diese Photonen müssen allerdings vom Radio- und Photoluminiszenz-Hintergrund unterschieden werden, welcher ebenfalls in dieser Arbeit charakterisiert und quantifiziert wurde.



## Abstract

Thorium-229 provides the unique feature of a nuclear transition with an exceptionally low energy. The isomer, i.e. the excited state of the transition, is predicted to be only a few eV above the ground state, making typical atomic physics tools like lasers applicable for nuclear spectroscopy. The currently most accepted value for the isomer energy is  $7.8 \pm 0.5$  eV, corresponding to wavelengths of 150 – 170 nm, in the vacuum-ultraviolet. This value was determined indirectly by gamma spectroscopy, but a direct excitation of the isomeric transition or the detection of the photonic deexcitation of the isomer is still pending. The isomer lifetime strongly depends on the charge state and chemical environment of the  $^{229}\text{Th}$  atom/ion, estimates for an isolated nucleus are on the order of a few 1000 s, providing a natural line width in the millihertz range. Possible applications are a nuclear optical clock with unprecedented stability, an optical gamma laser or a sensitive system for probing variations of fundamental constants.

The first ionization energy of the thorium atom is lower than the predicted transition energy, therefore it is necessary to work with ions. Our experimental approach consists in embedding  $\text{Th}^{4+}$  into the ionic crystal lattice of calcium fluoride where it replaces a  $\text{Ca}^{2+}$  ion.  $\text{CaF}_2$  provides a simple crystal structure and remains transparent in the UV region down to 125 nm. It allows doping with a large number of thorium atoms ( $> 10^{14}$ ) compared to ion traps, thereby facilitating a spectroscopic search for the nuclear transition. Numerical models have been applied to calculate the chemical environment around the thorium dopant site and how the band gap of calcium fluoride is affected by thorium doping. It is conjectured that the transparency window is only slightly reduced, validating the general approach.

In this thesis, a furnace for the growth of small-volume and highly-doped  $\text{CaF}_2$  crystals was developed. The vertical gradient freeze method, in which a temperature gradient is established along the vertical axis of the crucible, was applied for crystal growth. The raw material was first chemically purified, removing oxygen contaminants, and then molten. Seeding presented the most delicate part of the growth process. The  $\text{CaF}_2$  powder had to be molten without completely melting the seed crystal, which provided the orientation for the grown crystal. By precise temperature control in the furnace, the solid/liquid interface was slowly shifted upwards, thereby growing the crystal in the vertical direction.

High doping concentrations in the 0.1 – 1% range were demonstrated for  $\text{Th}:\text{CaF}_2$ . The absolute concentration and the distribution of the dopant in the crystals have

been determined by neutron activation analysis and gamma spectroscopy.

It was shown by UV spectroscopy that the thorium-doped  $\text{CaF}_2$  crystals remain sufficiently transparent in the UV region, making nuclear excitation by lasers or synchrotrons possible, as well as the detection of gamma photons emitted during deexcitation of the  $^{229}\text{Th}$  isomer. These photons have to be distinguished from the radio- and photoluminescence background, which was characterized and quantified in this work.

## Acknowledgements

Many people contributed to the completion of this thesis, in direct and indirect ways. Those mentioned here by name have provided scientific or otherwise life-enriching support (in many cases both!) and are representative of all of those who are not listed here but played important roles during my unforgettable years as a PhD-student.

First of all, I want to thank Professor Thorsten Schumm for his tremendous support that exceeded all expectations. He always had an open door for his students (and many others) and made lots of experiences possible that have significantly shaped my personal development, through conference visits, stays abroad as well as everyday discussions. The delicious and reliably provided Tuesday cake should not stay unmentioned here.

I also want to thank Professor Ekkehard Peik for agreeing to act as a secondary referee for this thesis. His scientific contribution has always been very much appreciated, by the entire thorium community as well as the participants (and especially the organizers) of the CoQuS Summer School 2013. Both, his lectures and the time (city walk) spent with the students shall be remembered.

I am much obliged to the Vienna Doctoral Program on Complex Quantum Systems (CoQuS) for the countless opportunities that broadened my scientific horizon and also those that enriched my life as a PhD student (e.g. get-togethers and retreats, especially the one at CERN). CoQuS provided encounters with scientists from all over the world as well as from (other) universities in Vienna, sometimes even laying the foundations for friendships beyond research networks. In addition to their everyday work, which is much appreciated, Christiane and Christina deserve special thanks for their support in organizing the already mentioned CoQuS Summer School 2013.

Of my co-workers, Georg, my loyal colleague, office-mate and friend, should be mentioned first since our paths already crossed during the first week of my diploma thesis and were intertwined ever since, a strong coupling that will hopefully continue in our post-thesis lives. I look back with gratitude at the time we spent together both inside and outside work. May we have many more journeys together, in good times and in bad.

A heart-felt thank you goes to Georgy, who also joined the Thorium team already in its early days and shared the office with Georg and me. This often implied being conveniently close (at least convenient for me) when questions arose. He has

always answered them patiently and extensively. I think the time we have spent together was a really good one and not just, as he says, “more or less OK”.

It was always a great pleasure to work or discuss with Simon Stellmer, who brought many new ideas with him and has shown great dedication to the Thorium team. When he joined the Thorium team, it was not only a great enrichment to our group (both on the professional as well as the personal level) but to the entire thorium community. Thank you, Simon, for your good work, especially for all the comprehensive explanations you provided, and also the times when we did not bother with physics.

A big thank you goes to all other present and former members of the Thorium team in Vienna: Veronika, Johannes, Enikő and Jozsef, Christoph, Pietro, Wolfgang, Maria, Alex, Jakob and Georg (Steinhauser). It was a great pleasure to work with you and to get to know you all.

The Atominstitut has become a second home over the years I have spent here, working on my Diploma as well as my PhD thesis. Some people, who are essential for things to function at the institute, should be mentioned here by name, standing representative for all the others who have provided such a pleasant (work) atmosphere: Michaela (Foster), Britta, Barbara (Stross), Ricki, Evi, Melissa, Zorica, Jan, Barbara (Fertl), Herbert (Diem), Herbert (Hartmann) and Günther.

I owe a great deal to many present and former members of the Atomchip group, my scientific home before moving one floor up (literally, not figuratively). I'm afraid that there are too many to mention them all without forgetting someone. We had joy, we had fun, we had all kinds of great things in the sun: whether it was ski mountaineering or climbing, for which it is so essential to have buddies you can rely on, or the process of exchanging all sorts of ideas that sustainably shaped all of our personalities. We have spent holidays together, climbing mountains or diving in coral reefs, but also had heated discussions in the lab, the coffee corner or the courtyard: it was a blast! The only slight regret I have, is that we did not introduce the *jour fixe* sooner. Last but not least, thank you for letting me use the fridge and the coffee machine.

At the Fraunhofer IISB in Erlangen, I received a very warm welcome by Kurt Semmelroth and Birgit Kallinger, who did not only introduce me to the art of crystal growing but also to their lovely city. After the furnace for crystal growth was transferred to Vienna, Kurt always took the time to answer my questions when we seemed to have reached a dead end with our experimental attempts. Kurt was also the first to read a preliminary version of this thesis and provided very helpful feedback.

Further thanks go to the Thorium community for its co-operative scientific work in contrast to the 'every man for himself'-approach. I especially want to thank Alex Kuzmich, Jake Lampen and Corey Campbell for welcoming me so warmly at the University of Michigan and letting me participate in their out-standing work

---

on thorium ion trapping. It was a wonderful time in Ann Arbor and I am truly grateful for all the lovely people I met there.

I benefited in more than one way from the time spent in Michigan, especially thanks to Linda and Rolf, who did not only welcome me into their home but also into their family. It soon became clear that this was not an ordinary host family, providing just a room for me. We shared wonderful dinners (especially the one at Thanksgiving) and an unexpected (for me) interest in American football (at least with Rolf), but most importantly, we shared stories and ideas.

Leo, my loyal compadre since early childhood, always reminded me to keep it down-to-earth. He has tolerated my quirks even in close-confinement situations and, in addition to being someone that you can easily get along with, he is very thoughtful when it comes to leaving others their freedom. His refreshing unconventionality is a source of great fun and can often drive away all kinds of piled-up negative feelings. I could not have asked for a better friend.

I can not thank my family enough for all the amazing support over the years. Nothing of this would have been possible without them. My parents, my sister Judith and her boyfriend (and brother-from-another-mother) Jochen were always there for me, sometimes to provide guidance, often to show interest but always to show that they care.

Tremendous support came from my girlfriend Evelyn, who reminded me of the importance of randomness, i.e. the lack of predictability, and that life, too, is all about interactions. May our journey together continue to be an adventurous one, full of joy and pleasant surprises.



# 1 Introduction

## 1.1 The isomeric transition of $^{229}\text{Th}$

$^{229}\text{Th}$  offers a very unique feature, namely a nuclear transition in an untypically low energy range. The isotope possesses the only known isomer with an excitation energy of a few eV, an energy range that is usually found in transitions between outer electronic shells of atoms. This makes  $^{229}\text{Th}$  a candidate for bridging the gap between different fields of physics. One of the many applications is nuclear spectroscopy with a laser, which transfers Mössbauer spectroscopy into the optical range.

The nuclear level structure of  $^{229}\text{Th}$  has already been studied in the 1970s by the group of C. Reich by performing gamma spectroscopy after the alpha decay of  $^{233}\text{U}$  [1]. A nuclear level structure, containing two low-energy levels with a spacing  $< 0.1$  keV, was deduced. One of the nuclear levels was the ground state, to which the quantum numbers  $3/2^+[633]$  according to the level classification of the Nilsson model were attributed. The other level was the isomer, described by the quantum numbers  $5/2^+[631]$ . By comparison of several decay cascades, the energy of the isomeric transition, i.e. between isomer and ground state, was determined to be  $3.5 \pm 1.0$  eV [2].

In an isolated nucleus, the lifetime of the isomer was estimated to be a few 1000 s, corresponding to a natural linewidth of a few millihertz. The decay of the isomer to the ground state is a magnetic dipole transition accompanied by the emission of a gamma photon in the optical range (again, for the case of an isolated nucleus). The chemical environment of the nucleus can affect the transition energy, lifetime (linewidth) and the decay mode of the isomer. Many attempts of directly detecting the isomeric state in the energy range given by Helmer and Reich failed or turned out to be false detections. A review of experimental and theoretical investigations of  $^{229}\text{Th}$  can be found in [3].

In 2007, the predicted isomer energy was shifted to the vacuum-ultraviolet (VUV) by high-resolution gamma spectroscopy carried out at the Lawrence Livermore National Lab [4]. The re-evaluated energy of  $7.8 \pm 0.5$  eV [5] is the currently most accepted value for the isomeric transition energy. Radiation at this wavelength is not transmitted through air, water or optical glasses, possibly explaining why previous attempts to detect the photonic deexcitation of the isomer failed. The new energy value lies between the first and second ionization potential of the neutral thorium atom. Internal conversion, in which the energy of the excited

nucleus is transferred to an electron and the latter is ejected from the atom, has therefore also become possible as an isomeric decay mode in the electrically neutral  $^{229}\text{Th}$  atom.

An experiment with a magnetic microcalorimeter that could reduce the large energy-uncertainty to the level of 0.1 eV is currently in preparation [6].

Only recently, the first direct observation of the isomeric transition was reported at the LMU Munich [7]. The isomer was populated by alpha decay of  $^{233}\text{U}$ , the  $^{229}\text{Th}$  ions were separated from other ions by a quadrupole mass separator and guided onto a multi-channel plate, where the conversion electrons generated by the isomeric deexcitation were detected. A number of cross-checks were carried out in order to exclude other possible origins of the observed signal, which showed different charge states of  $^{229}\text{Th}$  but vanished when the  $^{233}\text{U}$  source was replaced by a  $^{234}\text{U}$  source (producing  $^{230}\text{Th}$ ). The isomeric energy was constrained to 6.3 – 18.3 eV (first and third ionization potential of  $^{229}\text{Th}$ ), and the half-life for  $^{229}\text{Th}^{2+}$  is determined to be longer than 60 seconds (limited by the ion storage time in this experiment).

## 1.2 Possible application: a nuclear clock with $^{229}\text{Th}$

Atomic clocks cover a wide range from fundamental scientific experiments to technological applications of our everyday life. They are used as time and frequency standards in satellite-based navigation systems, telecommunication networks and broadcasting stations as well as in fundamental investigations of our universe, ranging from microscopic to macroscopic constituent parts, e.g. quantum physics, radioastronomy. Reviews on optical atomic clocks can be found in [8, 9].

The clock performance is characterized and limited by the following quantities. The *Q-factor* compares the resonator's bandwidth (linewidth of the transition  $\Delta\nu$ ) to its center frequency (transition frequency  $\nu_0$ ):

$$Q = \frac{\nu_0}{\Delta\nu}. \quad (1.1)$$

We consider a frequency standards for which the total time for preparation and interrogation of the atoms is given by  $T_c$ . If the atoms are interrogated only for a fraction  $\tau/T_c$  of the total cycle time  $T_c$ , the *frequency stability* is given by [10]:

$$\sigma_y(\tau) \propto \frac{1}{Q} \frac{1}{S/N} \sqrt{\frac{T_c}{\tau}} \quad (1.2)$$

where  $S/N$  is the signal-to-noise ratio. If the measurements are limited by shot-



noise, the frequency stability becomes

$$\sigma_y(\tau) \propto \frac{\Delta\nu}{\nu_0} \sqrt{\frac{T_c}{N\tau}} \quad (1.3)$$

with  $N$  as the number of oscillators (atoms/nuclei).

Frequency standards based on atomic transitions have made time the most precisely measurable physical quantity by far, with no fundamental limitation to the achievable accuracy in sight. Using a nuclear transition as a time/frequency reference, i.e. by resonantly exciting a radiative nuclear (i.e. gamma) transition with a coherent oscillator, provides some advantages over the use of atomic transitions. The relevant nuclear properties, namely decay rates and transition frequencies, are hardly influenced by the environment of the nucleus, including the physical or chemical state of the matter. Three practical motivations fuel the research towards building a **nuclear clock** (possibly based on  $^{229}\text{Th}$ ) [3]:

1. Higher accuracy through smaller systematic frequency shifts

Interactions with external electric or magnetic fields lead to systematic frequency shifts, limiting the accuracy of optical clocks. Temperature control and correction is required in order to minimize light shifts induced by thermal radiation from the environment. The smallness of the nucleus and the nuclear moments make nuclear transitions less sensitive against external perturbations compared to transition of the electron shell. A more detailed analysis of (temperature-dependent) broadenings and shifts of the isomeric transition in a crystal environment can be found in 1.3.3.

2. Higher stability in a solid-state optical clock

Interactions with the environment as well as between the atoms limit the number of oscillators in state-of-the-art optical clocks. Low atom numbers ranging from one (single trapped ion) to a few thousand (in optical lattice clocks) are used in a precisely controlled environment (ultrahigh vacuum, compensation of external fields, temperature stabilization etc.). In solid-state nuclear clocks (section 1.3.3) narrow and unperturbed resonances from a large ensemble of nuclei may be exploited. A huge gain in signal-to-noise ratio and stability can therefore be obtained by increasing the number of oscillators  $N$  in eq. 1.3 to ranges of  $10^{14} - 10^{19}$  in a crystal.

3. Higher stability through higher reference frequency

Increasing the frequency of the clock transition  $\nu_0$  leads to a higher Q-factor of the resonator (eq. 1.1) and therefore to a higher stability of the clock.

In Mössbauer spectroscopy, nuclear transition energies in the 10-keV-range are used, which are 4 orders of magnitude higher than in optical clocks. Replacing the

spontaneously emitted gamma radiation, used as a source in these experiments, by a coherent oscillator with the qualities of a tunable laser possibly allows ways of manipulating nuclear states that had previously been possible only for atomic states.

Variations of fundamental coupling constants are predicted by theories of grand unification [11]. Nuclear level structures depend mainly on the strong and weak force, whereas the main contribution for atomic levels is Coulomb interaction. The isomeric transition in  $^{229}\text{Th}$  is therefore more sensitive to variations of these forces than atomic transitions, and tighter constraints can be put on fundamental coupling constants [12, 13]. Other applications of the  $^{229}\text{Th}$  include gamma lasers [14], nuclear quantum optics [15, 16], a robust Q-bit [17] and testing the effect of the chemical environment on nuclear decay rates [18].

### 1.3 Experimental search for the isomeric transition of $^{229}\text{Th}$

This section gives an overview of experimental techniques currently applied in the search for the isomeric transition of  $^{229}\text{Th}$ , with an emphasis on the approach chosen at the Vienna University of Technology (section 1.3.3). A more detailed description can be found in the review [3] or on the webpage of the NuClock consortium [19].

#### 1.3.1 Ion traps

Trapped thorium ions excited by laser photons probably provide the system for the most precise determination of the isomeric transition frequency. Due to the lack of UV laser which are tunable over the wide range corresponding to the currently accepted isomer energy ( $7.8 \pm 0.5$  eV or 149 – 170 nm), direct laser excitation of the nuclear transition seems beyond current technical feasibility. Energetic coupling of the nucleus and the electronic shell provides a way of populating the isomer by energy transfer from an atomic to a nuclear state [20]. This can be achieved via two-photon electronic bridge processes, for which an electronic level that is energetically close to the isomer energy has to be populated. Another way is NEET (nuclear excitation by electron transition), where the energy difference between an energetically higher-lying atomic state and the isomer is compensated by spontaneous photon emission.

Two different charge states of thorium are the focus of currently running experiments:  $^{229}\text{Th}^+$  is investigated at the PTB Braunschweig. This ion has a high density of electronic states due to its three valence electrons outside the Rn-like core, making two-photon electronic bridge processes a good candidate for isomeric excitation.

Experiments in which up to  $10^6$   $^{232}\text{Th}^+$  were loaded into a linear Paul trap and cooled to room temperature by an argon buffer gas, revealed 43 previously unknown electronic levels [21, 22]. Scanning the excitation laser over the search range from 7.3 to 8.3 eV is currently in progress with the  $^{229}\text{Th}$  isotope.

The most promising candidate for the development of nuclear clocks with trapped ions is  $^{229}\text{Th}^{3+}$ , which possesses a single valence electron. This ion has an electronic level structure suitable for laser cooling, offering high spectral resolution and efficient state detection. In contrast to the triply-charged ion, there are only very few electronic states available for electronic bridge processes.

Experiments with  $^{229}\text{Th}^{3+}$  were initially built at Georgia-Tech in Atlanta and then moved to the University of Michigan in Ann Arbor. After preliminary experiments with  $^{232}\text{Th}^{3+}$  [23], Wigner crystals of  $^{229}\text{Th}^{3+}$  were produced in a linear Paul trap [24]. Isotopic shifts of three transitions as well as the hyperfine splitting factors of four levels were determined and a value for the nuclear electric quadrupole moment was deduced [25].

### 1.3.2 Recoil nuclei

The  $^{229}\text{Th}$  isomer is populated in 2% of the alpha decays of  $^{233}\text{U}$ . This allows experiments for the search of the isomeric transition that do not require an excitation source (laser, synchrotron etc.) or precise knowledge of the isomer energy or lifetime.  $^{229}\text{Th}$  recoil ions are collected on an absorber plate, thus allowing the separation of the photon detection from the population of the isomer, which is accompanied by radioactivity and the associated radioluminescence (further details in section 3.2.1).

Experiments of this kind were carried out at the PTB [26] and at the Lawrence Livermore National Lab [27]. The reported discovery of optical deexcitation of the  $^{229}\text{Th}$  made at the Los Alamos National Lab [28] raised the question whether the decaying signal should rather be attributed to radioluminescence of the absorber plate and other nuclear decays [29] (also compare section 3.2.3).

The recently published direct observation of the isomeric transition via electron conversion at the LMU Munich (already described in section 1.1) is also based on the collection of  $^{229}\text{Th}$  recoil nuclei [7].

### 1.3.3 The solid-state approach: $^{229}\text{Th}$ implanted in a crystal

Large ensembles of  $^{229}\text{Th}$  nuclei ( $10^{14}$ – $10^{20}$ ) can be implanted into UV-transparent crystals [30]. Broadening of the isomeric transition due to interaction of the nucleus with the crystal environment may even facilitate the search for the isomeric

transition but at the same time reduce the Q-factor. The large number of oscillators (compared to ion traps) provides an increased stability for the application of a nuclear clock (section 1.2).

Thorium atoms in a crystal lattice are confined to the Lamb–Dicke regime, i.e. the recoil energy  $E_{rec} = E(7.8 \text{ eV})^2 / (2M_{Th}c^2) = 1.4 \cdot 10^{-10} \text{ eV}$  is much smaller than the energy required for the creation of a phonon with the recoil momentum  $p_{rec} = E(7.8 \text{ eV})/c$  [31]. The recoil can only be transferred to the crystal lattice by optical phonon scattering. However, optical modes are expected to be frozen out, even at room temperature [30]. This leads to a decoupling of internal and external degrees of freedom and the transition energy is therefore not sensitive to recoil or first-order Doppler effects.

Shifts and broadenings of the isomeric transition strongly depend on the chemical surroundings of the implanted nuclei, i.e. electric and magnetic fields of neighbouring ions. Nuclear spectroscopy thus provides insight into the interactions between the nucleus and the crystal lattice and allow testing how the chemical environment affects nuclear decay rates. Estimations on shifts and broadenings of the isomeric transition in a  $\text{CaF}_2$  crystal, which is the focus of our investigations at the Vienna University of Technology, are given in section 1.3.3. The charge difference between the  $\text{Th}^{4+}$  ion and the  $\text{Ca}^{2+}$  it substitutes has to be balanced by additional atoms or vacancies in the crystal lattice (section 3.1.1). The thereby introduced inhomogeneities in the periodic lattice can affect both, the properties of the crystal (e.g. UV transmission) and/or the nucleus (e.g. shifts and broadenings).

Possible excitation sources in the search for the isomeric transition are synchrotrons, which provide sufficient intensity and a wide tunability in the expected energy range for a coarse determination of the isomer energy. The isomeric state can thereby be excited without requiring knowledge of the exact wavelength.

Broadband excitation with undulator radiation from an electron storage ring at the Metrology Light Source (MLS) of the PTB [32] is currently in preparation for the  $^{229}\text{Th}:\text{CaF}_2$  crystals grown for this thesis. For realistic experimental parameters, a detectable steady-state fluorescence signal of 1000 photons per second is expected from a transparent crystal containing  $10^{13}$  nuclei [3].

Other attempts of using doped crystals for the nuclear spectroscopy of  $^{229}\text{Th}$  have been made in a corporation of the University of California, Los Angeles, and the Los Alamos National Laboratory. Charge compensation configurations for thorium doped into  $\text{LiCaAlF}_6$  (LiCAF) and  $\text{LiSrAlF}_6$  (LiSAF) have been calculated in [33]. Effects on the isomeric transition by the crystal environment (shifts and broadenings), that determine the performance of a solid-state nuclear frequency standard or the sensitivity of fundamental constant variation, were investigated in [30]. Further considerations for the  $^{229}\text{Th}$  solid-state approach were made

in [34]. Several high energy band-gap crystals were tested for their suitability as a host crystal for  $^{229}\text{Th}$  [35]. A synchrotron search for direct excitation of the isomeric transition in  $^{229}\text{Th}$ -doped LiSAF was carried out at the Advanced Light Source in Berkeley [36]. It found no evidence for excitation or photonic deexcitation of the isomeric state in the energy range of 7.3 – 8.8 eV with transition lifetimes  $(1-2) \text{ s} < \tau < (2000-5600) \text{ s}$ .

$^{229}\text{Th}$  atoms adsorbed on the surface of  $\text{CaF}_2$ , were investigated at the PTB, Braunschweig [37]. This experimental approach circumvented the difficulties arising from the growth of crystals doped with the radioactive  $^{229}\text{Th}$ , but could not detect photons originating from the isomeric transition. Due to the adsorption process, the chemical form and/or environment of the  $^{229}\text{Th}$  atoms is unknown. Electron bridge mechanism may make the nuclear lifetime much shorter (1) or longer (2) so that the opening time of the mechanical shutters (1) or the fluorescence background noise masking the isomeric photons (2) prevent the detection of the isomeric photons. Non-radiative decay due to internal conversion may also shorten the isomer lifetime or prevent photon detection.

Coherent forward scattering was suggested as an efficient method for detection of the isomeric transition in a crystal [16]. The luminescence background could be reduced because the signal would be carried in a directional beam, allowing the detector position to be further away.

### Broadenings and shifts of the isomeric transition in $\text{CaF}_2$

Thorium ions are expected to be embedded into the crystal lattice as  $\text{Th}^{4+}$  ions due to their high electropositivity of 1.3 Pauling, leading to a radon-like noble gas electron configuration in the ion. Only the  $\text{Ca}^{2+}$  site qualifies as a doping site. The similar ionic radii of  $\text{Ca}^{2+}$  and  $\text{Th}^{4+}$  (1.26 Å and 1.19 Å [38]) facilitate the replacement in the doping process. Possible configurations for charge compensation were calculated using numerical models (section 3.1.1). A detailed analysis of broadenings and shifts of the isomeric transition can be found in [30, 31], a summary of the results therein is given in the following.

In the ionically bonded crystal lattice, all electron spins are paired, yielding a vanishing fine-structure interaction. The hyperfine interaction remains as the dominant source of shifts and broadenings of the isomeric transition. Using a multipole expansion, three major contributing terms can be distinguished that will be discussed in the following:

$$H_{HFS} = H_{E0} + H_{M1} + H_{E2} + \dots \quad (1.4)$$

The **electric monopole term**  $H_{E0}$  describes the contact interaction between the electron cloud and the finite volume of the nucleus. Changes in the size of

either one lead to changes in the isomeric transition energy. Since the physical dimensions of the nucleus are different in the ground state and the isomer, this effect leads to a shift of the nuclear transition relative to a bare nucleus. Electric monopole shifts depend on the host crystal but are typically on the order of 100 MHz [30] to a few GHz [13,39]. As long as the crystal environment is identical for the different nuclei in the crystal, i.e. the neighbouring ions arranged in the same configuration<sup>1</sup>, this will lead to constant, identical shifts of the isomeric energy and therefore only affect the nuclear clock accuracy, but not the stability (precision).

However, the electron density at a specific lattice is temperature-dependent, leading to an inhomogeneous broadening of the isomeric transition if temperature gradients occur over the crystal extensions. This temperature dependence is estimated to be 10 kHz/K [30], leading to a broadening of about 10 Hz for a temperature stability of  $\Delta T = 1$  mK.

The **magnetic dipole term**  $H_{M1}$  causes a shift and splitting of both nuclear states in the presence of a magnetic field at the nucleus. Crystals with large band gaps are free of spurious electric currents and all electron spins are paired so that the anti-parallel magnetic moments cancel each other out. The only remaining magnetic fields in the crystal are caused by the magnetic moments of neighbouring nuclei. The magnetic dipole interaction is the dominant source of inhomogeneous broadening, calculated for  $\text{CaF}_2$  crystals to be  $2\pi \cdot (84\text{--}251)$  Hz, depending on the sub-levels of the quadrupole structure (see next section) between which the isomeric transition occurs. In LiCAF crystals, it was estimated to be (1 – 10) kHz [30].

The **electric quadrupole term**  $H_{E2}$  described the interaction of the electric quadrupole moment of the  $^{229}\text{Th}$  nucleus with an electric field gradient at the position of the nucleus, which depends on the structure of the host crystal. Since both states of the isomeric transition have a nuclear spin  $I > 1/2$ , they can both support a quadrupole moment (only known for the ground state). The resulting quadrupole splittings of both nuclear states are on the order of a few hundreds of MHz, which can be resolved in laser spectroscopy [31]. If the chemical environment of the different nuclei is identical, the level splittings only shift the nuclear transition frequency but do not affect its linewidth, which determines the stability of the nuclear clock. Electric field gradients and quadrupole shifts of ground state and isomer levels, corresponding to different charge compensation configurations, were calculated in [39]. The quadrupole shift is minimized for host crystals with cubic or icosahedral symmetry [30].

However, a temperature-dependence causing inhomogeneous broadening arises because the nuclei can vibrate in their lattice sites. The interactions between the nuclei and phononic modes of the crystal lattice leads to mixing between

---

<sup>1</sup>compare the difference configurations for charge compensation discussed in section 3.1.1

different quadrupole sublevels as their typical level spacings are much smaller than characteristic phonon energies. By comparison with other crystals a relaxation and mixing rate was determined to be on the order of  $2\pi \cdot (5\text{--}100)$  Hz at room temperature and  $2\pi \cdot (0.3\text{--}7)$  Hz at liquid nitrogen temperature, scaling with  $T^2$  [31].

Vibrations of a nucleus also lead to a shift of the isomer transition energy due to the **second-order Doppler effect**. Using a classical harmonic oscillator model, the shift of the isomeric transition is

$$\omega' = -\omega \frac{v^2}{(2c^2)} = -\omega \frac{3k_B T}{2M_{\text{Th}} c^2} \quad (1.5)$$

where  $\omega$  is the isomeric transition frequency and  $v$  the velocity of the thorium nucleus.

The shift for each nucleus depends on the temperature  $T$  and a temperature difference over the crystal therefore causes inhomogeneous broadening of the isomeric transition by

$$\Delta\omega = \omega \frac{\langle \Delta v^2 \rangle}{2c^2} = \frac{\sqrt{6} k_B T}{2M_{\text{Th}} c^2}. \quad (1.6)$$

The second-order Doppler effect leads to a shift of about  $2\pi \cdot 1.14 \cdot T$  (in Hz) and to a broadening of about  $2\pi \cdot 0.93 \cdot T$  (in Hz) where  $T$  is the temperature in Kelvin [31].





## 2 Growth of (doped) calcium fluoride crystals

Synthetic calcium fluoride crystals for optical applications were developed in the 1930s to exploit the material's unique optical, physical and mechanical characteristics. They comprise a broad transmission window from the far ultraviolet up to the mid-infrared, within which the refractive index varies less than that of other fluoride crystals, superior dispersion characteristics, low stress-induced birefringence, negligible solubility in water and insolubility in many acids, an adequate hardness, a fair thermal conductivity and a high resistance to radiation at a low luminescence level. These properties made  $\text{CaF}_2$  the material of choice for various optical elements. Calcium fluoride was used for windows, lenses, mirrors and prisms; in laser optics, holography, dosimetry, lithography etc. [40].

In the late 1980s, military needs for optical elements used in night vision devices, systems for automatic rocket control and other related applications lead to an production improvement of  $\text{CaF}_2$  as an optical material, mainly in IR-optics. The early 1990s were marked by a considerable rise in interest in VUV-grade  $\text{CaF}_2$ . Large lenses found applications in commercial television cameras requiring chromatically corrected lenses. The required substantial volumes lead to another increase in production yield. Furthermore,  $\text{CaF}_2$  was used for windows in excimer lasers, developed to generate shorter wavelengths in the UV range.

Calcium fluoride is still widely used for large-diameter lenses in photolithography. One important challenge of the semiconductor industry has been, and still is, the decrease of structural elements in integrated circuits (e.g. computer chips, data storage devices), which are produced by illuminating the photoresist through photomasks to pattern the microstructures: the shorter the wavelength, the smaller the structures that can be created. The material used for the lenses in photolithography should therefore be transparent in the deep UV and be able to withstand high radiation intensities. Single crystals of  $\text{CaF}_2$  fulfill these requirements and therefore a lot of effort was put into the improvement of the crystal growth in order to obtain large-volume single crystals with a high transmission and a good homogeneity of the refractive index.

### 2.1 Crystal growth from the melt: a general introduction

In this section, general principles and techniques for crystal growth from the melt are introduced. All of them are valid for growing calcium fluoride crystals, but can be applied to a much larger variety of materials beyond that. Other techniques

that include growth from the gaseous phase, growth from solutions and growth in solids are not (widely) used for calcium fluoride and are therefore only mentioned for the sake of completeness. Detailed descriptions and lists of crystals that have been produced by the various growth techniques can be found in [41].

Today, most crystals are grown from the melt. This includes semiconductors like silicon, laser crystals, and dielectric crystals for optical, electro-optical and piezo-electrical applications. The crucial parameter is temperature, whereas heat transfer is the key phenomenon. The heat flow through the phase boundary between the liquid melt and the solid crystal can be described by:

$$q_l = q_s + \Delta h j \quad (2.1)$$

where  $q_l$  and  $q_s$  are the heat fluxes in  $[\text{W}/\text{m}^2]$  of the liquid phase  $l$  and the solid phase  $s$ ,  $\Delta h$  is the (latent) heat of fusion<sup>1</sup> and  $j$  the density of the mass flow in  $[\text{m}^{-2} \text{ s}^{-1}]$  which undergoes the phase transition. The growth velocity, i.e. the velocity at which the phase boundary is shifted, is then given by<sup>2</sup>

$$v = -\frac{j}{c_s} = \frac{(q_s - q_l)}{\Delta h c_s} \quad (2.2)$$

where  $c_s$  is the particle density in  $[\text{m}^{-3}]$  in the crystal. Temperature is increasing towards the melt, and heat is dissipated through the crystal. The heat fluxes can be expressed by<sup>3</sup>

$$q_{l,s} = -\lambda_{l,s} \left( \frac{\partial T}{\partial z} \right)_{l,s} \quad (2.3)$$

with  $\lambda_l$  and  $\lambda_s$  being the thermal conductivities and  $\left( \frac{\partial T}{\partial z} \right)_{l,s}$  the temperature gradients of the liquid phase ( $l$ ) and the solid phase ( $s$ ). Inserting into eq. 2.2 yields

$$v = \frac{\lambda_s (\partial T / \partial z)_s - \lambda_l (\partial T / \partial z)_l}{\Delta h c_s}. \quad (2.4)$$

The growth velocity is therefore highest for large temperature gradients in the crystal and small temperature gradients in the melt (e.g. minimized by convec-

---

<sup>1</sup>a.k.a: enthalpy of fusion: energy required for melting a substance. The same amount of energy is released when this substance crystallizes.

<sup>2</sup>Sign convention: the positive  $z$  direction, along which the crystal growth occurs, points into the melt and therefore into the opposite direction of the mass flow (which is negative).

<sup>3</sup>neglecting the movement of the phase boundary

tion). The maximum growth velocity is obtained for constant temperatures in the melt:

$$v_{max} = \frac{\lambda_s}{\Delta h c_s} \left( \frac{\partial T}{\partial z} \right)_s. \quad (2.5)$$

In this case, only the latent heat of fusion has to be dissipated. From eq. 2.5, it can be seen that materials with high thermal conductivities  $\lambda_s$ , e.g. metals<sup>4</sup>, can be grown faster than those which provide poor heat transfer.

Three different technical principles can be distinguished for crystal growth from the melt (two of which will be described in the following sections 2.1.1 and 2.1.2):

- Crystal growth in crucibles
- Crystal pulling from the melt: the melt is kept in a crucible as well, but the crystal grows freely suspended on the seed, i.e. without contact to the crucible walls
- Methods without crucibles: not treated here, e.g. zone-melting (silicon)

### 2.1.1 Crystal growth in crucibles

The raw material is heated above the melting point in a crucible (container that can withstand the required physical and chemical conditions). Subsequently, the temperatures in the crucible are lowered in a controlled way, so that the melt crystallizes. Growth inside a crucible causes the shape of the crystal to be formed by the container walls.

The crucible material must be resistant to the high temperatures but at the same time allow a sufficient energy transfer to the raw material (e.g. thermal conduction, induction heating). Thermal contraction of the crucible should only put minimal mechanical tension on the crystal during growth and cool-down. Furthermore, the crystal should not stick to the crucible walls during or after growing, and the crucible material should not chemically react with the crystal (raw material) during the growing process.

These problems can be tackled by choosing a material with a similar thermal expansion coefficient as the crystal, or a soft and ductile one. The crystal can also be removed from the crucible after solidifying and be cooled down outside of it. Providing smooth and clean container walls, eventually with some protective

---

<sup>4</sup>For example, the thermal conductivities of Sn and Zn are 65 W/(m·K) and 110 W/(m·K), compared to 9.71 W/(m·K) of CaF<sub>2</sub>.

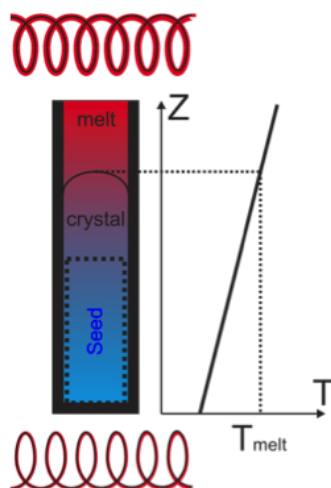


Figure 2.1: Vertical gradient freeze method

coating, is essential. This ensures an easy removal of the crystal after the growing process but also avoids introducing impurities or defects.

In the growth of  $\text{CaF}_2$  crystals, crucibles made of graphite or molybdenum are used. Platinum crucibles are not recommended since corrosive fluorine gases damage this material.

In the following, the two different methods for growing crystals in crucibles are explained. Further details can be found in [41], whereas [42] gives an overview of the historic contributions in the development of crystal growth.

### Vertical gradient freeze method (Tammann-Stöber method)

A vertical temperature gradient is applied to a stationary, upright crucible. The lowest temperature is at the bottom, and therefore, crystallization starts there (fig. 2.1). The temperature gradient and the crucible are shifted with respect to each other so that the crystal grows upwards [43, 44]. This was first achieved by heating the crucible from the side or the top, and cooling the bottom with air or water in order to initialize crystallization [45]. Later, heating coils were arranged underneath and above the crucible, and the solid/liquid interface was shifted upwards by regulating the power in one or both heaters [46]. For large crystals, or for a better control of the temperature field in the crucible, the number of heating coils can be increased.

Microscopic crystals are formed in the melt when the temperature is low enough (nucleation). The growth of mono-crystals though, requires a seed crystal that provides only one orientation for the further crystallization process. Therefore, crucibles are used, in which the inner diameter is reduced towards the bottom so that only one seed/crystal orientation can be sustained (seed selection) at the

lower end<sup>5</sup>, i.e. the point with the lowest temperature. A way of determining the crystal orientation before growing, is to use a mono-crystalline seed that is only partially melted at the highest temperature. The melt crystallizes on top of the seed, maintaining its orientation. This is the most challenging part of the growth process (also in our case), since the position of the phase boundary has to be controlled over a range determined by the size of the seed.

Furnaces without moving parts are easier to maintain than those described in the next section (2.1.1), but a process control mechanism is required in order to control the temperature. For some crystals, in particular some metals, it is sufficient to simply switch off the heating in order to obtain the rather high cooling rates.

### **Bridgman-Stockbarger method**

In order to move the phase boundary upwards, the crucible and the heating coils can be mechanically moved with respect to each other [47, 48]. In the simplest form, a heating coil is operated at constant power and the crucible is lowered into the coil and exits on the other side. More advanced furnaces have two independent temperature zones through which the crucible is passed. Typically, the temperature in the upper zone is above the melting point and below it in the lower zone. A heat shield between the two zones ensures a steep temperature gradient. Alternatively, the heating coil that surrounds the crucible can be moved upwards, or heat shields can be introduced between heating coil and crucible.

#### **2.1.2 Crystal pulling from the melt**

The raw material is molten in a crucible, and the temperature of the melt is kept above the melting point. A seed crystal is introduced from above into the melt. The seed conducts some heat away from the melt so that crystallization starts at the surface of the seed.

The requirements for the crucible are similar to the above-mentioned ones, whereas the difference between the growth techniques in this section and section 2.1.1 is, that the crystal is growing freely suspending on the seed, i.e. without contact to the crucible walls.

The two growth methods described in the following are very similar and therefore not always clearly distinguished. This is also the reason why the Nacken-Kyropoulos method is mentioned here, although, in most cases, it does not involve any actual pulling of crystals like in the Czochralski method.

---

<sup>5</sup>The lower end can be a sharp tip but in many cases it is sufficient to just reduce the diameter a bit. Capillary tubes are also used for seed selection.

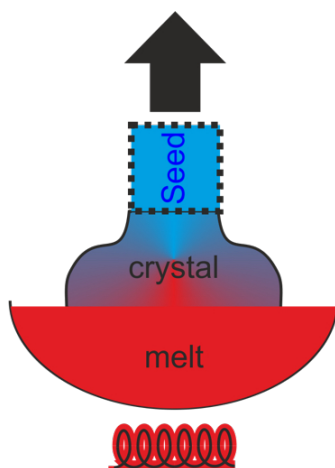


Figure 2.2: Czochralski method

### Nacken-Kyropoulos method

A seed crystal is dipped into the melt<sup>6</sup> and actively cooled so that crystallization occurs [49, 50]. The crystal grows further into the melt as long as enough heat is conducted away through the crystal from the solid/liquid phase boundary.

### Czochralski method (Cz)

A seed crystal is dipped into the melt, whose temperature is kept slightly above the melting point. The melt crystallizes onto the seed, which is slowly pulled upwards (fig. 2.2). The crystal does not grow further into the melt like for the Nacken-Kyropoulos method, but the solid/liquid phase boundary is always kept close to the melt's surface instead [51]. The crystal diameter depends on the pulling speed, whose limits depend on the substance (0.1 - 100 mm/h [41]). The crystal can be rotated around its cylindrical axis (parallel to the direction of pulling), at typical frequencies between  $1 \text{ min}^{-1}$  and  $100 \text{ min}^{-1}$ , again depending on the material [41].

Seeding, i.e. the process of crystallizing onto the seed so that the grown crystal has the same properties as the seed, is the most crucial but also most challenging part of the growth process. The seed is brought close to the melt for temperature exchange before dipping it in. Due to the temperature difference between seed and melt, a poly-crystal is often formed first. One needs to wait until it is molten again, as well as a part of the seed, before starting to pull. If the temperature of the melt is too low, a poly-crystal or a disturbed crystal growth are the results.

---

<sup>6</sup>If no seed crystal is available, a material with a higher melting point, on which nucleation occurs, can be used in order to create poly-crystals. A mono-crystalline part is selected and subsequently used as a seed.

If the temperature of the melt is too high, the connection between the seed and the melt is severed.

It might be advantageous to choose a high pulling speed such that the crystal diameter is very small (1 mm) in the beginning of the growth. Defects resulting from the seed or from imperfect seeding (like dislocations or subgrain boundaries) can “grow out” of the crystal in the narrow part. Afterwards, the pulling speed is reduced until the desired crystal diameter is reached. By means of this procedure, the first dislocation-free silicon crystals were grown [52].

In order to keep the crystal diameter constant, the liquid/solid interface has to be maintained in the same position, which requires feedback control. If the pulling speed or the heating power is too high (low), the phase boundary is too far up (down) and the crystal gets thinner (thicker). However, the released heat of crystallization, i.e. the latent heat of fusion, has a stabilizing effect. The higher the growth speed, the more heat of crystallization is released, which inhibits the crystallization. The growth process is often controlled by varying the temperature (heating power) instead of the pulling speed<sup>7</sup>. Sometimes, the furnace is lowered together with the heater, while the crystal position remains constant.

### 2.1.3 Comparison of the growth methods

For many materials, the Czochralski method is the most developed growth technique and therefore the method of choice for obtaining the best crystal quality [41]. However, the technological challenges (e.g. design of the furnace, feedback mechanism for process control) are significant. Cz growth requires thorough observation and control, and is more failure-prone than growth in crucibles. On the other hand, Cz imposes optical access to the crystal during growth and thereby offers better control for maintaining steady/constant growing conditions,

For our purposes, the vertical gradient freeze method (VGF) provides a few important advantages. The furnace is easier to handle and the growth process is more robust. The growth velocity can be chosen arbitrarily slow ( $< 0.5$  mm/h [41]) without affecting the crystal diameter, and the crystal volume can therefore be very small, even for slowly grown crystals.

When doping  $\text{CaF}_2$  crystals with the rare and pricey  $^{229}\text{Th}$ , the dopant has to be added rather homogeneously and effectively, i.e. without wasting too much of it. For a given amount of  $^{229}\text{Th}$ , the crystal volume has to be kept small in order to optimize the doping concentration ( $> 10^{14}$   $\text{cm}^{-3}$ ). In the Cz method, the pulling speed determines the crystal diameter/volume. Small-sized crystals can only be grown at rather high growth velocities, which reduces the crystal quality. Furthermore, distorting a regular crystal lattice, by substituting a different atom

---

<sup>7</sup>Moreover, the effective pulling speed increases during growth because the melt is used up and therefore the level of the liquid is lowered.

into it, costs energy. The dopant is not necessarily incorporated in the crystal lattice but could accumulate in the melt instead. In the Cz method, not all of the melt can be used for crystal growth<sup>8</sup>. The Cz-grown <sup>232</sup>Th-doped CaF<sub>2</sub> crystal showed a doping efficiency of  $\sim 30\%$ , meaning that 2/3 of the dopant remained in the melt from which the crystal was grown. This behavior is also reflected in the doping concentrations of the different crystal parts. More <sup>232</sup>Th can be found in the part that crystallized later in the growth process, when the increasing <sup>232</sup>Th concentration in the melt forced more and more thorium atoms into the crystal.

VGF-grown crystals also show an increasing Th concentration towards the later-grown parts (section 3.5.2) but all of the melt becomes part of the crystal finally.

During Cz growth, the surface of the melt and the phase boundary are very close together. Particles floating on the melt, as well as gas bubbles, can be easily incorporated into the crystal when it grows downwards. In the VGF method, in which the crystal grows upwards, the phase boundary reaches the melt surface only at the end of the growth with negligible convection effects. The free surface area of the melt is smaller. A thermal field configuration, with a sufficiently steep temperature gradient for compensating a partial supercooling of the melt [53], can be provided in the furnace [40].

Heating from below, like for the Cz method, introduces convectional currents which improve the mixing of the raw materials in the melt but can also cause instabilities.

Thermal stress is the result of temperature gradients in the crystal during cool-down. Axial gradients can be very small and nearly constant in VGF. The radial gradients can in principle be reduced to zero, resulting in a flat phase boundary and a high crystal quality. In Cz growth an axial temperature gradient is necessary for the regulation of the crystal diameter, whereas in VGF, the form of the crucible determines the crystal shape. Therefore, VGF is used for obtaining specially shaped crystals, thereby avoiding material loss and the change of physical/mechanical properties due to machining [54].

The success of industrial technology development for optical CaF<sub>2</sub> is based on the vertical Bridgman technique which is preferred over the vertical gradient freeze method. The latter requires a tighter temperature control using a thermocouple, as well as a more precise control of the growth rate [55]. Nevertheless, a shortcoming of the conventional Bridgman method is the impossibility of ensuring a sufficiently high vertical temperature gradient in the crystallization zone [40]. This leads to melt supercooling in a thin layer just ahead of the crystallization front, resulting in the segregation of impurities therein. A fluctuation of the defect density is the consequence [53].

---

<sup>8</sup>It crystallizes in the crucible and can be re-used for the next crystal, though.



## 2.2 The Furnace: design and principle of operation

In the Fraunhofer Institut IISB<sup>9</sup> in Erlangen, we found a cooperation partner with experience in CaF<sub>2</sub> crystal growth. An R&D furnace for the growth of high-quality calcium fluoride crystals was already developed there [56]. Our requirements for a smaller crystal volume, however, called for a different design. Making use of the IISB's vast experience in crystal growth and the design of a small furnace, which was previously used for the investigation of Silicon<sup>10</sup>, a way for growing our own (doped) CaF<sub>2</sub> crystals was found. The furnace was numerically simulated and optimized by Dr. Kurt Semmelroth with the author's support, whereas the findings of Dr. Alexander Molchanov [56–58] were used for process development. The collaboration with the IISB involved several visits of the author in Erlangen for training and test purposes during the furnace development. The first eleven attempts for growing calcium fluoride crystals were still made at the IISB, before the furnace was transferred to Vienna for further development.

### 2.2.1 General requirements for the growth of small CaF<sub>2</sub> crystals

The furnace has to provide conditions under which a stable growth of (doped) single crystals with a low number of defects and a high uniformity is possible. In order to obtain a good optical quality, it is important to avoid not only defects like dislocations or grain boundaries, but also to minimize thermal stress during growth and avoid undesired impurities.

In contrast to the requirements in industry, where large crystals (diameter > 400 mm [59]) are produced, the low availability (and therefore the high price) of <sup>229</sup>Th limits the crystal volume for a given doping concentration. Growth in crucibles (section 2.1.1) allows the growth of centimeter-sized crystals at a low growth rate. In order to obtain small crystal volumes by the Czochralski method (section 2.1.2), the pulling speed, i.e. the growth velocity, has to be increased, thereby increasing the probability for defect formation. Furthermore, a first <sup>232</sup>Th-doped crystal grown by the Czochralski method showed a doping efficiency of ~ 30%, with 2/3 of the dopant remaining in the melt from which the crystal was grown (section 3.5.2). Better results can be obtained by growth in a crucible, since there is no remaining material that is not incorporated into the crystal. For our purposes, the expected higher doping efficiency and the low growth rates favor growth in crucibles over crystal pulling from the melt.

The handling of the radioactive thorium isotopes is easier at the Atominstitut compared to crystal growth facilities, that usually do not have the permission to work with substances above a certain radioactivity threshold. The Institut für

---

<sup>9</sup>Fraunhofer Institut für Integrierte Systeme und Bauelementetechnologie

<sup>10</sup>grown under similar conditions as calcium fluoride

Kristallzüchtung (IKZ) in Berlin was willing to grow a  $^{232}\text{Th}$ -doped  $\text{CaF}_2$  crystal for us, but a thorough decontamination of the furnace was required afterwards. Doping with  $^{229}\text{Th}$  turned out to be impossible at IKZ. Besides that, one man's dopant is another man's impurity, which often makes providers of commercially available  $\text{CaF}_2$  crystals reluctant to add dopants, especially if they are radioactive.

### 2.2.2 Requirements to the temperature field and the phase boundary

Stable growth requires a sufficiently large axial temperature gradient in the melt. In that case, the effects of small temperature fluctuations on the position of the phase boundary are minimized. An inhomogeneous temperature field creates thermal stress in the crystal, and a constant axial temperature gradient is required in order to minimize them [60]. Due to the temperature-dependent thermal conductivity, the semi-transparency of calcium fluoride (section 2.2.3) and geometrical effects, non-linearities occur in the temperature field [56, 57]. For these reasons, a small axial temperature gradient is favored (in contrast to before). In order to ensure a linear temperature field, the phase boundary should be flat. Often, a convex phase boundary is preferred so that defects grow towards the crystal surface instead of accumulating in the crystal, like for a concave interface. Some requirements to the temperature field and the phase boundary are contradictory, and compromises need to be found [56]:

- constant axial temperature gradient: 1 – 5 K/cm
- slightly convex phase boundary
- slow crystal growth rate (0,01 – 0,05 K/min).

The main difference to Molchanov's furnace [56] was the much smaller crystal volume required in Vienna in order to obtain a certain doping concentration with the rare  $^{229}\text{Th}$ . The compact design poses challenges of a different kind for obtaining the required axial temperature gradient (section 2.2.4) and the control of the position of the phase boundary (section 2.2.4).

### 2.2.3 Numerical simulation

The material and shape of the inner parts of the furnace, i.e. thermal insulation, crucible and its mounting, heaters etc., determine the temperature field in which the crystal is grown and therefore the crystal quality. However, the high melting temperature and the strong corrosiveness of  $\text{CaF}_2$  limit the choice of possible materials drastically.

The axial temperature gradient probably has the strongest influence on the crystal growth (also see 2.2.4). The shape of the phase boundary should be stable in

a certain range of temperatures and temperature gradients, but also rather independent of the position of the phase boundary. This way, similar conditions can be maintained throughout the growth process, ensuring a homogeneous crystal quality.

The transmission spectrum of high-quality calcium fluoride shows a plateau between  $0.2\ \mu\text{m}$  and  $7\ \mu\text{m}$ , where a maximum value of more than 90% is maintained [61]. The absorption edges slightly shift to the visible range for increasing temperature [62, 63] but the absorption properties in the plateau range do not change significantly [56]. Black-body radiation shows a maximum around  $2\ \mu\text{m}$  at the melting temperature of  $\text{CaF}_2$ , i.e. the main share of thermal radiation is emitted in the range where the material's absorption is minimal. Thermal radiation is therefore not negligible: at the melting temperature the ratio of thermal conductance to thermal radiation for a 10 cm long crystal varies between 0.26 and  $2,6 \cdot 10^{-3}$  for an absorption coefficient of 0.1 to  $0.001\ \text{cm}^{-1}$  [64]. However, the transparency of  $\text{CaF}_2$  strongly depends on its purity which can also differ between the crystal and the melt of the same material [56]. Measurements during the growth of high-quality  $\text{CaF}_2$  crystals have shown that the axial temperature gradient in the crucible is independent of the position of the phase boundary, i.e. for different fractions of solid and liquid phase. This means that the heat transport through the crystal and the melt is similar [56].

During crystallization the latent heat of fusion, i.e. energy necessary for melting a crystal, is released. At a crystal growth rate of 1 mm/h the heat flux in calcium fluoride makes up 30% of the external heat flux [56] and has to be considered in the numerical models.

A detailed description of process simulation of  $\text{CaF}_2$  growth and the development of an advanced model can be found in [56]. The results obtained therein show a good agreement with experimental data [57] and were considered while developing the simulation software CrysMAS<sup>©</sup>. It was used by Dr. Kurt Semmelroth for designing the furnace and should therefore be briefly described in the following.

CrysMAS<sup>©</sup> is a program developed at the Fraunhofer IISB in Erlangen for numerical simulations of crystal growth processes in complex furnaces with axial symmetry [65]. It is based on the program CrysVUN<sup>©</sup> which uses a finite volume discretization scheme using an unstructured grid.

It allows computing the heating powers required for reaching certain temperatures at defined control points in the furnace (inverse simulation<sup>11</sup>). First, the furnace geometry has to be defined. Then, the different materials are assigned to furnace regions from a database which includes properties like thermal conductivity and emissivity. Finally, conditions (e.g. heaters and control points, boundary conditions) are defined and parameters are set. One can distinguish between hard

<sup>11</sup>The forward simulation, in which the temperature distribution is computed for given powers in the heaters, is also possible

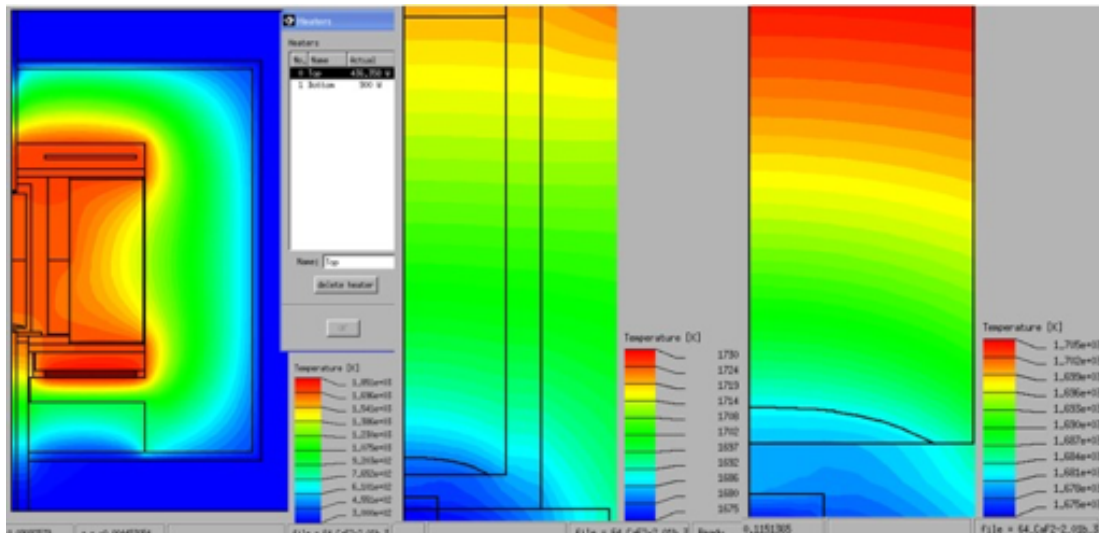


Figure 2.3: Numerical simulation of the temperature field and the shape of the phase boundary. This image shows the end of the growth, where the slightly convex phase boundary is already close to the top of the furnace (visible in the middle and right section of the image). In this simulation, the power in the lower heating meander was maintained at 1500 W, whereas the power in the upper heating meander was lowered by 183 W until the end of the growth process (when the phase boundary reaches the top).

parameters which require a change of the hardware, e.g. removing /replacing the shape or material of parts of the furnace, and soft parameters, which can be altered otherwise, e.g. heating powers and gas composition [59]. Finally, variables like temperature but also heat flux and flow velocity are calculated. It can therefore be classified as a process model which, in contrary to defect models, do not describe the relations between growth conditions and the formation of crystal defects [59]. An overview of numerical simulations of crystal growth can be found in [59] and [66].

Dopants were not considered in the numerical simulations, since it was assumed that the thorium concentration is so low that the material properties would not deviate significantly from those of pure  $\text{CaF}_2$ . Most importantly, the first  $^{232}\text{Th}$ -doped calcium fluoride crystal (section 3.5.2) showed sufficiently high doping concentrations and satisfying transmission properties.

## 2.2.4 Thermal insulation

The stainless-steel housing of the furnace is water-cooled and keeps its temperature rather constant during the crystal growth. Carbon-based materials can be

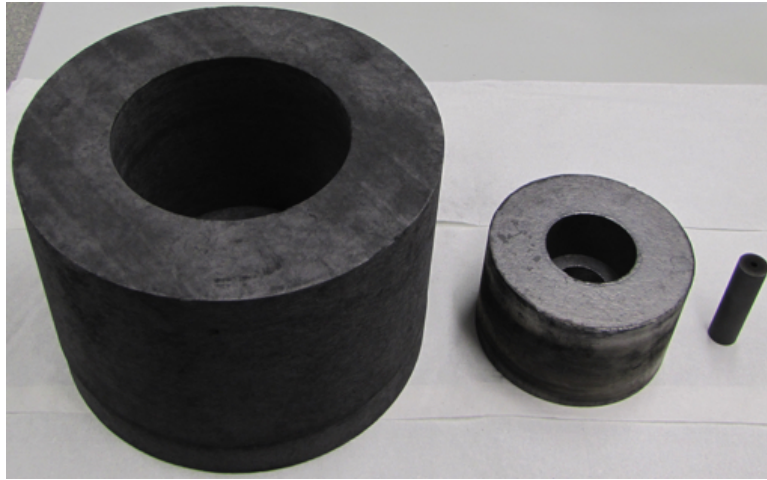


Figure 2.4: Thermal insulation of the furnace and crucible  
Two layers of carbon-bonded carbon fiber (left and middle, outer  $\varnothing$  of 294 mm and 160 mm) surround the crucible (right) during growth.

used inside of the furnace, where corrosive fluorine-containing compounds<sup>12</sup> and the high temperatures required for melting calcium fluoride, destroy most other materials. The thermal conductivity of those carbon materials varies over several orders of magnitude, depending on their density, inner structure etc. This offers enough flexibility for designing a thermal insulation around the crucible that keeps up the required temperature field for a stable crystal growth. Numerical simulations (section 2.2.3) were carried out by Dr. Kurt Semmelroth for several materials and configurations before installation.

The thermal insulation (fig. 2.4) consists mainly of carbon-bonded carbon fiber<sup>13</sup> (CBCF). The first sets supplied by Graphite Materials GmbH<sup>14</sup> did not provide the necessary purity, and considerable gas emission; a soft, dark deposit on the water-cooled furnace walls was the consequence. The thermal insulation was then baked out at 2000 °C by the producer which took 4 – 5 weeks but allowed a lower vacuum pressure and the growth of cleaner<sup>15</sup> crystals. Every change of the thermal insulation (even for the same supplier) slightly alters the temperature profile and requires new fine-tuning of the temperature set points.

The insulation tube around the lower vertical thermoelement, as well as the plate on which the crucible rests, are made of the harder and less porous isographite<sup>16</sup>.

---

<sup>12</sup>When the fluorine evaporated from the molten calcium fluoride reacts with the water in the residual atmosphere it forms HF.

<sup>13</sup>in German: Kohlenstoffhartfilz or Hartgraphitfilz

<sup>14</sup>alternative supplier for CBCF with similar properties: Calcarb

<sup>15</sup>Dark particles, supposedly coming from the graphite insulation in the furnace, were found in the first crystals.

<sup>16</sup>purity < 150 ppm, supplied by Graphite Materials GmbH

### **Temperature profile: experimental verification**

A movable thermoelement was used to measure the temperature along the vertical axis of the crucible to experimentally verify the temperature profile predicted by the simulations. A graphite dummy<sup>17</sup>, which has similar properties as a half-filled crucible, can be used. A constant gradient of 3 K/cm was measured whereas 70% (top) and 85% (bottom) of the available electrical power was used for heating to the maximum required temperatures.

The first crystals grown with these settings showed strange structures like a hole, that looks like a frozen vortex, at the top (fig. 2.5). Measurements with an empty crucible instead of the graphite dummy showed that the temperature gradient is reversed in the lower part. With these settings, crystallization did not occur steadily from the bottom to the top as intended, but probably started in the middle and spread upwards and downwards from there. Only a temperature difference of more than 100 K between the upper and the lower vertical thermoelement could generate a steady temperature gradient from the top to the bottom. This behavior was neither reflected in the simulations nor in the measurements with the graphite dummy but might be explained by the high share of thermal radiation which can not penetrate the opaque graphite.

It also turned out that the heat flux through the lower parts of the furnace was overestimated by the numerical simulations.

### **Shape of the interface: experimental verification**

The shape and position of the solid/liquid interface for a given temperature profile are crucial parameters in the growth process. Especially seeding (section 2.3.5) requires a good control of the phase boundary's position. In order to experimentally verify the numerical results, a mechanical probe<sup>18</sup> that can be moved in the vertical direction was used. The idea is that the probe can penetrate the melt but not the crystal, thereby determining the position of the solid/liquid interface. Unfortunately, the influence of the probe on the temperature field was too strong in our compact furnace. Although sufficient time was attributed to thermalisation while slowly approaching the probe, the heat transfer from the probe to the crystal was strong enough to melt the latter. It was therefore not possible to mechanically sense the phase boundary position, and the probe was destroyed in one of the attempts.

---

<sup>17</sup>massive graphite in the lower half of the crucible, contains a hole for the thermoelement

<sup>18</sup>made of glassy carbon

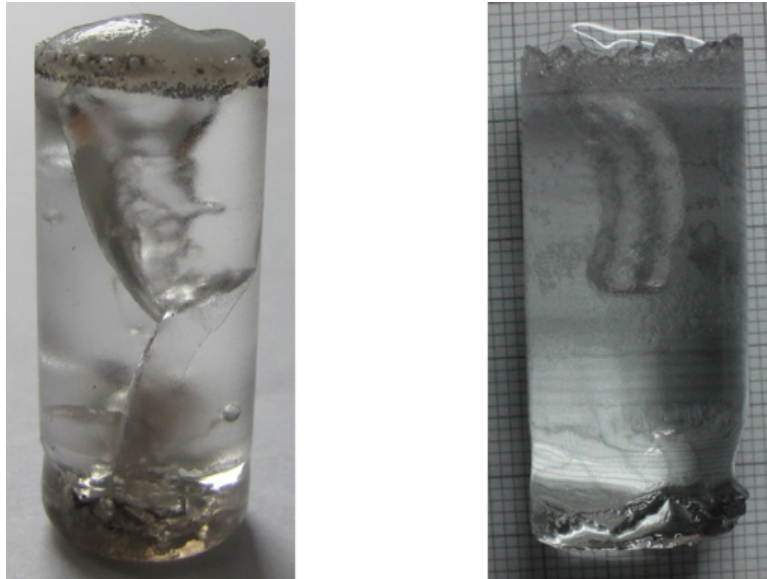


Figure 2.5: Undesired crystallization direction

The growth process of crystal on the left was aborted so that a rapid temperature drop occurred. The frozen vortex is the result of an inwards-directed, fast crystallization. For the crystal on the right, the axial temperature was too low during growth, yielding a similar result: a hollow channel in the top part.

### 2.2.5 Crucible

The influence of the crucible material on the shape of the phase boundary in a vertical Bridgman configuration was investigated in [67]. It was shown, that it is dominantly influenced by the crucible's thermal conductance near the crucible wall. The crucible's thermal conductance should be significantly smaller than that of the crystal but similar to the one of the melt.

$\text{CaF}_2$  is chemically unstable at the melting point and the fluorine has a high chemical activity at these temperatures. The material of the crucible, which is in direct contact with the melt and the evaporated fluorine gases, must therefore be able to chemically withstand these conditions. The material must have a low partial gas pressure and should not release contaminants into the melt. Its surface has to be sufficiently smooth to avoid spontaneous nucleation at the crucible wall. The crucible material of our choice is graphite<sup>19</sup>.

Vacuum pumps that are able to provide a sufficiently low pressure inside the furnace compensate to a certain degree the inevitable leakages in the chamber. Nevertheless, oxygen reduces the UV transmission already at the level of a few 10 ppm (section 4.1.1) and its transport into the crucible has to be reduced as

<sup>19</sup>EK94, purity < 10 ppm, supplied by CTG GmbH

much as possible. For small-diameter channels, the driving force behind the oxygen flow is determined by the slowest mass-transfer mechanism: the Knudsen type diffusion. It occurs at low pressures when the gas molecules collide with the channel walls more often than with each other, i.e. the mean free path of the molecules is longer than the channel diameter, and does not depend on the mean pressure. This minimizes the evaporation and decomposition of the melt at high temperatures by maintaining a certain pressure over it [40]. A high mass-flow resistance, in the form of (a) small-diameter channel(s), does not only prevent a strong inward flow of oxygen-containing contaminants but also minimizes the necessary outward-flow of undesired gases evaporated from the raw material, e.g. during the chemical purification of the scavenger process (section 2.3.4). A compromise between an open and a hermetically sealed crucible has to be found, and the best solution seemed to be a thread for screwing the lid on.

### 2.2.6 Heating and temperature control

Four resistive heating meanders made of carbon fiber-bonded carbon<sup>20</sup> (CFC) are placed two by two above and below the crucible (fig. 2.6). Each set of meanders can deliver a maximum power of 2 kW coming from a power transformer. Electric isolation between the heating meanders and the thermal insulation (both made of graphite) is provided by boron nitride plates. The electric feedthroughs for the heaters have to be air-cooled by fans outside of the vacuum system.

The temperature is measured by means of six thermoelements (further details in section 2.2.6). One thermoelement measures the temperature right above the crucible, one right below. They are referred to as “upper and lower vertical TE” (fig. 2.6) due to their orientation. They are not involved in the feedback mechanism for temperature control, but provide crucial data-output. The measured values of these thermoelements can be used for the manual temperature fine-tuning near the melting point (2.3.5). Feedback temperature control is carried out by means of two pairs of horizontal thermoelements (fig. 2.7), which are placed in the graphite insulation surrounding the crucible (fig. 2.6). A feedback-loop compares the temperatures set by the control software with those measured by the horizontal TEs. Those values are not fully reproducible since they are in a region with a steep temperature gradient, and the materials in the furnace undergo changes due to the high temperatures and the corrosiveness of  $\text{CaF}_2$ . The thermal insulation wears and can be in slightly different positions (gap for thermal expansion). The same is true for the thermoelements.

The PID parameters of the feedback control are optimized for temperatures around the melting point which can lead to strong oscillations for low temperatures, especially in the upper heating meanders (see section 2.3.3).

---

<sup>20</sup>kohlefaserverstärkter Kohlenstoff





Figure 2.6: Lower heaters and position of the lower thermoelements  
The lower heating meanders are electrically insulated by boron nitride plates (white). The white Alsint tip of the lower vertical thermoelement can be seen between the heaters. The TE is surrounded by an insulation tube made of isographite. The lower horizontal TE, whose end is hidden in the thermal insulation beneath the heaters, can be seen at the top of the picture.

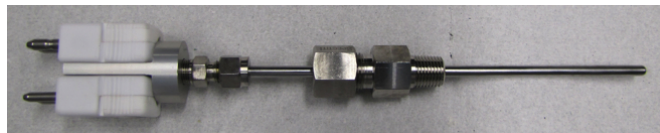


Figure 2.7: Horizontal thermoelement  
consists of two thermocouples  $W_{0.5}Re-W_{0.26}Re/C$  in a Molybdenum tube. The vacuum feedthrough is visible as well.

## Thermoelements

A thermoelement consists of one or two thermocouple(s) that are housed in a protective tube.

A **thermocouple** consists of two wires of materials with different thermo-electrical properties, connected at one point (point of measurement). The temperature difference between the point of measurement and a point of reference, outside of the furnace, causes a material-dependent electromotive force in each wire. The temperature difference is thereby translated into a voltage between the ends of the wires (Seebeck effect).

The thermocouple's materials in the vertical TEs are platinum +30% rhodium and platinum +6% rhodium (short: PtRh30-PtRh6/B, where B is an alternative short form for the type of the thermocouple). Temperature deviations are  $\pm 4^\circ\text{C}$  in the range of  $600^\circ\text{C} - 800^\circ\text{C}$  and  $\pm 0,005 \cdot |t|$  in the range of  $800^\circ\text{C} - 1700^\circ\text{C}$ , where  $|t|$  stands for the temperature at the point of measurement. The horizontal TEs (fig. 2.7) are fabricated by Günther GmbH, each consisting of two thermocouples Wo5Re-Wo26Re/C in a Molybdenum tube<sup>21</sup>.

The **protective tubes** for the vertical TEs are made of Alsint<sup>22</sup>, a ceramic with a refractoriness up to  $1800^\circ\text{C}$  and high thermal conductivity. However, the material deteriorates with every growth process. When in contact with graphite, a chemical reduction to elementary aluminum, which has a lower melting point, is also possible<sup>23</sup>. This leads to a material loss and a deformation of the Alsint tubes, which require regular checks before and after each growth process.

### 2.2.7 Vacuum

The pressure during the crystal growing process should be as low as possible in order to avoid oxygen contamination that reduce the UV-transparency [56]. Ideally, a pressure in the range of  $10^{-6} - 10^{-5}$  mbar is favored. Our furnace, however, has quite a lot of limitations when it comes to achieving such low pressures (described in the following). Typically, pressures are in the  $10^{-4}$  mbar range, often reaching  $10^{-3}$  mbar at the highest temperatures around the melting point of calcium fluoride.

In principle, crystal growth under a very pure argon atmosphere is possible with our furnace. However, in the numerical simulations this was never considered, and the temperature profile (and therefore the position and shape of the phase boundary) will probably be quite different.

---

<sup>21</sup>Only one functioning thermo couple is required for process control, the temperature measured by the other one can be checked for comparison on the displays of the transformer box.

<sup>22</sup>99,7%  $\text{Al}_2\text{O}_3$ , supplied by Buntenkötter Technische Keramik

<sup>23</sup>private communication with Frank Osthues, Buntenkötter Technische Keramik

## Possible leaks

The high temperatures together with the corrosiveness of calcium fluoride pose a challenge even for many chemically resistant materials. A corrosion-resistant pump proved to be absolutely necessary as well as regular material checks. The Alsint tubes of the vertical thermoelements have to be replaced after several growth processes.

Several weak spots in the vacuum system have been identified throughout this work. Strategies for finding leaks and a list of the usual suspects can be found in the group's wiki [68].

## Out-gasing

The graphite insulation can hold a lot of air and water between its fibers. Pumping times of a few hours, combined with heating to get rid of the water, are often required after the graphite insulation was exposed to air. It is important to use semi-conductor-grade insulation parts<sup>24</sup>. Otherwise, it can take weeks until the material completely gasses out.

There are a few measures that can help in reducing the pumping time. The graphite insulation must not get wet when cleaning the furnace. Even volatile solvents like acetone or isopropanol take a long time to get out of the pores completely. It is also recommended to switch off the water-cooling of the furnace<sup>25</sup> and fill the furnace with argon, when it is not in use.

The calcium fluoride powder is another possible source of water/oxygen contamination [40]. It has to be stored pure and dry.

### 2.2.8 Process control

The process control software<sup>26</sup> offers the possibility to divide the growing process into 30 **segments**. In each segment the temperature can be changed at a constant, user-defined rate or kept constant for a specified time. In the following, the names of the software links are written in *italic*.

Each segment requires the user to set the following **parameters** for both the lower and the upper heater (*Parameter*).

---

<sup>24</sup>impurities  $\ll$  200 ppm

<sup>25</sup>Air moisture might condense on the cold surfaces inside the furnace.

<sup>26</sup>a TwinCAT PLC Control<sup>©</sup> software, that was adapted to the furnace by the ZEW (Zentrale Elektronik Werkstatt) of the Friedrich-Alexander-University Erlangen-Nürnberg

- **Time** for which the temperature should be kept constant (hold-time)<sup>27</sup> [h, min, s]
- **Temperature** that should be reached by the end of the segment OR temperature which should be held constant for the specified time [°C]
- **Rate** with which the temperature should be changed<sup>28</sup> [K/min]
- **Tolerance** for switching from one segment to the next [%]: the temperatures<sup>29</sup> for both heaters have to be within the specified margin around the set point at the same time.

The parameters can also be changed for the segment that is currently processed (*Segment*) which is especially important near the melting point, when some fine-tuning by the user is required.

Furthermore, the control software allows setting the PID parameters of the temperature controller (*Regler*), recording data during the growth process (*Verlauf*) (section 2.2.9) and displaying occurred errors (*Alarme*). Some safety measures are integrated into the software (described in the following section) or can be controlled with it by setting thresholds (*Alarme*).

A more detailed description of how to use the control software can be found in the group's wiki [68].

### Software safety measures

The safety measures integrated into the control software allow it to be used in various crystal growth applications. They are often the reason for process abortions or undesired behavior and therefore treated in detail (both as failure prevention and as a troubleshooting guide) in the group's wiki [68].

#### 2.2.9 Data recording and analysis

The software iTools OPC Scope<sup>©30</sup> is used to display and record the latest data points of the (measured) process parameters:

- Date and time
- Pressure in the furnace

---

<sup>27</sup>A non-zero hold-time specifies the segment as a hold segment. When heating or cooling, the hold-time must be set to 0.

<sup>28</sup>A non-zero rate specifies the segment as heating/cooling segment. In a hold segment, the rate must be set to 0.

<sup>29</sup>measured by the horizontal thermoelements

<sup>30</sup>a program tool by Eurotherm, accessibly from the control software under *Verlauf*

- Measured temperatures of vertical and horizontal thermoelements
- Temperature set points for the horizontal thermoelements
- Number of the current segment
- Total and remaining duration of the current segment
- Opening status of the argon valve for emergency flooding of the furnace (section 2.2.10)

Since crystal growing is a rather slow business, it is enough to record the process parameters every 5 seconds, in order to avoid the accumulation of too much data for the analysis<sup>31</sup>.

A Matlab<sup>®</sup> program<sup>32</sup> was written for displaying the progression of the measured temperatures and comparing them with the set points of the process control. It also shows the pressure evolution in dependence of the measured temperatures. Furthermore, the program checks if data points were omitted, provides an overview of the process segments, their start time and duration (table of segment switching = toss) and allows the user to create tables and graphs of the measured temperatures vs. duration.

An Excel<sup>®</sup> sheet<sup>33</sup> provides an overview of the temperature set points, the heating/cooling rates, hold times and switching tolerances of all crystals grown in Vienna so far. This table is also very useful for the scheduling/time management of the growing process since the operator's presence is required when reaching the melting point of calcium fluoride (section 2.3.5). Another Excel<sup>®</sup> sheet<sup>34</sup> can be used for the temperature fine-tuning around the melting point.

The data analysis and presentation is essential for reproducing process conditions, since the set points differ slightly in each growing process and fine-tuning by the operator is required.

### 2.2.10 Hazards and safety measures

Hazardous chemicals and radioactive dopants that are involved in the growth process can pose a threat to the operator of the furnace as well as to certain

---

<sup>31</sup>The recording frequency can be increased to monitor faster changes, but the control computer has its limitations. If the parameter values are recorded every second the computer skips data points every now and then. A data point consists of all recorded process parameters of a specific time.

<sup>32</sup>named *Logdatadisplay-record2-VXXX.m*, where XXX stands for the number of the grown crystal. It can be combined with *bindatafunct.m* to create graphs and tables of the measured temperatures vs. duration.

<sup>33</sup>*process steps VXXX*, where XXX stands for the number of the last grown crystal

<sup>34</sup>*CG melting point adjustment.xlsx*

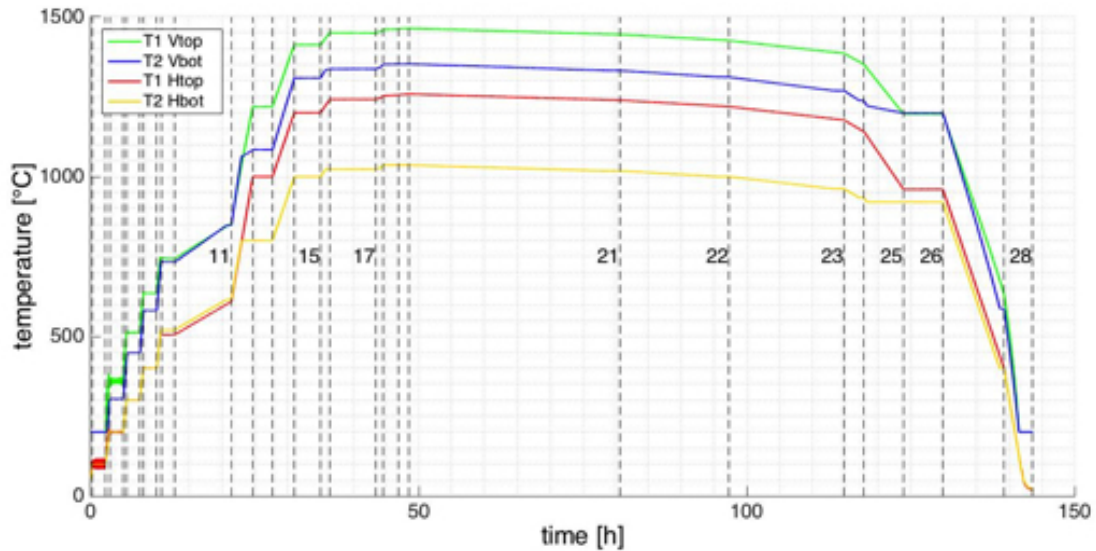


Figure 2.8: Process diagram of a typical  $\text{CaF}_2$  growth

The temperatures measured by four different thermoelements are plotted over time. The horizontal thermoelements (red and yellow) measure the temperature in the thermal isolation around the crucible and are used for process control (set points). The vertical thermoelements (blue and green) measure the temperatures directly above and below the crucible. Dashed vertical lines indicate switching points between segments:

- 1-10: Alternation of heat and hold segments (for restoring the pressure)
- 11: scavenger process
- 18-20: homogenizing and seeding
- 21-23: growth and slow cool-down with rates of 0.01 K/min, 0.02 K/min and 0.04 K/min
- 26: annealing

components of it. An overview, including installed safety measures, can be found in the group's wiki [68].

### 2.3 Process steps in the calcium fluoride growth

This section describes the steps in the growth process of a (doped)  $\text{CaF}_2$  crystal. A more detailed description of the furnace components can be found in the previous section 2.2, whereas a general introduction into crystal growth from the melt is given in section 2.1.

A diagram of the process steps can be found in fig. 2.8.

### 2.3.1 Process planning

Scheduling is the first step of the growth process since the operator's presence is required for the following process steps:

- switch-on and first heating segment(s): observe pressure evolution (section 2.3.3)
- heat to melting point, seeding and homogenizing: find the correct set points which change from one growth process to another (section 2.3.5)

Two to three days typically lie between these two steps, depending on the heating rate and the pumping time (section 2.3.3). The Excel<sup>®</sup> sheet *process steps VXXX* can be used for process planning. In the homogenizing phase (section 2.3.5) the settings can be checked to ensure a sufficiently long time for melting all of the calcium fluoride powder.

After the operator's corrections around the melting point, the process takes another three to four days to finish (fully automatic).

The Excel<sup>®</sup> sheet *CG melting point adjustment* can be used for manual temperature fine-tuning around the CaF<sub>2</sub> melting point.

### 2.3.2 Preparation of the furnace and the raw material

The components of the furnace should be checked for damage and eventually cleaned or replaced. Residues from the previous growth process have to be removed from the crucible. The seed, the CaF<sub>2</sub> powder<sup>35</sup> (and eventually the dopant) are weighed and filled into the crucible. Typically, a total amount of  $\sim 20$  g of CaF<sub>2</sub> powder is used in each growth process (CaF<sub>2</sub> powder plus dopant, seed is not included).

Detailed instructions for this step can be found in the group's wiki [68].

### 2.3.3 Drying

Water contained in the calcium fluoride powder and in the thermal insulation is thermally desorbed in the first heating segments. Heating of the furnace can be started when a sufficiently low pressure is obtained (on the order of  $10^{-4}$  mbar). Be aware that the pressure increases by at least one or even two orders of magnitude in the first heating phase due to out-gassing and evaporation of water.

In the following, we distinguish between set temperatures (measured by the horizontal TEs, see section 2.2.6) and temperatures directly above and below the

---

<sup>35</sup>typically with an admixture of 2% lead fluoride for the scavenger process (section 2.3.4)

crucible (measured by the vertical TEs). Both can be given in pairs, where the first value refers to the upper TE and the second to the lower TE. Remember that horizontal TEs are used for the process control by setting the temperatures that should be reached. These values correspond to temperatures measured in the outer insulation, but the relevant temperatures (measured by the vertical TEs) differ from process to process for the same set points. For the reader's convenience, the temperature set points are preceded with "SP" and given without units.

It is recommended to heat to SP 100/100 first and hold the temperature until a satisfying pressure is reached again, which typically takes 1 – 3 hours. Afterwards the temperature can be increased again in steps of  $\Delta\text{SP } 100/100$  with hold segments in between, during which the pressure is restored. The heating rate depends on the amount of water and residual gases, contained in the thermal insulation and the raw material for the crystal (typically 1 – 5 K/min)<sup>36</sup>.

The vertical TEs are not working below 200 °C<sup>37</sup>. The parameters of the feedback loop are optimized for maximum temperatures around the melting point of CaF<sub>2</sub>. Temperature oscillations<sup>38</sup> together with a bad vacuum pressure can be an indication that the thermal insulation needs to be replaced.

Most water contained in the thermal insulation of the furnace or the raw material evaporates in the first heating segment. Therefore the pressure maximum of the growth process is typically reached therein as well.

### 2.3.4 Scavenger process: chemical removal of oxygen

Oxygen is the most perturbing impurity in calcium fluoride since it drastically reduces the UV transparency already at a level of a few 10 ppm, making the crystal opaque below 200 nm at oxygen concentrations of about 100 ppm [56, 69] (details in section 4.1.1). It can be contained in the CaF<sub>2</sub> powder in the form of H<sub>2</sub>O or CaO. This remaining oxygen can not be thermally desorbed but has to be removed in a chemical reaction with lead fluoride (PbF<sub>2</sub>) at temperatures around 800 °C:

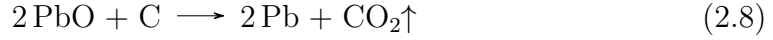
---

<sup>36</sup>If the heating rate is set too high and the evaporated gases can not be pumped away sufficiently, the pressure might increase above the safety limit (section 2.2.10) and the process is shut down while the furnace is flooded with Argon.

<sup>37</sup>An error message appears in *Alarme*. It will disappear automatically as soon as the TEs start measuring (typically between SP 100/100 and SP 200/200)

<sup>38</sup>Temperature oscillations with a peak-to-peak amplitude of more than 200 °C and a cycle period of 10 – 20 minutes have been observed in the upper heater for temperatures below 700 °C.





PbO is volatile and condenses at cold spots of the crucible where it is reduced to elementary lead by means of carbon (graphite). The resulting CO<sub>2</sub> is pumped away from the furnace.

In the growth process, the temperature is slowly increased from 750 °C to 850 °C in both heaters. Typical rates of 0.1 – 0.2 K/min ensure enough time at the required temperature for the chemical reactions to take place. Due to the low heating rate, an increase in pressure is barely detectable.

The PbF<sub>2</sub> is already contained (2wt%) in the CaF<sub>2</sub> powder supplied by the IISB Erlangen<sup>39</sup>.

### 2.3.5 Homogenizing and seeding

After the scavenger process the temperatures can be increased to values just a few degrees below the maximum temperatures<sup>40</sup>, which determine the lowest position of the phase boundary (the crystal grows upwards). Heat and hold segments can be alternated depending on the pressure evolution.

However, near the melting point some manual fine-tuning by the operator is required to adjust the temperatures so that only the upper part of the seed crystal, but all of the above-lying CaF<sub>2</sub> powder, is molten (seeding). The set points for reaching the desired temperature profile around the melting point differ from one growing process to another (between SP 1220/1020 and SP 1280/1070), depending mainly on the condition of the thermal insulation and the exact position of the vertical TEs. Even small displacements (1 – 2 mm) of the vertical TEs can cause the measured temperature to drop by a few degrees.

**Homogenizing** of the melt is achieved by keeping the temperatures slightly above the melting point for some time without significantly overheating any part of the melt. This phase should last long enough for completely melting the calcium fluoride powder and releasing the volatile contaminants but not too long as to cause melt decomposition. In larger furnaces that can hold more raw material, this can take a few hours. After homogenizing, the temperature can be briefly increased to partially melt the seed. The temperatures in our furnace are harder

<sup>39</sup>The raw material is the same one that was used in [56] for growing high-quality CaF<sub>2</sub> crystals.

<sup>40</sup>The exact values of the maximum temperatures depend on the exact position of the protective Alsint tubes of the vertical thermoelements.

to control due to its small size and the small resulting thermal inertia. The crystal volume is also very small, and homogenizing does not take that long. Therefore, homogenizing and seeding are not separated process steps but take place at the same time.

**Seeding** is the most difficult part of the growth process since the lack of optical access leaves only the temperatures measured by the vertical TEs as reference points. It is therefore essential to ensure that the protective Alsint tubes (section 2.2.6) are renewed when necessary, and that the vertical TEs are always in the same position (especially after replacing the Alsint tubes).

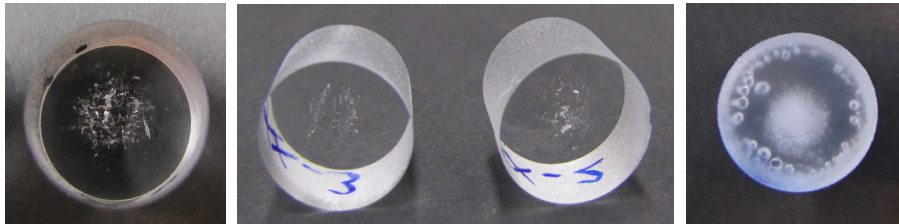


Figure 2.9: Crystals grown with a too low axial temperature gradient

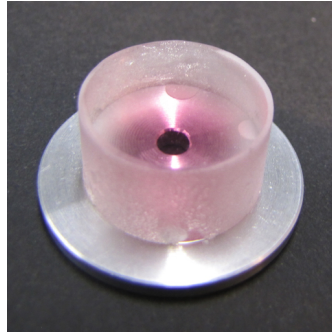
A few trial-and-error experiments were necessary to find suitable temperature settings for successful seeding (section 2.4).

The margin for the bottom temperature is only a few degrees (typically between  $1350^{\circ}\text{C}$  to  $1353^{\circ}\text{C}$ , measured  $3.0 \pm 0.5$  mm below the bottom of the crucible).

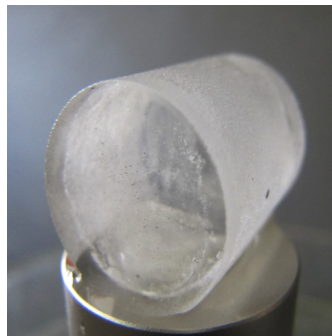
This also means that the axial temperature gradient is mainly determined by the upper heater. In our first growth attempts, the overall gradient was chosen too low and was even inverted locally in the lower part of the crucible (section 2.2.4). The crystals did not grow in the desired way or direction, since crystallization probably started on the outside (figs. 2.5 and 2.9). Only a temperature difference between upper and lower vertical TE of around 110 K ensured the growth of crystals without visible defects in their structure.

However, sometimes the temperature suddenly dropped by several degrees after a hold segment. This means, that the interface between melt and crystal shifted faster than during the desired growth conditions, which lead to irregularities in the crystal structure. It is therefore both safer and crucial for the crystal quality to split the part of the growing process, where the seeding and homogenizing occurs, into several heating segments and **renounce hold segments**. One can use the minimal heating rate of 0,01 K/min to keep the temperature nearly constant for hours. If the temperature change is still too large, one can alternate heating and cooling segments with minimal temperature change. However, one has to keep in mind that there can not be more than 30 segments during one growth process.

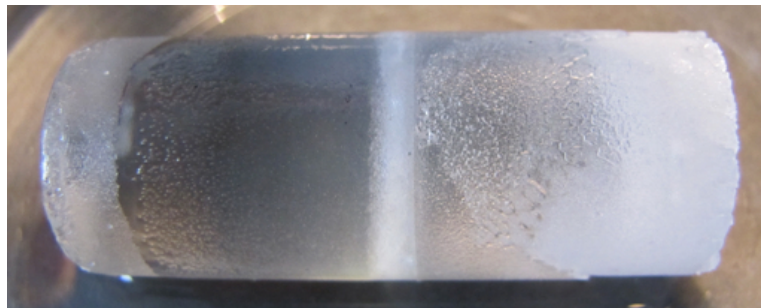
The best approach seems to slowly ( $0,1 - 0,5$  K/min) heat to the maximum bot-



(a)  $\text{CaF}_2$  after rapid cool-down in oxygen-containing atmosphere



(b) Incomplete seeding



(c) Incomplete seeding

Figure 2.10: Undesired growth conditions

(a) A vacuum leak occurred during growth of this  $\text{CaF}_2$  crystal, which caused a rapid cool-down at a pressure of  $> 0.05$  mbar. It remains unclear how much of the crystal had already solidified prior to the exposure to oxygen and the thermal shock. The pink coloring could have been caused by thermally induced crystal defects and/or increased oxygen content.

(b) The seed did not melt and is still clearly visible inside this crystal.

(c) A layer of incompletely molten  $\text{CaF}_2$  is visible between the seed (right) and the grown part of the crystal (left) of V038. The rough surface structure of the seed is the result of melt flowing into the gap between seed and crucible, and crystallizing in an uncontrolled way in this colder part of the crucible.

tom temperature (between 1350 °C and 1353 °C) and hold<sup>41</sup> it constant while increasing the top temperature from (1461 ± 1) °C to (1464 ± 1) °C. The heating rate for the top heater should be chosen accordingly so that the maximum bottom temperature is held between 1 – 4 h (typically 2 – 3 h), depending on the exact temperature measured by the lower vertical TE. The tolerance for segment switching should be set to the minimum value of 0,01% around the melting point, i.e. > 1400 °C/1300 °C. Together with the slow heating rate, this gives the operator enough time to make manual corrections to the temperature settings<sup>42</sup>.

Temperature alone is not the only crucial process parameter in this small furnace. The position of the phase boundary before the actual growth begins also depends on the time during which the CaF<sub>2</sub> was exposed to the high temperatures. Very similar temperature values, measured by the vertical TEs, can produce different crystals for different hold times, if in one case the seed was completely (or not at all) molten. A low bottom temperature can therefore be compensated to a certain extend (< 0,5K) by a longer hold-time. However, the time during which the furnace is kept at high temperatures should be minimized because of the material wear due to the corrosive CaF<sub>2</sub>.

In order to facilitate the adjustment of the parameters, but also the planning of the growing process, several software tools were developed (see sections 2.3.1 and 2.2.9). Especially the graphs and tables of previous (successful) growing processes, that show temperature vs. duration, can be very helpful for reproducing similar conditions.

The temperature control of our furnace, i.e. the feedback parameters, is optimized for temperatures near the melting point of calcium fluoride. For small temperature changes in that range, one can assume for both heaters that the difference between two set points is equal to the actual temperature difference in the furnace:

$$\Delta SP \simeq \Delta T \text{ for } T \simeq T_{melt}(\text{CaF}_2). \quad (2.9)$$

### 2.3.6 Crystal growth

In order to avoid thermal stress during the crystallization the same cooling rate is chosen for the top and the bottom heater. Thereby the axial temperature gradient is maintained and the phase boundary is slowly shifted upwards (typically at 0,01 – 0,02 K/min). The assumption 2.9 still holds in most cases but sometimes set point corrections of 1 – 2 K have to be made to keep the gradient unchanged.

---

<sup>41</sup>The temperature of **one** of the two heaters can be kept constant while the other one is still changing the temperature. This can be done by leaving the set point of one heater unchanged AND specify a **non-zero** heating rate. For the other heater, a set point that is different to the one of the previous segment has to be chosen as well as a non-zero heating rate.

<sup>42</sup>in *Segment*

The segment switching tolerances should be kept at the minimum of 0,01% in order to avoid sudden drops in temperature.

The growth phase is by far the most time-consuming part of the entire process. Assuming a temperature difference of 110 °C and a distance of 10 cm between the upper and the lower vertical TE, it takes more than 18 h for shifting the phase boundary by 1 cm at the minimum growth rate of 0,01 K/min.

### 2.3.7 Cool-down

The crystal is slowly cooled (0,5 – 1 K/min) to 1200 °C/1200 °C and the temperature is held there for 3 – 6 hours in order to anneal the crystal and minimize dislocations [56]. In some cases, crystals can be heated up to temperatures just below the melting point and cooled down thereafter in a homogeneous temperature field to avoid thermal stress [41].

During the subsequent cool-down the axial temperature gradient should be as flat as possible in order to minimize thermal stress. Both heaters are brought down to SP 400/400 at a rate of 1 – 2 K/min and finally to SP 20/20 at 2 – 4 K/min.

When opening the lid of the furnace, follow the check-list in the group's wiki [68].

## 2.4 Parameters for successful seeding

A major drawback of the vertical gradient freeze method compared to Czochralski growth is the lack of optical access to the crystal during growth. This especially poses a challenge during seeding, i.e. the part of the growth process during which the seed crystal is partially molten in order to provide a crystal orientation for subsequent growth. The appropriate temperature at the bottom of the crucible needs to be found, since it determines the position of the phase boundary (the temperature at the crucible's top just sets the axial temperature gradient for a fixed temperature at the bottom). With no way of mechanically probing where the solid/liquid interface occurs during growth (section 2.2.4), several trial-and-error experiments had to be carried out. Relatively long seeds (20 mm, compared to a resulting crystal length of 40 – 45 mm) have been used to increase the chance of reaching a satisfying position of the phase boundary.

Not all process steps are necessary for finding satisfying seeding conditions. Since the crystal quality is not crucial in these attempts, the scavenger process can be shortened/omitted, the heating rates increased and the pumping times shortened. Switching off the heaters after homogenizing and seeding so that crystallization occurs very fast and uncontrolled, leads to the creation of clearly visible defects in the crystal (fig. 2.5, left). However, the sudden temperature drop also creates

a lot of thermal stress, which can damage the seed crystal as well. Therefore, this rapid cool-down is not recommended for determination of the phase boundary. However, increasing the growth rate by a factor of 10 to 0.1 K/min shortens the entire process significantly.

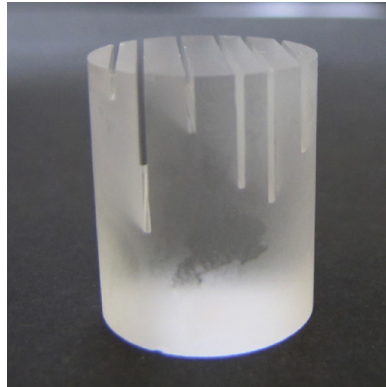
If the bottom temperature in the furnace was too low, the seed stayed intact and a layer of only partially molten  $\text{CaF}_2$  powder formed on top of it (figs. 2.10b and 2.10c). If the bottom temperature was chosen too high, the seed melted completely and there was no preferred crystal axis any more.

In order to determine if the bottom part of the seed was molten or not after the growth process, several ways of marking the seed were considered. Drilling holes of different lengths into the bottom was tried first. If the phase boundary reached the end of the hole, the melt would fill it up. The drill depth of the unfilled holes indicates how much of the seed remained solid. Our attempts of drilling into  $\text{CaF}_2$  crystals were mostly unsuccessful due to the crystal breaking apart.

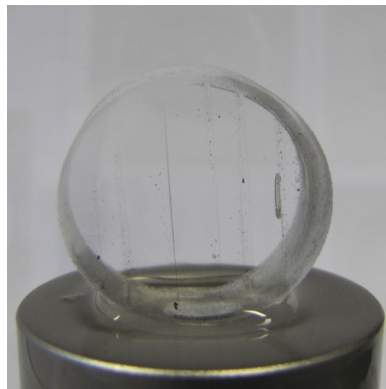
Cutting the crystals with a wafering blade on the other hand was a well-established procedure. First, cuts half-way through the seed were made normal to the cylindrical axis. In another attempt, the seed was sliced into discs with a height of a few millimeters that were stacked onto each other at the bottom of the crucible. After growth, these cuts were not always clearly visible (fig. 2.12) due to melt flowing in from the side.

Cutting marks were also made into the bottom part of the seed. The same idea like for drilling holes was implemented by varying the cutting depth (fig. 2.11a). Although the cuts were filled with melt, they could still be seen after growth (fig. 2.11b). Every time the phase boundary reached the end of a cut, the seed was effectively split up. These seed parts could easily be tilted with respect to each other due to the film of liquid  $\text{CaF}_2$  between them, resulting in multiple seeds with slightly different orientations. An easily recognizable pattern of 2 – 3 mm deep marks was therefore cut into the bottom of the seed. If the temperature at the bottom of the crucible is below the melting point of  $\text{CaF}_2$ , the crystallization of the melt flowing into the cutting marks occurs very fast and the pattern of the marks is therefore still visible after growth.

However, the marking method of making cuts into the seed bears a variety of problems for the crystal grown with this seed. The temperature profile in the crucible is changed due to the broken radial symmetry which can lower the crystal quality. When machining crystals, one always risks introducing impurities, defects or weaknesses in the crystal lattice due to mechanical stress. The heat transported by the melt that flows into the cuts can cause the seed to melt in undesired parts. The seed length is effectively reduced, and thereby the margin for the position of the phase boundary is decreased. Bearing that in mind, cutting marks can be used to gain more information about the position of the phase boundary before growth but should not be applied as a standard technique when crystal quality is



(a) Cutting marks in seed



(b) after growth

Figure 2.11: Cutting marks in the seed crystal before (a) and after the growth (b). Typically, cuts should not be deeper than 2 – 3 mm in order to avoid splitting up the seed when the phase boundary reaches down. In this case, the intention was to use the different cut depths for determining the lowest position of the phase boundary. Unfortunately, all the cuts were filled with melt (probably from the side).

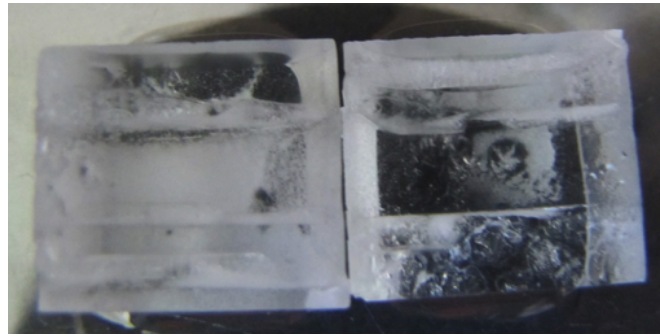


Figure 2.12: Remainder of the sliced seed

The result of an alternative approach, namely cutting the seed horizontally into slices, can be seen in the picture at the bottom (c). The remaining seed crystal was cut into two pieces along the cylindrical axis after growth. The slices were fused together by melt flowing in from the side but can still be distinguished in this crystal, which was not the case in other attempts.

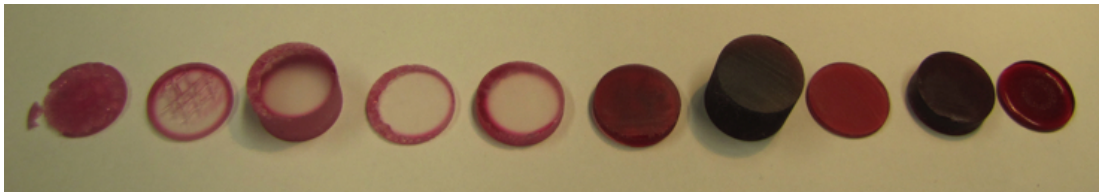


Figure 2.13: U:CaF<sub>2</sub> crystal V042 cut into 10 pieces

The five pieces on the left are the remaining seed crystal (transparent), where the markings are still clearly visible at the bottom. An increasing uranium concentration in the top parts of the crystal (on the right) yields the burgundy coloring. The U-containing crust around the seed originates from melt flowing down into the gap between seed and crucible. The uranium in this crystal has a natural isotopic distribution.



crucial. If changes are made to the thermal insulation, the thermoelements or the doping concentration in the crystal, a test run with a marked seed can provide useful information.

Another way of marking the phase boundary is to deliberately add impurities that are visible in the crystal after growth. However, any impurity will change the melting point of  $\text{CaF}_2$  to some degree. Graphite particles could be added to the  $\text{CaF}_2$  powder to distinguish the newly-grown crystal parts from the clean seed crystal. Uranium in different isotopic compositions was added as a dopant to  $\text{CaF}_2$  (section 3.2), which lead to an intense, burgundy coloring even for low doping concentrations. This did not only give insight into the dopant's distribution but also provided information about the success of the seeding (fig. 2.13).



### 3 Doping CaF<sub>2</sub> crystals

Doping of CaF<sub>2</sub> has been investigated extensively (both theoretically and experimentally) in the search for laser crystals. Mainly divalent and trivalent dopants have been studied, most of them lanthanides (e.g. Nd<sup>3+</sup>, Ho<sup>3+</sup>, Er<sup>3+</sup>, Yb<sup>3+</sup>, Sm<sup>2+</sup>, Dy<sup>2+</sup>, Tm<sup>2+</sup>) [70]. Uranium, an actinide like thorium, has been in the focus of laser research since 1960, when U<sup>3+</sup>:CaF<sub>2</sub> was described as a resonator material for generating stimulated infrared radiation [71].

Thorium has a high electropositivity of 1.3 Pauling, and is therefore expected to be integrated into the CaF<sub>2</sub> lattice as Th<sup>4+</sup>, showing a radon-like noble gas electron configuration. Doping CaF<sub>2</sub> with tetravalent ions is far less common in literature. In plutonium-doped CaF<sub>2</sub>, absorption lines attributed to Pu<sup>4+</sup> were reported, which are formed as the result of radioactive decay of the dopant [72]. In uranium-doped CaF<sub>2</sub>, the trivalent state is most common (section 3.2), but there is some controversy about the valence states of U<sup>2+</sup>, U<sup>4+</sup> and U<sup>6+</sup> (a brief overview is given in [73]). U<sup>4+</sup>:CaF<sub>2</sub> was suggested for passive Q-switching at wavelengths near 1.5 μm [74].

Thorium-doped CaF<sub>2</sub> crystals were grown to study the radiation damage to the crystal [75, 76]. The dopant was added in the form of ThO<sub>2</sub>, yielding a yellow coloring of the crystal and an absorption band around 400 nm.

In this chapter, doping CaF<sub>2</sub> with various dopants is described. Thorium-doping of CaF<sub>2</sub> crystals is introduced in section 3.1. Then, an alternative approach of populating the <sup>229</sup>Th isomer via alpha decay of <sup>233</sup>U is described in section 3.2. Zirconium was investigated as a dopant because it is a byproduct in one of our <sup>229</sup>Th samples (section 3.3). Cerium, as a stable dopant which is chemically similar to thorium, was doped into CaF<sub>2</sub> crystals for comparison (section 3.4). Neutron activation analysis and gamma spectroscopy were used in order to determine the absolute concentrations and distribution of thorium in our doped CaF<sub>2</sub> crystals (section 3.5)

#### 3.1 Thorium-doped CaF<sub>2</sub> crystals

Our experimental approach for future studies of the isomer transition in <sup>229</sup>Th consists of embedding thorium atoms into the ionic crystal lattice of calcium fluoride. Thorium-doping of CaF<sub>2</sub> is studied theoretically in section 3.1.1. Numerical calculations were carried out to predict how the thorium is integrated into the crystal

lattice.

Since  $^{229}\text{Th}$  is a very rare, artificial radioisotope, the doping process was studied experimentally by means of the chemically identical isotope  $^{232}\text{Th}$ . Doping  $\text{CaF}_2$  with thorium can be achieved by adding it as a fluoride ( $\text{ThF}_4$ ) to the  $\text{CaF}_2$  powder before growth.

The chemical preparation of the dopant, i.e. the conversion into  $\text{ThF}_4$  is briefly described in section 3.1.2. This preparation process was tested with the abundant isotope  $^{232}\text{Th}$  first. Crystals were doped with  $^{232}\text{ThF}_4$  that underwent the same chemical preparation later used for obtaining  $^{229}\text{ThF}_4$ .

Later in this chapter, the experimental determination of the obtained doping concentrations is treated in section 3.5.

### 3.1.1 Theoretical predictions for Th:CaF<sub>2</sub>

In the crystal lattice, thorium replaces  $\text{Ca}^{2+}$ , whose ionic radius of  $1.26 \text{ \AA}$  is similar to that of  $\text{Th}^{4+}$  ( $1.19 \text{ \AA}$ ) [38].

Ab-initio and empirical modelling was combined to calculate how thorium is incorporated into the  $\text{CaF}_2$  lattice and how the crystal's band gap is altered due to the doping. Special consideration was given to oxygen as a contaminant that negatively affects the UV transparency. Finally, it was shown how interactions between the crystal lattice and the nucleus affect the nuclear level structure of the isomer and the ground state of  $^{229}\text{Th}$ . A summary of the results presented in [39] is given in the following.

#### Computer models

GULP (General Utility Lattice Program) is an empirical atomistic modeling code used for calculating defect formation energies and solution energies with the required accuracy but a rather low computational effort. It uses a Buckingham potential supplemented by an electrostatic term to model interaction between atoms:

$$V(r) = A \exp(-r/\rho) - Cr^{-6} + \frac{q_1 q_2}{r_{12}} \quad (3.1)$$

where  $A$ ,  $\rho$  and  $C$  are parameters whose values are specified for each interaction between a pair of ions,  $q_1$  and  $q_2$  are the charges of the interacting ions and  $r_{12}$  the distance between them. The Mott – Littleton approximation is used, in which the region immediately surrounding the defect (radius  $10 \text{ \AA}$ ) is modeled explicitly, and approximations are used for more distant regions of the lattice.

The Vienna ab initio simulation package (VASP) uses hybrid Hartree–Fock density functionals to calculate the electronic structure of a periodically repeated cell containing 81 atoms, in which one calcium atom is replaced by thorium. This allows the determination of the band gap of thorium-doped  $\text{CaF}_2$  crystals as well as the effect of oxygen contamination.

## Modeling results

Comparison between experimental and modelled structures without doping show that the **lattice parameters** were reproduced to better than 1.5%, giving confidence in the used approximations.

The charge difference between  $\text{Th}^{4+}$  and the  $\text{Ca}^{2+}$  ion that is substituted requires **charge compensation** by either removing positive ions from the lattice, creating negatively charged calcium vacancies, or by adding additional negative charges. In the absence of oxygen, the latter occurs in the form of two fluorine interstitials ( $\text{F}_i$ ). Formation energies of these basic defects were calculated and combined to give the formation energy of Frenkel and Schottky defects.

GULP calculations, which allow comparing different stoichiometries, show that charge compensation by calcium vacancy creation (fig. 3.1a) is energetically less favorable than adding two fluorine interstitial atoms (fig. 3.1b-d). The defect formation energy shows a difference of a factor 5. Of the three possible configurations, the one where the fluorine atoms are at an  $90^\circ$  angle (fig. 3.1b) has the lowest solution energy. The result was confirmed by VASP calculations, comparing the three geometric configurations of fluorine interstitials (different stoichiometries can not be compared with this method).

The **crystal lattice** is slightly **deformed** by the insertion of  $\text{Th}^{4+}$  and the two additional  $\text{F}_i^-$  ions (fig. 3.2), leading to relaxations on the order of 5 – 10% of the bond length. The  $\text{F}_i^-$  ions move slightly towards the  $\text{Th}^{4+}$  ion, accompanied by an increase in **charge density** between them (fig. 3.3 left), whereas next-neighbour lattice fluorine ions are repelled by the  $\text{F}_i^-$  ions (fig. 3.3 right).

The VASP calculation results for the **electronic density of states** of  $\text{CaF}_2$  is shown in (fig. 3.4). It is known, that band-gaps of insulators like  $\text{CaF}_2$  are underestimated by the computer model and have to be rescaled by comparison with the experimentally determined value of 12 eV for  $\text{CaF}_2$ .

The **band gap** of  $\text{Th}:\text{CaF}_2$  (charge compensation with two  $\text{F}_i^-$  at  $90^\circ$ ) is reduced by 5.5% (fig. 3.5) compared to the undoped case, which is still large enough to be transparent in the expected wavelength region of the isomeric transition (section 4.1). The two additional  $\text{F}_i^-$  ions form electronic states that are located at the bottom of the gap. The empty Th states form the conduction band together with the unoccupied Ca states. At the top of the insulating gap, the unoccupied

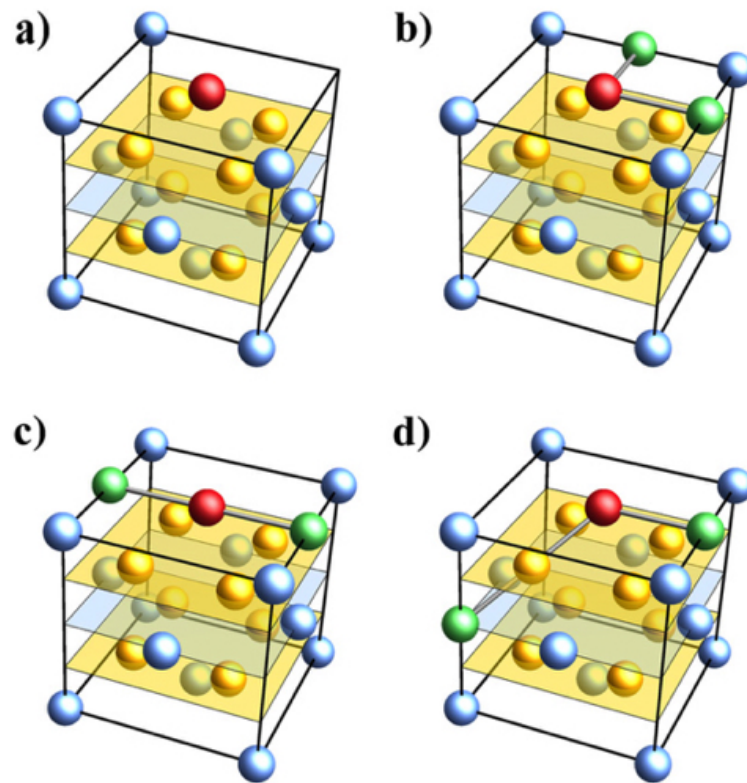


Figure 3.1: Charge compensation configurations for thorium-doping of  $\text{CaF}_2$ . Calcium ions are depicted in blue, fluorine ions on regular lattice sites are shown in yellow. The charge imbalance between  $\text{Th}^{4+}$  (red) and the  $\text{Ca}^{2+}$  ion it substitutes can be compensated by a calcium vacancy (a) or two fluorine interstitial atoms (green). The  $\text{F}_i^-$  can be arranged at an angle of  $90^\circ$  (b), in a linear configuration (c) or at an angle of  $125.3^\circ$  (d). Image taken from [39].

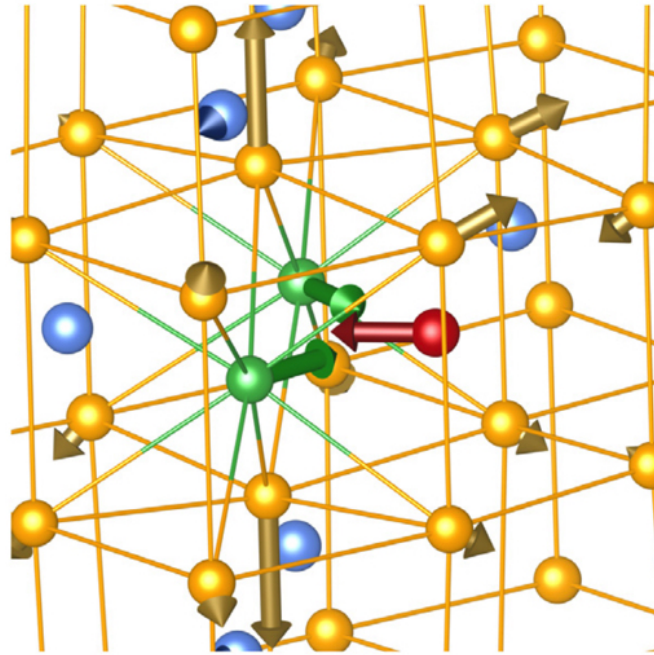


Figure 3.2: Forces acting on the atoms in thorium-doped  $\text{CaF}_2$

The configuration in which charge compensation was achieved by fluorine interstitials at an angle of  $90^\circ$  is shown. The arrows point in the direction of the lattice deformation, and the arrow length is proportional to the acting force.

The same colour code as in fig. 3.1 was used. Image taken from [39].

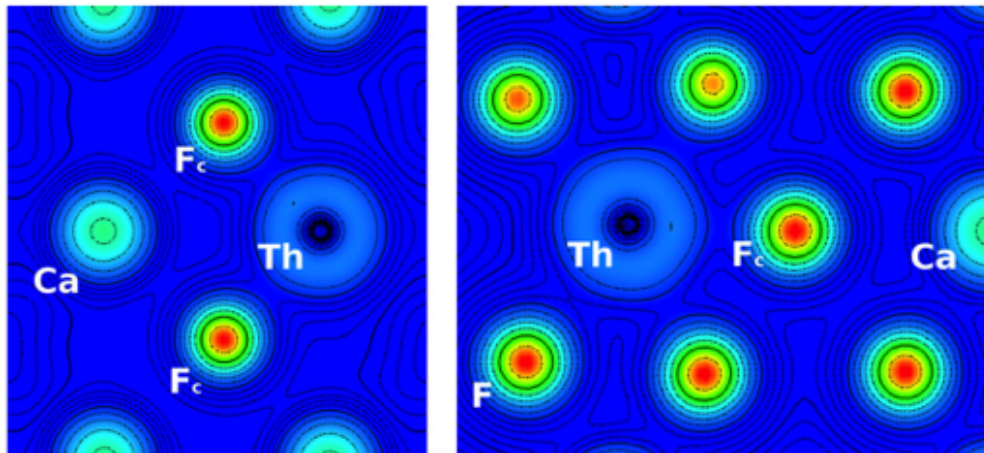


Figure 3.3: Charge densities around the dopant side of  $\text{Th}:\text{CaF}_2$

The configuration of  $90^\circ$  fluorine interstitials is shown for the  $(110)$ -plane (left) and the  $(01\bar{1})$ -plane (right). Further details in the text. Image taken from [39].

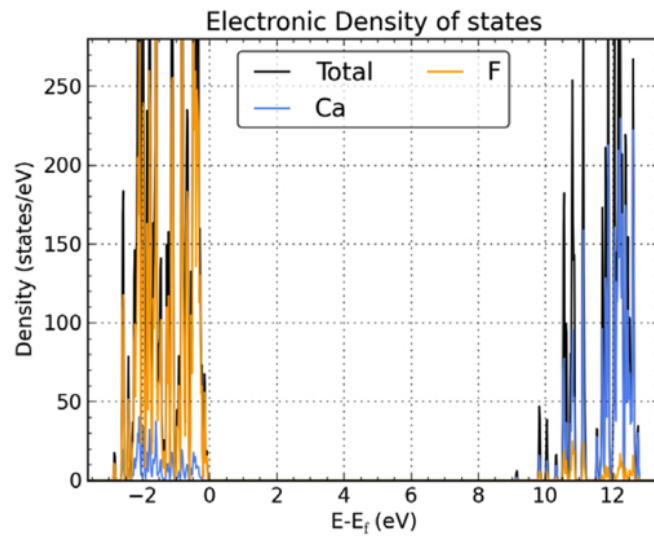


Figure 3.4: Density of states of undoped  $\text{CaF}_2$  per supercell which consists of 81 atoms or 27 formula units. The energies have to be rescaled to the well-known band gap of 12 eV in  $\text{CaF}_2$ . Image taken from [39].

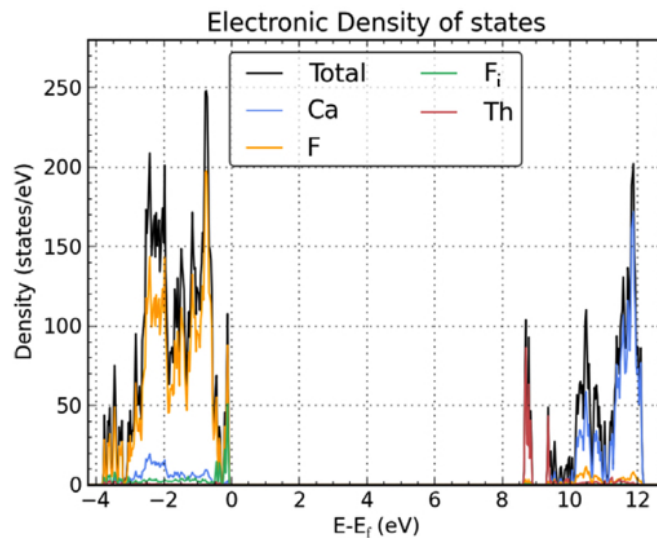


Figure 3.5: Density of states for Th-doped  $\text{CaF}_2$  with two additional  $\text{F}_i^-$  ions in the  $90^\circ$  configuration for charge compensation. The states of the two additional  $\text{F}_i^-$  ions appear at the bottom of the band gap. The empty 5f states of Th are slightly reducing the band gap compared to the undoped case. Image taken from [39].



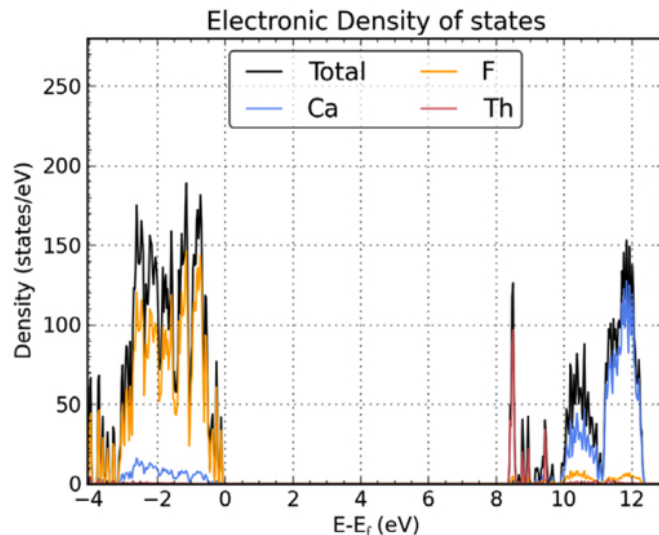


Figure 3.6: Density of states for Th-doped  $\text{CaF}_2$  with a calcium vacancy for charge compensation. The missing calcium atom reduces the density of the empty states above the band gap, which is reduced compared to the undoped case by empty 5f states of Th. Image taken from [39].

5f states of Th form a narrow band. The electronic density of states of both other  $\text{F}_i$  configurations look quite similar but the band gap is smaller. Charge compensation by a Ca vacancy yields similar results for the band gap (reduction by 8.2%) and the density of states (fig. 3.6), without the additional  $\text{F}_i$  states at the bottom of the gap.

**Oxygen** impurities can act as charge compensation ions for  $\text{Th}^{4+}$ , either replacing  $\text{F}^-$  ions or by creating interstitial ions or a combination of both (fig. 3.7). The band gap is significantly reduced due to the formation of electronic states created by the oxygen impurities (fig. 3.8).

### 3.1.2 Chemical preparation of $^{229}\text{ThF}_4$ as a dopant

Two samples<sup>1</sup>, one containing  $\sim 1 \cdot 10^{15}$ , the other  $7 \cdot 10^{16}$   $^{229}\text{Th}$  atoms, were purchased from Ecker & Ziegler. Thorium-229 is contained as thorium nitrate ( $\text{Th}(\text{NO}_3)_4$ ) diluted in 5 mL nitric acid ( $\text{HNO}_3$ , 0.1 mol/L), which also contains 50  $\mu\text{g}$  zirconium ( $\sim 3 \cdot 10^{17}$  Zr atoms) as a byproduct of the production process.

For doping thorium into  $\text{CaF}_2$  crystals, the  $\text{Th}(\text{NO}_3)_4$  has to be converted into thorium fluoride ( $\text{ThF}_4$ ). The chemical procedure described in [77] was applied. Since the amount of  $^{229}\text{Th}$  is too small to handle with standard chemical procedures,  $\sim 5$  mg thorium nitrate tetrahydrate ( $^{232}\text{Th}(\text{NO}_3)_4 \cdot 4\text{H}_2\text{O}$ ) were added

<sup>1</sup>isotopic composition: 75.6%  $^{229}\text{Th}$ , 23.9%  $^{232}\text{Th}$  and 0.5%  $^{230}\text{Th}$ ,  $^{228}\text{Th}$  is 0.4% of  $^{229}\text{Th}$

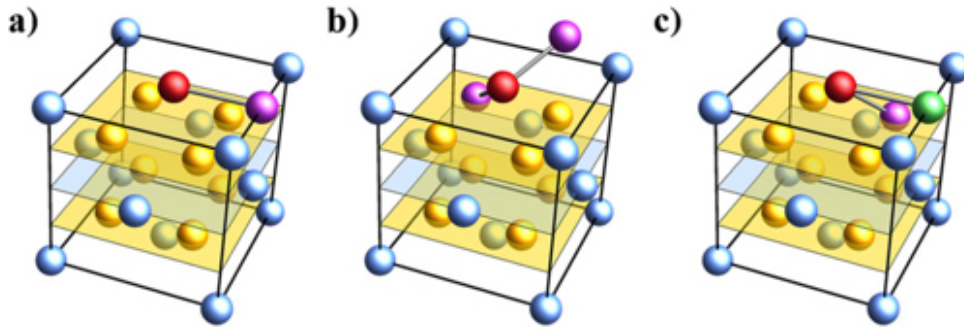


Figure 3.7: Charge compensation configurations in  $\text{Th}:\text{CaF}_2$  with oxygen present

Calcium ions are depicted in blue, fluorine ions on regular lattice sites are shown in yellow. The additional charge of the  $\text{Th}^{4+}$  ion (red), sitting on a  $\text{Ca}^{2+}$  lattice site, can also be balanced by an  $\text{O}^{2-}$  (violet) impurity interstitial (a), two  $\text{O}^-$  impurity ions substituting  $\text{F}^-$  ions (b) or by one  $\text{O}^-$  ion (violet) substituting an  $\text{F}^-$  ion and an  $\text{F}_i^-$  interstitial (green). Image taken from [39].

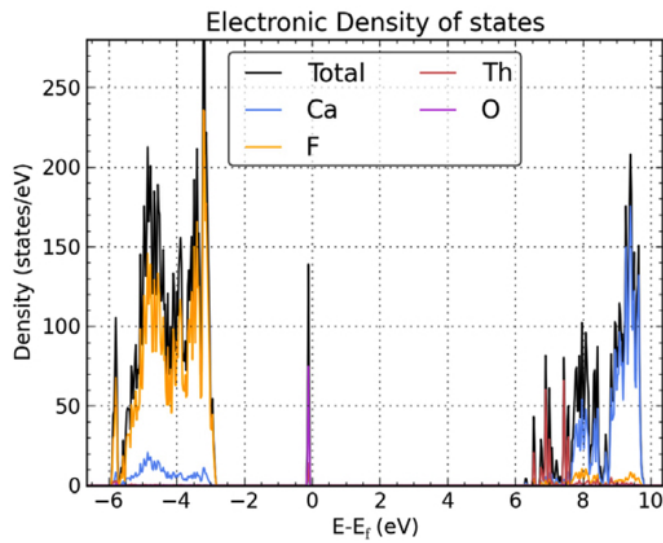


Figure 3.8: Density of states for with  $\text{O}^{2-}$  at an interstitial site. The additional oxygen ion forms a state within the gap, thereby reducing it by more than 30%. Image taken from [39].

( $\sim 5 \cdot 10^{18}$  <sup>232</sup>Th atoms).

The zirconium must be separated from the thorium, which can be achieved by anion-exchange. Thorium(IV) forms stable, negatively charged complexes with the nitrates of HNO<sub>3</sub>, whereas zirconium does not. An anion-exchange resin is used, to which the thorium-nitrate complexes attach, in contrast to zirconium, which can be eluted. The thorium is afterwards eluted with hydrochloric acid (HCl) since it forms no complexes with the chloride ions.

The elution of thorium was performed step-wise, and 8-10 fractions were collected in each elution step ( $\sim 3$  mL). A small part of each fraction (20  $\mu$ L) was used to measure the thorium and zirconium content by inductively coupled mass spectrometry (ICPMS, section 3.5.1). All samples containing thorium were then combined and concentrated to 1 – 2 mL. The precipitation of the white ThF<sub>4</sub> was performed with hydrofluoric acid (HF, 40%). Water was added to dilute the hydrofluoric acid, and the precipitate was separated by centrifugation. Afterwards, the ThF<sub>4</sub> was dried in the oven at 130 – 140 °C.

## 3.2 Uranium-doped CaF<sub>2</sub> crystals

This section treats an alternative approach of populating the <sup>229</sup>Th isomer in a crystal, namely via alpha decay of <sup>233</sup>U. After introducing the idea and motivation behind this approach (section 3.2.1), the chemical preparation of the dopant is described and a list of grown U:CaF<sub>2</sub> crystals is given in section 3.2.2. Finally, experimental challenges like background noise and features in the spectrum, that resemble the sought-after photon signal of the isomeric transition, are treated in section 3.2.3.

### 3.2.1 Indirect excitation of the <sup>229</sup>Th isomeric state in a bulk crystal

A detailed treatment of the idea and motivation behind this approach can be found in [78], a summary is given in the following.

Direct optical excitation of the <sup>229</sup>Th isomeric state poses a number of challenges. The **uncertainties** of the isomer lifetime and energy are very large, requiring an extensive two-dimensional search. The only **light sources** in the VUV region which offer both, a sufficient tunability and intensity in a small spectral range, are synchrotrons, for which beam time is precious and the spectral power is still several orders of magnitude smaller compared to diode lasers in the visible range. The excitation light causes the crystal to emit photons with a longer wavelength, often with a significant delay after the crystal was illuminated. This **photoluminescence** (section 4.2.2) acts as background noise in the search for the the nuclear signal, potentially masking it.

$^{229}\text{Th}$  is produced via the alpha decay of  $^{233}\text{U}$ , which has a half-life of 159200(2) a, and decays in a relatively short time in comparison ( $^{229}\text{Th}$  half-life: 7932(28) a) [79]. The available amount of  $^{229}\text{Th}$  atoms is therefore very small and the doping concentration in  $\text{CaF}_2$  is limited (section 3.5.2).

Various experiments using  $^{233}\text{U}$  have been or are still carried out (references in [78]). The population of the isomer via alpha-decay of  $^{233}\text{U}$  is well-separated both in time and space from the UV photon detection in all these experiments, in order to get rid of the background noise caused by radioluminescence. Typically, a UV-transparent crystal is brought close to the  $^{233}\text{U}$ -containing source, where the crystal absorbs  $^{229}\text{Th}$  recoil nuclei. The penetration depths in both the absorber and the uranium source are on the order of 10 nm, limiting the signal contribution to thin surface regions of the absorber and the source. The band gap of the crystal's surface region might be smaller than the isomer energy, allowing it to de-excite via electronic states [18, 80]. Depending on the surface roughness and contamination, the recoil ions might be stopped before reaching the crystal bulk structure.

An alternative experimental approach for the excitation of the isomeric state and the detection of its relaxation to the ground state via photon emission is provided by doping  $\text{CaF}_2$  with  $^{233}\text{U}$ . The alpha decay of  $^{233}\text{U}$  is followed by a gamma cascade and 2% of the  $^{229}\text{Th}$  daughter nuclei are predicted to end up in the isomeric state [81]. The accompanying radioluminescence (mainly caused by the alpha decay) is expected to be spectrally separated from the isomeric photons and therefore be reduced by filtering. The photonic deexcitation of the isomer can be observed without requiring direct excitation/knowledge of the energy of the isomeric state. Measuring the wavelength of the VUV photon with a spectrometer could reduce the present energy uncertainty to a degree that would allow to commence laser spectroscopy.

Doping  $^{233}\text{U}$  directly into a  $\text{CaF}_2$  crystal allows to increase the production rate of  $^{229}\text{Th}$  recoil ions, which will be directly introduced into the bulk of the crystal lattice. Continuous signal integration is possible for this experimental approach and it does not require knowledge of the isomer lifetime. The volume of the crystal, that contributes to the signal, is given by how far UV photons can travel in the crystal volume before they are absorbed. The optical properties of uranium-doped  $\text{CaF}_2$  allow to make use of a much larger part of the crystal than in the case, when  $^{233}\text{U}$  atoms are only implanted into surface regions (further details in section 3.2.3). Estimations show that uranium-doped crystals offer a maximum isomeric photon emission rate that is a factor 160 higher compared to the surface implantation technique.

### 3.2.2 Growth of U:CaF<sub>2</sub> crystals

Uranium-doped CaF<sub>2</sub> crystals have mainly been studied as optical medium for infrared lasers (emission lines between 2.2 μm and 2.6 μm). Most commonly, U:CaF<sub>2</sub> crystals show a ruby colouring, attributed to U<sup>3+</sup> ions in the crystal lattice. Green and yellow U:CaF<sub>2</sub> crystals, with absorption bands attributed to other valence states or different charge compensation mechanisms, have also been studied (overview in [73]). A model for the reduction mechanism from tetravalent uranium (e.g. in dopants like UF<sub>4</sub> or UO<sub>2</sub>) to trivalent uranium in CaF<sub>2</sub> is given in [82]. Different charge compensation configurations in U<sup>3+</sup>:CaF<sub>2</sub> have been distinguished by optical spectroscopy measurements, which also considered the effect of gamma radiation and the oxygen content [83]. Depending on the amount of added PbF<sub>2</sub> as a scavenger for oxygen removal (section 2.3.4), charge compensation occurred either by O<sup>2-</sup> at a fluorine lattice site or by an F<sup>-</sup> interstitial. The crystals in the referenced material were grown by the vertical gradient freeze method<sup>2</sup> and showed an increasing doping concentration in the latter grown parts, clearly visible due to color gradient from bright red at the crystal's bottom to dark red towards the top [84].

#### Chemical preparation of UF<sub>4</sub> as a dopant

Like thorium, uranium has to be converted to the fluoride form (UF<sub>4</sub>) for doping into CaF<sub>2</sub>. The raw material for obtaining **uranium-233**, is uranyl nitrate UO<sub>2</sub>(NO<sub>3</sub>)<sub>2</sub> in a HNO<sub>3</sub> solution. The solution also contains several decay products of <sup>233</sup>U, most interestingly <sup>229</sup>Th.

In order to separate uranium from its decay products (thorium), an anion-exchange process is used [85, 86] (also see section 3.1.2). In nitric acid, the thorium(IV) forms stable, negatively charged complexes with the nitrates from HNO<sub>3</sub>, whereas uranium(VI) does not. The thorium-nitrate complexes attach to an anion-exchange resin, and the uranium can be eluted. Flushing with hydrochloric acid elutes the thorium because it forms no complexes with chloride ions. The use of mixed alcoholic-aqueous media (80% methanol and 20% of the desired acid) provides a much better separation of the two elements than without the alcohol.

The elution of thorium was performed step-wise, and several fractions were collected in each elution step. A small part of each fraction (20 μL) was used to measure the thorium and zirconium content by inductively coupled mass spectrometry (ICPMS, section 3.5.1). All samples containing either uranium or thorium were then combined, the alcohol evaporated and the remaining aqueous solution concentrated to 1 – 2 mL. The reduction to uranium(IV) was performed with sodium hydrosulfite (Na<sub>2</sub>S<sub>2</sub>O<sub>4</sub>). Addition of hydrofluoric acid (40%) gave a

<sup>2</sup>called temperature gradient technique (TGT) in the publications

blue-green precipitate. Water was added to dilute the hydrofluoric acid, and the precipitate was separated by centrifugation. Afterwards, the  $\text{UF}_4$  was dried in the oven at  $130 - 140^\circ\text{C}$ .

**Uranium-232** was purchased<sup>3</sup> as as uranyl nitrate in a  $\text{HNO}_3$  solution. The sample contained no thorium or other undesired impurities, so that no separation was necessary.

Since the amount of  $^{232}\text{U}$  is too small to handle with standard chemical procedures,  $\sim 6$  mg of uranyl nitrate hexahydrate ( $^{238}\text{U}(\text{NO}_3)_6 \cdot 6\text{H}_2\text{O}$ ) was added. The uranium solution was concentrated to  $1 - 2$  mL and sodium hydrosulfite was added to reduce the uranium(VI) to uranium(IV). Addition of hydrofluoric acid (40%) gave a blue-green precipitate. The hydrofluoric acid was washed away with water, and the  $\text{UF}_4$  was afterwards dried in the oven at  $130 - 140^\circ\text{C}$ .

### Grown U:CaF<sub>2</sub> crystals

Seven  $\text{CaF}_2$  crystals doped with  $^{238}\text{U}$  (3),  $^{233}\text{U}$  (2) or  $^{232}\text{U}$  (2) were grown with the vertical gradient freeze method. An overview is given in table 3.1, including the expected doping concentrations calculated from the masses of the raw materials. The doping concentration describes (a) how many microgram of the respective uranium isotope are contained per gram of  $\text{CaF}_2$ , (b) how many uranium atoms are expected per  $\text{cm}^{-3}$   $\text{CaF}_2$  and (c) the relative number of uranium ions compared to the calcium ions in the crystal. The mass of the dopant for V058 could only be determined with an  $2 - 3\%$  uncertainty.

Table 3.1: Expected uranium concentration in VGF-grown  $\text{CaF}_2$

crystal	dopant	mass of added $\text{UF}_4$ [mg]	expected U doping concentration		
			(a) [ $\mu\text{g}/\text{g}$ ]	(b) [ $\text{cm}^{-3}$ ]	(c) $N_{\text{U}}/N_{\text{Ca}}$
V042	$^{238}\text{U}$	100.55	2300-3700	$(2 - 3) \cdot 10^{19}$	$(8 - 12) \cdot 10^{-4}$
V043	$^{238}\text{U}$	20.8	480-770	$(4 - 6) \cdot 10^{18}$	$(2 - 3) \cdot 10^{-4}$
V044	$^{238}\text{U}$	2.5	60-90	$(5 - 7) \cdot 10^{17}$	$(2 - 3) \cdot 10^{-5}$
V048	$^{238}\text{U}$	7.23	170-270	$(1 - 2) \cdot 10^{18}$	$(6 - 9) \cdot 10^{-5}$
V049	$^{233}\text{U}$	3.83	90-150	$(7 - 12) \cdot 10^{17}$	$(3 - 5) \cdot 10^{-5}$
V050	$^{233}\text{U}$	8.03	190-310	$(2 - 3) \cdot 10^{18}$	$(6 - 10) \cdot 10^{-5}$
V058	$^{232}\text{U}$	4.2(1)	100-170	$(9 - 14) \cdot 10^{17}$	$(3 - 6) \cdot 10^{-5}$

The doping concentration was not experimentally determined since the success of the doping process was obvious from the ruby color of the crystals (fig. 2.13 and 3.9). The higher the amount of the added dopant, the darker the colour of the

<sup>3</sup>from Eckert & Ziegler

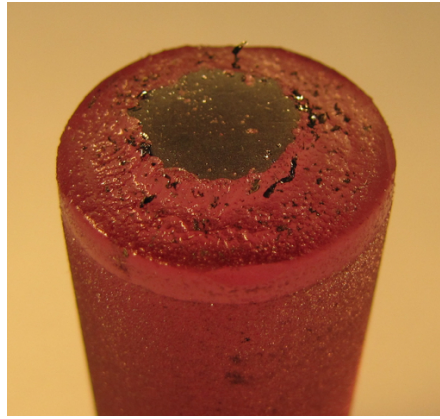


Figure 3.9: Lead from the scavenger process forms a film on the top of a crystal. This crystal (V044) was doped with 2.5 mg  $^{238}\text{U}\text{F}_4$ .

crystal. An increasing concentration gradient from bottom to top could also be observed with the naked eye due to the intense color.

### 3.2.3 Challenges of the experimental approach

A detailed treatment of the experimental challenges, summarized in the following, can be found in [78].

The number of isomeric photons is limited by the U: $\text{CaF}_2$  crystal's **UV transmission**. As a first step, a  $^{238}\text{U}$ : $\text{CaF}_2$  sample was prepared for transmittance measurements to ensure that the crystal allows a sufficient fraction of photons to pass through (section 4.1.4). The signal-contributing volume of the crystal is limited by the range of UV photons in the crystal volume before they are absorbed. The optical absorption length can be expressed by means of the uranium concentration  $n_U = N_U/N_{\text{Ca}}$  and the wavelength-dependent absorption coefficient  $\xi_U(\lambda)$ . For the achieved doping concentrations,  $\xi_U(\lambda)$  is independent of  $n_U$  and the optical absorption length becomes inversely proportional with the doping concentration:  $\xi_U(\lambda)/n_U$ . The absorption coefficient at 160 nm is determined to be  $\xi_U(160 \text{ nm}) = 6.3(8) \cdot 10^{-5} \text{ cm}$ . The penetration depth of a  $^{229}\text{Th}$  recoil nucleus is only about 15 nm in  $\text{UO}_2$ . This means, that only a very small volume of the  $^{233}\text{U}$  source contributes to the isomeric signal. The absorption coefficient is approximately 40 times larger than its equivalent quantity, the penetration depth of a  $^{229}\text{Th}$  recoil nucleus in  $\text{UO}_2$ .

The background noise in the form of **radioluminescence** is the second challenge in detecting isomeric photons. An alpha decay in  $\text{CaF}_2$  is followed by a photon burst consisting of  $10^5$  photons that are emitted from the crystal in a few  $\mu\text{s}$ , and can therefore be discriminated from isomeric photons by their temporal emission characteristics. Their spectrum shows a peak at 280 nm, which allows spectral

filtering in addition. Cherenkov radiation on the other hand also contains photons between 120 and 200 nm (details in section 4.2.3).

From the characteristic temperature-dependence of the emission rate [44] and their temporal distribution we conclude that the radioluminescence properties of U:CaF<sub>2</sub> are governed entirely by the general properties of CaF<sub>2</sub> and are not determined by the uranium doping. For more details see [78, 87], a summary of the results therein is given in section 4.2.3.

By far the largest uncertainty stems from the uncertainty in the **probability to populate the isomer** in the alpha decay of <sup>233</sup>U and the unknown magnitude of **competing non-radiative decay channels** in the deexcitation of the <sup>229</sup>Th isomeric state. The exact atomic configuration of the <sup>229</sup>Th nucleus in the crystal remains unknown, especially when considering the defect creation by the alpha particle and the recoil nucleus. It still has to be measured how many <sup>229</sup>Th end up in a suitable crystal environment that does not allow deexcitation via non-radiative decay modes.

Estimations including conservative values for the unknown parameters show that a measurement time of a few days to weeks can already be sufficient for the isomeric signal to exceed the noise of the background. This measurement is currently carried out in our lab.

**Spectrally narrow features with a long life-time** were found after exposing a CaF<sub>2</sub> crystal to gamma radiation or UV light. They could be easily confused with the emission of isomeric photons and we speculate that their origin are crystal contaminations. A way of excluding such signal is the comparison of crystals doped with different isotopes. Reference measurements can be performed with CaF<sub>2</sub> doped with <sup>234</sup>U, which is very similar to <sup>233</sup>U in terms of half-life (245000 a vs 160000 a), energy of the alpha radiation (4.86 MeV vs 4.91 MeV), and half-life of the first daughter nuclei (75000 a vs 7932 a). More details can be found in [78] and in section 4.3.

### 3.3 Zirconium-doped CaF<sub>2</sub> crystals

Our samples of <sup>229</sup>Th<sup>4</sup> contained Th(NO<sub>3</sub>)<sub>4</sub> in 0.1 mol/L HNO<sub>3</sub>. Zirconium (Zr) was present in the sample as a byproduct of the production process (10 μg/mL, ~ 3 · 10<sup>17</sup> Zr atoms in the 5 mL solution). In order to find out if and how the zirconium will be implanted into the CaF<sub>2</sub> crystal lattice, 57.8 mg of ZrF<sub>4</sub> were added to 33.3 g of CaF<sub>2</sub> before growth<sup>5</sup>. The experimental attempts to determine the doping concentration in the resulting crystal (V027) are described in section 3.5.2.

---

<sup>4</sup>purchased from Eckert & Ziegler

<sup>5</sup>19.3 g CaF<sub>2</sub> powder and 14 g CaF<sub>2</sub> seed



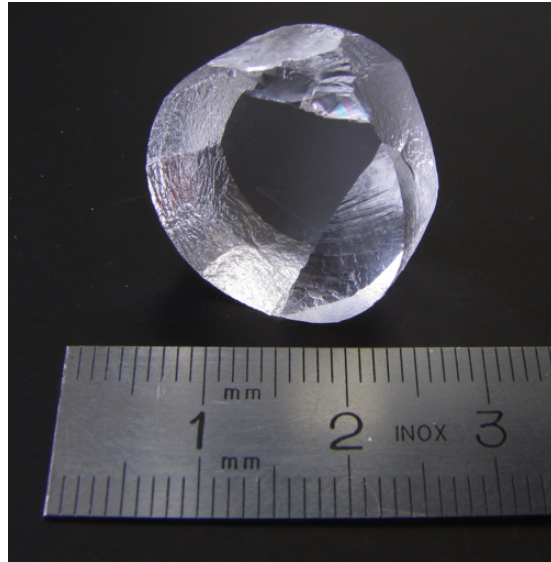


Figure 3.10: Ce:CaF<sub>2</sub> crystal grown by the Czochralski method  
Image taken from [89].

### 3.4 Cerium-doped CaF<sub>2</sub> crystals

Both oxidation states, the trivalent and the tetravalent, are common in ionic bonds with Cerium. The Ce<sup>3+</sup> ion has a very similar ionic radius of 1.283 Å compared to Ca<sup>2+</sup> (1.26 Å) [38], facilitating cerium-doping into CaF<sub>2</sub> [88]. The ionic radius of Ce<sup>4+</sup> (1.11 Å) is close to that of Th<sup>4+</sup> (1.19 Å) [38]. Furthermore, the most abundant cerium isotope <sup>140</sup>Ce is not radioactive. Cerium as a dopant in CaF<sub>2</sub> thus provides the opportunity for comparing thorium with a stable and chemically similar dopant. A Ce:CaF<sub>2</sub> crystal was therefore grown at the IKZ by the Czochralski method (fig. 3.10).

### 3.5 Experimental determination of the doping concentration

To date, no experimental way was found to determine the chemical environment of a thorium dopant site on the atomistic level. There are, however, ways to measure the doping concentration, i.e. how much thorium is contained per crystal volume/mass, on a macroscopic scale.

Doping concentrations are usually not homogeneous over the entire crystal. Integration of a dopant into a crystal lattice depends on the gain in entropy and/or the energy required for locally changing the crystal lattice. If the energy costs due to distorting the crystal lattice are too high, the dopant accumulates in the melt. In the worst case, a significant doping concentration would only be found at an (inner) surface of the crystal, e.g. dislocation, grain boundary, stacking fault,

or an interface with a precipitate or secondary phase within the solid.

Therefore, it is important to know how the dopant is distributed over the crystal. Depending on the growth technique (section 2.1), parameters like growth velocity, shape of the solid/liquid interface, temperature gradient etc., are different. The crystal grown by means of the Czochralski method is therefore treated separately from those grown later and in-house by the vertical gradient freeze method.

The various experimental techniques described in the following typically yield the mass of the dopant in the sample to be measured (sample tbm). The doping concentration can be determined with respect to the mass of the crystal ( $n_m$ ) and given in  $\mu\text{g/g}$  (ppm) or  $\text{ng/g}$  (ppb). Knowing the density of  $\text{CaF}_2$  ( $3.18 \text{ g/cm}^{-3}$ ) allows to specify the number of dopant atoms per volume ( $n_V$ ). The doping concentration can also be given as the relative number of thorium ions compared to the calcium ions in the crystal ( $N_{Th}/N_{Ca}$ ).

First, the experimental methods for determining the doping concentration are introduced in section 3.5.1, then the results of the measurements are presented in section 3.5.2.

#### 3.5.1 Experimental methods

##### Inductively coupled plasma mass spectrometry (ICPMS)

ICPMS is a type of mass spectrometry in which a plasma, that is inductively heated by an electromagnetic coil, atomizes and ionizes the sample. A mass spectrometer (often a quadrupole) is used to separate the ions by their mass-to-charge ratio. The concentration is quantified by measuring the ion current, which is proportional to the number of ions arriving at the detector, and comparing it to that of a certified reference standard.

##### Gamma spectroscopy

Nuclear energy levels, as well as transitions between them, are characteristic for each isotope. The gamma spectrum of every radioisotope therefore consists of a very unique set of gamma-ray energies that also have a characteristic intensity distribution (fig. 3.11). Like a nuclear fingerprint, they can be used to identify different radioisotopes in a sample. Comparison with the spectrum of a reference sample, for which the absolute quantities of the contained isotopes are known, can be used for a quantitative analysis. The intensities of the gamma lines in the reference spectrum are compared to those of the sample tbm. If the same measurement geometry was used (more details below), the ratio of the count rates  $C_\gamma$  (intensities) between reference and sample tbm is equal to the mass ratio:

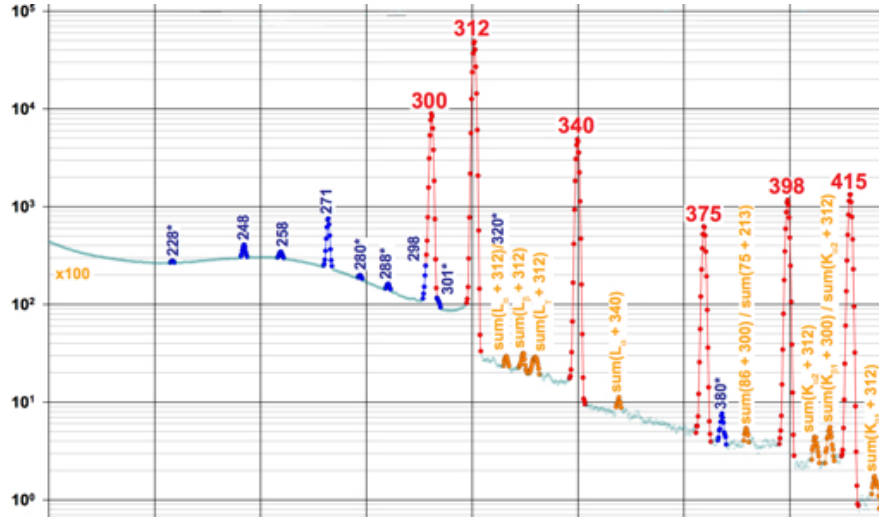


Figure 3.11: Gamma spectrum of  $^{233}\text{Pa}$   
Image taken from [90].

$$\frac{C_{\gamma, \text{sample}}(E)}{C_{\gamma, \text{ref}}(E)} = \frac{m_{\text{sample}}(X_E)}{m_{\text{ref}}(X_E)}, \quad (3.2)$$

where  $C_{\gamma}(E)$  stands for the count rate at the specific energy  $E$  and  $m(X_E)$  for the mass of the radionuclide  $X$ , emitting a gamma ray with the energy  $E$ .

The geometrical arrangement of the sample with respect to the detector plays a crucial role. Gamma radiation is emitted in all directions and the intensity therefore drops with  $1/r^2$ . The sample tbm and the reference are measured one after another and must be in exactly the same position during spectroscopy. For a quantitative measurement, the shape, size and distribution of the radioisotopes must be the same for the reference sample and the sample tbm. Sample holders out of plexiglas are transparent for gamma rays and ensure a reproducible positioning of the sample with respect to the detector.

The detection efficiency is not only influenced by the measurement geometry but is also energy-dependent. A calibration solution of known composition, together with a certified gamma spectrum for the solution, can be used to determine the concentration of radioisotopes, whose characteristic gamma energies are spread over the range of tens of keV to MeV (like the measurements in [91], described in section 3.5.2).

For different measurement geometries, a coarse determination of the activity in a sample can be achieved if the detection efficiency  $D_{eff}$  and the relative intensity<sup>6</sup>  $I_{rel}$  of a specific gamma peak are known. The activity  $A(t)$  is linked to the number

<sup>6</sup>a.k.a. branching ratio

of nuclei  $N(t)$  via the decay constant  $\lambda$ :

$$A(t) = \lambda \cdot N(t). \quad (3.3)$$

The decay constant  $\lambda$  is connected to the half-life  $t_{1/2}$  of the radioisotope by

$$\lambda = \frac{\ln(2)}{t_{1/2}}. \quad (3.4)$$

The number of nuclei  $N(t)$  in a sample can be therefore be determined by means of the measured activity  $A_{meas}(t)$ , which is given by

$$A(t) = I_{rel} \cdot D_{eff} \cdot \underbrace{\frac{\ln(2)}{t_{1/2}}}_{\lambda} \cdot N(t). \quad (3.5)$$

This approach neglects different measurement geometries between the calibration sample and the sample tbm. When measuring relatively large samples like entire crystals<sup>7</sup>, only an estimation of the order of magnitude can be obtained (section 3.5.2). These measurements require a sufficient gamma activity, and can therefore only be applied to  $^{229}\text{Th}$ , but not  $^{232}\text{Th}$  (an experimental method for measuring doping concentrations of  $^{232}\text{Th}$  is presented in the next section). After the alpha-decay of  $^{229}\text{Th}$ , only 5% of the decaying nuclei end up directly in the ground state of  $^{225}\text{Ra}$  (fig. 3.12). The other  $^{225}\text{Ra}$  nuclei go to lower nuclear energy levels under the emission of gamma radiation, which is characteristic for  $^{225}\text{Ra}$  and therefore for the alpha decay of  $^{229}\text{Th}$  (if other sources for the population of the excited nuclear levels of  $^{225}\text{Ra}$  can be excluded).

Gamma spectroscopy was performed with a germanium semi-conductor detector<sup>8</sup> (177 keV resolution of the 1332 keV  $^{60}\text{Co}$  peak; 33% relative efficiency), connected to a multi-channel analyzer with a pre-loaded filter and a loss-free counting system. Data analysis is carried out by means of a peak-search algorithm and comparison to the background radiation. The measurement time depends on the activity of the sample, the distance to the detector and the desired signal-to-noise ratio.

### Neutron activation analysis (NAA)

$^{232}\text{Th}$  decays via emission of an alpha particle and has a very long lifetime, resulting in a very small number of its daughter nuclei in the crystal. Neither  $^{232}\text{Th}$  nor

<sup>7</sup>typical height of 40 – 45mm and a diameter of 17 mm

<sup>8</sup>Ortec HPGe-gamma-detector

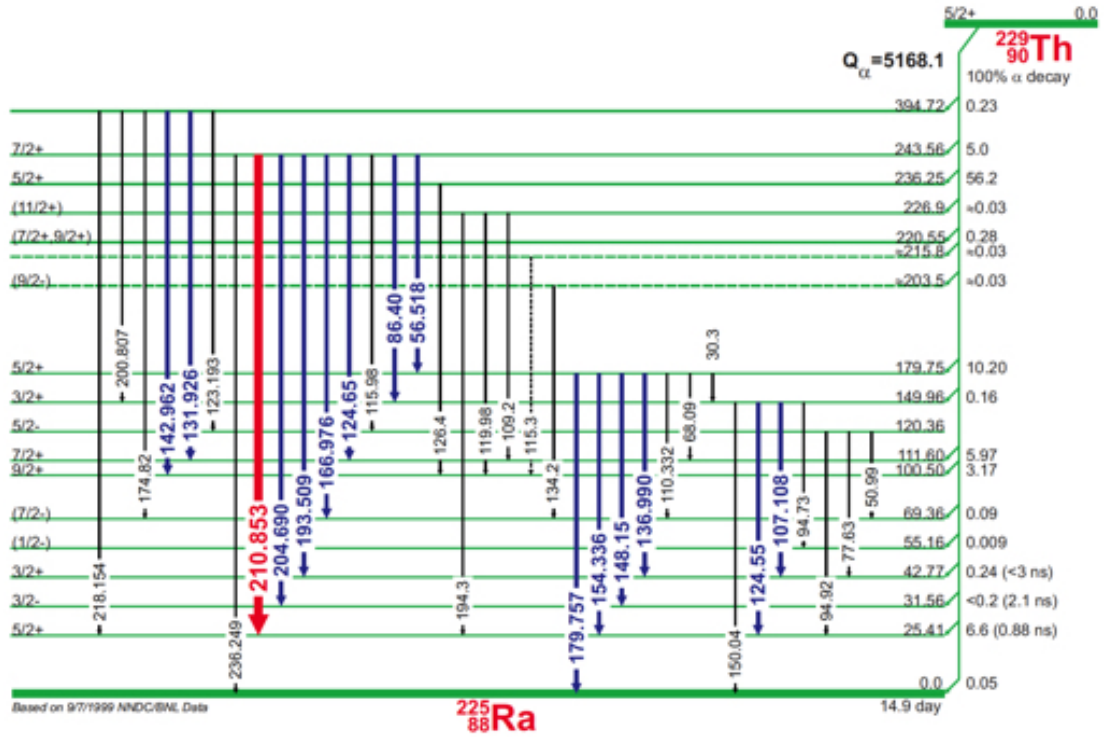


Figure 3.12: Gamma spectrum of  $^{229}\text{Th}$ . Transition energies are given in keV. For a coarse determination of the  $^{229}\text{Th}$  doping concentration, the gamma lines at 211 keV and 194 keV were observed. Image taken from [90].

its daughter products emit a sufficient amount of gamma radiation for obtaining a good signal-to-noise ratio in gamma spectroscopy. Neutron activation analysis is a measurement technique, providing an alternative for many non-radioactive nuclei and/or those who do not possess a rich gamma spectrum.

When nuclei are exposed to neutron radiation, they can capture a neutron, creating new, artificial isotopes. The probability of the process depends on the isotope-specific and energy-dependent cross section for neutron capture, the density and the energy spectrum of the neutron flux and the exposure time. Especially thermal neutrons  $n_{th}$ , which are also crucial for sustaining a stable chain reaction in a nuclear reactor, have a high probability to be caught:



where  $A$  and  $Z$  are the mass number and the atomic number of the element  $X$ . Typically, the newly-generated isotope is not stable and decays under emission of radiation, therefore the term ‘activation’. Depending on the half-lives of the daughter products, several decays can occur within a certain time, each emitting characteristic radiation. This radiation can be used to identify the different isotopes in a sample. In most cases, gamma radiation is detected (details in the previous section).

A reference sample, with a known isotopic composition<sup>9</sup>, can be irradiated together with the sample tbm. If the measurement geometry is the same for the sample tbm and the reference, comparison of the isotope-specific (gamma) intensities allow a direct mass determination of the isotopes in the sample tbm (from eq. 3.2):

$$m_{sample}(X_E) = \frac{C_{\gamma,sample}(E)}{C_{\gamma,ref}(E)} \cdot m_{ref}(X_E). \quad (3.7)$$

A big advantage of this method is the low quantity required for a measurement. Typically, the samples had a mass of 100 – 300 mg. In order to get homogeneous and representative samples, pieces of certain crystal parts were ground into a fine powder. A thin slice of  $\sim 1$  mm thickness can be cut off the crystal (cutting plane normal to the cylindrical axis). The disc is then divided into an inner part (bulk) and an outer part (surface), which were investigated separately, in order to get an idea of the dopant’s radial distribution. For such a thin disc, removing the outer layer (2 – 3 mm) of the crystal’s curved surface is done by scratching the crystal with a thin needle, introducing a predetermined breaking point thereby.

Thorium nitrate  $\text{Th}(\text{NO}_3)_4$  was used as a reference material, except for the measurements carried out by B. Ullmann [91], where thorium oxide ( $\text{ThO}_2$ ) provided

<sup>9</sup>The absolute quantity of each isotope of interest needs to be known.

an additional reference. The water content of the reference sample ( $\text{Th}(\text{NO}_3)_4 \cdot 5\text{H}_2\text{O}$ ) was taken into account in the analysis.

The samples *tbm* were irradiated together with the reference samples in the research reactor TRIGA Mark II at the ATI, with a typically neutron flux density of  $3 \cdot 10^{12} \text{ cm}^{-2} \text{ s}^{-1}$ . Eight samples *tbm* can be packed close together with a reference sample so that they are all exposed to the same neutron flux, which varies depending on the position in the reactor. The activity of the irradiated sample depends on the exposure time in the reactor and the mass of the activated radioisotopes in the sample. Activation usually took a few hours, except for the Zr-doped samples (section 3.5.2), which were irradiated for 40 hours (5 days, each with 8 hours of reactor operation time).

When  $^{232}\text{Th}$  captures a neutron, it turns into the short-lived  $^{233}\text{Th}$  ( $t_{1/2} = 21.83$  min), which decays to  $^{233}\text{Pa}$  ( $t_{1/2} = 27$  d). A waiting period of up to two weeks between activation and gamma spectroscopy was required to get rid of the short-lived daughter nuclei, whose activity can saturate the gamma detector. As soon as the reference samples, which contain the most  $^{232}\text{Th}$ , have a low enough activity, all the samples are measured in the gamma detector sequentially. The radioactive samples must be handled with caution by storing them behind lead shielding, minimizing exposure time and using long pincers for transport.

A correction factor is applied to the count rate to take the time between the individual measurements into account<sup>10</sup>. The count rate of the characteristic gamma energy  $E$  at the time  $t$  is given by:

$$C_\gamma(E, t) = C_\gamma(E, t = 0) \cdot e^{-\lambda t}. \quad (3.8)$$

In the analysis, the  $^{233}\text{Pa}$  gamma peak at 311.9 keV was used because it has the highest intensity in the spectrum (fig. 3.11).

### 3.5.2 Results

#### Czochralski-grown $^{232}\text{Th}:\text{CaF}_2$

Our first  $^{232}\text{Th}$ -doped  $\text{CaF}_2$  crystal was grown at the Institut für Kristallzüchtung (IKZ) in Berlin, using the Czochralski method (raw material: 100 mg  $\text{ThF}_4$  added to 142 g of  $\text{CaF}_2$ , growth speed: 1.5 mm/h). Since the crystal was pulled from the melt, only a fraction of the material (74.8 g) formed the crystal. Some part of the melt (67.2 g) remained in the crucible and crystallized there. A few pieces of it were analyzed, as well as certain parts of the crystal itself (fig. 3.13).

<sup>10</sup> $t=0$  for the gamma spectroscopy measurement of the first sample

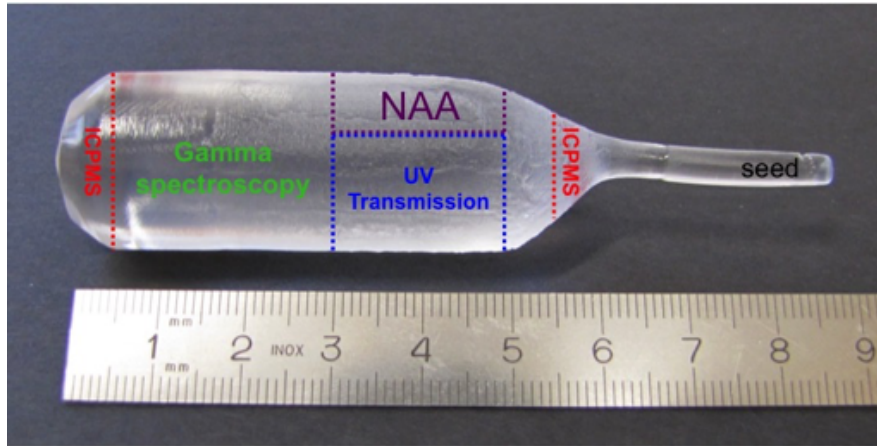


Figure 3.13: Czochralski-grown  $^{232}\text{Th}$ :  $\text{CaF}_2$  crystal

The image shows which parts of the crystal were investigated by the different measurement techniques described in the text. During Czochralski-growth the seed (right) was dipped into the melt (containing the dopant as well) and slowly pulled upwards so that the melt crystallized onto the seed. The crystal diameter was kept small in the beginning of the growth process so that defects could “grow out” of the crystal (section 2.1.2). By subsequently decreasing the pulling speed, the crystal diameter was increased.

ICPMS was carried out at the IKZ to determine the  $^{232}\text{Th}$  concentration in the crystallized melt and both end pieces of the crystal (fig. 3.13). The results can be found in table 3.2. The  $^{232}\text{Th}$  concentration in the crystallized melt was a factor of 2.00(9) or 2.66(8) higher than in the investigated end pieces of the grown crystal. An increasing doping concentration was obtained towards the end of the growth process. The doping concentration in the first-grown crystal was only 75% of the end piece’s concentration.

Table 3.2:  $^{232}\text{Th}$  concentration in Czochralski-grown  $\text{CaF}_2$  measured by ICPMS

	$[\mu\text{g}/\text{g}]$	$[\text{cm}^{-3}]$	$N_{\text{Th}}/N_{\text{Ca}}$
beginning of growth	219(3)	$1.81(2) \cdot 10^{18}$	$7.36(10) \cdot 10^{-5}$
end of growth	291(9)	$2.40(7) \cdot 10^{18}$	$9.78(30) \cdot 10^{-5}$
crystallized melt	583(10)	$4.81(8) \cdot 10^{18}$	$1.96(34) \cdot 10^{-4}$

Another attempt of determining the  $^{232}\text{Th}$  doping concentration of the crystallized melt and the Czochralski-grown crystal was made by gamma spectroscopy [91]. The energy-dependent detector efficiency was accounted for by means of a calibration solution. The activity ratio between the melt and the crystal was  $\sim 3.4$  for  $^{208}\text{Tl}$ ,  $^{212}\text{Pb}$  and  $^{224}\text{Ra}$ , comparable to the distribution of  $^{232}\text{Th}$ . However, the activity of  $^{228}\text{Ra}$  in the melt was  $\sim 15$  times higher than in the crystal, indicating that equilibrium was not yet reached in the decay chain and/or that the doping efficiency differed from element to element. Gamma spectroscopy alone



can therefore not be used to quantify the doping concentration of  $^{232}\text{Th}$ , but can help identifying impurities. However, no unexpected nuclei were found in the crystal.

Neutron Activation Analysis (NAA) on the other hand allowed a quantitative determination of the  $^{232}\text{Th}$  concentration [91]. Three samples of each, the crystallized melt and the Czochralski-grown crystal, were activated in ATI's Triga Mark II research reactor for three hours. After a cool-down period of nearly two weeks, during which the short-lived isotopes could decay, the samples were measured with the gamma spectrometer. Samples of  $\text{ThF}_4$  and  $\text{ThO}_2$ , which have a high and precisely known  $^{232}\text{Th}$  concentration, were activated too for providing a reference. Furthermore, multi-element standards were used attempting to identify impurities. The analysis of the 311 keV peak of  $^{233}\text{Pa}$  yielded the results presented in table 3.3. On average, the  $^{232}\text{Th}$  concentration in the crystallized melt was a factor of 2.77(5) higher than in the Czochralski-grown crystal.

Table 3.3:  $^{232}\text{Th}$  concentration in Czochralski-grown  $\text{CaF}_2$  measured by NAA

	$[\mu\text{g}/\text{g}]$	$[\text{cm}^{-3}]$	$N_{\text{Th}}/N_{\text{Ca}}$
crystal sample 1	219(2)	$1.81(2) \cdot 10^{18}$	$7.36(7) \cdot 10^{-5}$
crystal sample 2	210(2)	$1.73(2) \cdot 10^{18}$	$7.06(7) \cdot 10^{-5}$
crystal sample 3	220(2)	$1.82(2) \cdot 10^{18}$	$7.40(7) \cdot 10^{-5}$
<b>mean crystal</b>	216(2)	$1.79(2) \cdot 10^{18}$	$7.27(7) \cdot 10^{-5}$
cryst. melt sample 1	595(5)	$4.91(4) \cdot 10^{18}$	$2.00(17) \cdot 10^{-4}$
cryst. melt sample 3	603(5)	$4.98(4) \cdot 10^{18}$	$2.03(17) \cdot 10^{-4}$
<b>mean cryst. melt</b>	599(5)	$4.94(4) \cdot 10^{18}$	$2.01(2) \cdot 10^{-4}$

The exact position in the crystal from which the samples were taken is not precisely known (compare fig. 3.13). Only data of two (out of three) melt samples is available. The respective  $^{232}\text{Th}$  concentrations of both, the crystallized melt and the Czochralski-grown crystal, were very similar and confirmed the ICPMS results. Possible impurities, e.g. lanthanides like cerium or europium, could not be identified in any sample.

### VGF-grown $^{232}\text{Th}:\text{CaF}_2$

Typically, the crystals contain a few mg of  $\text{ThF}_4$  (V029, V034, V036 - V039) and are referred to as **lightly-doped**. For the given doping concentrations, it was assumed that either the seed was molten completely (lower value) or not at all (upper value). For the application of a solid-state nuclear clock, the number of thorium atoms in the crystal sample should be on the order of  $10^{14}$  [31].

Several  $^{232}\text{Th}$ -doped  $\text{CaF}_2$  crystals were cut into slices (compare fig. 3.22), some of which were used to determine the doping concentration by NAA. The results of the

Table 3.4: Expected  $^{232}\text{Th}$  concentration in VGF-grown  $\text{CaF}_2$ 

crystal	expected Th-232 doping concentration		
	$[\mu\text{g}/\text{g}]$	$[\text{cm}^{-3}]$	$N_{\text{Th}}/N_{\text{Ca}}$
V038	80-130	$(7 - 11) \cdot 10^{17}$	$(3 - 4) \cdot 10^{-5}$
V039	80-130	$(7 - 11) \cdot 10^{17}$	$(3 - 4) \cdot 10^{-5}$
V057	130-200	$(1 - 2) \cdot 10^{18}$	$(4 - 7) \cdot 10^{-5}$
V029	140-220	$(1 - 2) \cdot 10^{18}$	$(5 - 8) \cdot 10^{-5}$
V034	130-200	$(1 - 2) \cdot 10^{18}$	$(4 - 7) \cdot 10^{-5}$
V036	10-20	$(1 - 2) \cdot 10^{17}$	$(4 - 7) \cdot 10^{-6}$
V037	150-230	$(1 - 2) \cdot 10^{18}$	$(5 - 8) \cdot 10^{-5}$
V040	$(1.9 - 3.1) \cdot 10^4$	$(2 - 3) \cdot 10^{20}$	$(6 - 10) \cdot 10^{-3}$
V041	$(2.0 - 3.2) \cdot 10^4$	$(2 - 3) \cdot 10^{20}$	$(7 - 11) \cdot 10^{-3}$

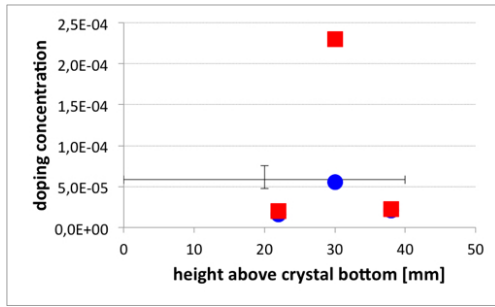


Figure 3.14: V029

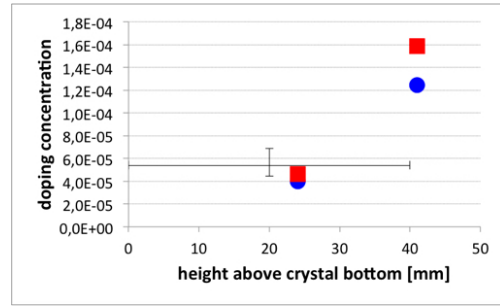


Figure 3.15: V034

$^{232}\text{Th}$  concentration in highly-doped  $\text{CaF}_2$  crystals measured by neutron activation analysis. The doping concentration ( $N_{\text{Th}}/N_{\text{Ca}}$ ) was determined separately for the bulk (red) and the crystal's surface (blue). The black vertical error bar marks the expected range of the doping concentration.

measurements can be found in figures 3.16 - 3.24. The low number of measurement points in some crystals are due to the time-consuming sample preparation and the long measurement time per sample. Furthermore, some parts of the crystals were needed for other measurements, e.g. transmission, luminescence etc, and were therefore not used for the destructive NAA. For comparison, the expected doping calculations (calculated from the masses of the raw materials) are given in table 3.4. For the values given in the table, it was assumed that either the seed was molten completely (lower value) or not at all (upper value).

During growth by the vertical gradient freeze method (VGF), a slightly convex phase boundary is preferred (section 2.2.2). If the dopant's integration into the crystal lattice does not work well, segregation can occur in the melt. In this case, the dopant would be pushed outwards (and upwards) to the crystal's surface by the moving phase boundary. Therefore, the bulk material was investigated separately by cutting off a few millimeter of the crystal's curved surface.

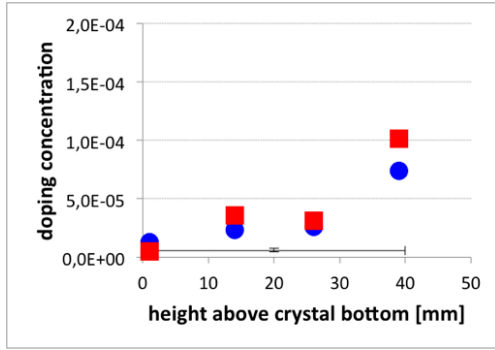


Figure 3.16: V036

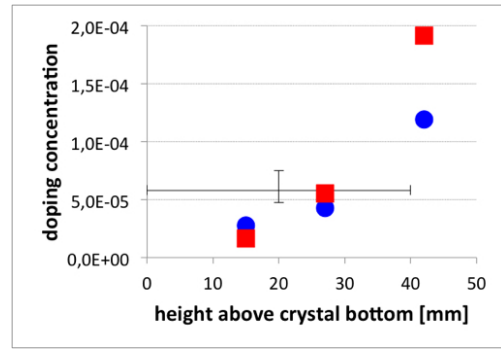


Figure 3.17: V037

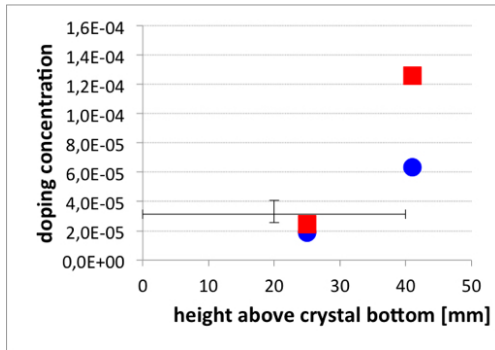


Figure 3.18: V038

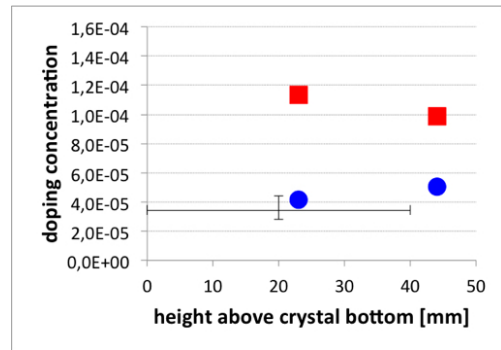


Figure 3.19: V039

$^{232}\text{Th}$  concentration in lightly-doped  $\text{CaF}_2$  crystals measured by neutron activation analysis. The doping concentration ( $N_{\text{Th}}/N_{\text{Ca}}$ ) was determined separately for the bulk (red) and the crystal's surface (blue). The black vertical error bar marks the expected range of the doping concentration.

In most cases, the  $^{232}\text{Th}$  concentration in the bulk material is higher than in the crystal's surface. Only the seed-containing parts of the crystal show a reversed concentration gradient. This can be explained by melt (which contains the dopant) flowing down into the gap between the seed and the crucible (compare fig. 2.13), where it crystallizes faster than the rest of the crystal due to the lower temperature near the bottom of the crucible. The bulk of the crystal's bottom part contains mainly the material of the undoped  $\text{CaF}_2$  seed (in most cases only partially molten) and therefore shows a lower doping concentration.

Crystal V029 was one of the first attempts of growing  $^{232}\text{Th}:\text{CaF}_2$ . It shows an intransparent part in the upper half (fig. 3.20), probably due to imperfect seeding because the dopant altered the melting point of  $\text{CaF}_2$ . Unmolten  $\text{CaF}_2$  on top of the seed can form such an opaque crystal part. Samples for the NAA were taken from its center, as well as from the transparent parts just above and below it. The doping concentration spiked in the bulk of the intransparent part but remained around the estimated mean value at the surface (fig. 3.14).

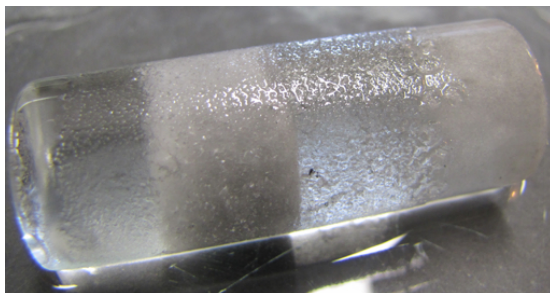


Figure 3.20: Intransparent part in crystal V029

The  $\text{CaF}_2$  powder on top of the seed (right part of the crystal) was probably not completely molten and formed an opaque layer.

For the other lightly-doped crystals, the highest doping concentration was found in the crystal's top end cap, which crystallizes last. This supports the hypothesis that the thorium concentration is higher in the melt than in the crystal during growth. Similarly, the lead from the scavenger process (section 2.3.4) tends to accumulate on crystal surfaces, mostly at the crystal's top part, which crystallizes last (fig. 3.9).

In the  $^{232}\text{Th}$ -doped crystals V034, V036 and V037, there is only a small difference between bulk and surface doping concentration. Only the top end piece deviates from that trend, furthermore showing a doping concentration which is a multiple of the one in the other crystal parts. In V036, rather high doping concentrations compared to the calculated mean value (black error bars in the figures) were measured. Its  $^{232}\text{Th}$  concentration is comparable to that of V037 although only a 1/10 of the dopant amount was added. It indicates that there has been a transfer of  $^{232}\text{Th}$  from previous growth processes. The most likely case is that some material remained in the crucible.

Two crystals (V040 and V041) were grown with a much higher dopant amount of 0.8 g  $\text{ThF}_4$  and are therefore referred to as **highly-doped**.

Increasing the doping concentration to values close to one per cent ( $N_{\text{Th}}/N_{\text{Ca}}$ ) was originally intended for X-ray diffraction analysis. It was checked if any information could be gained about the distortion of the  $\text{CaF}_2$  crystal lattice due to the thorium doping, ideally revealing the configuration of neighbouring atoms at the doping site. Unfortunately, no other results than confirming a locally mono-crystalline  $\text{CaF}_2$  lattice were obtained. However, the crystals showed some structural weaknesses during machining and were more likely to crack compared to undoped or lightly-doped  $\text{CaF}_2$ .

For the highly-doped crystals, accumulation of the dopant in the melt, towards the end of the growth process, could not be observed. The crystal V040 was cut parallel to the cylindrical axis, and a thin, rectangular piece that contains the entire concentration profile was cut out of the crystal's bulk (fig. 3.21). The

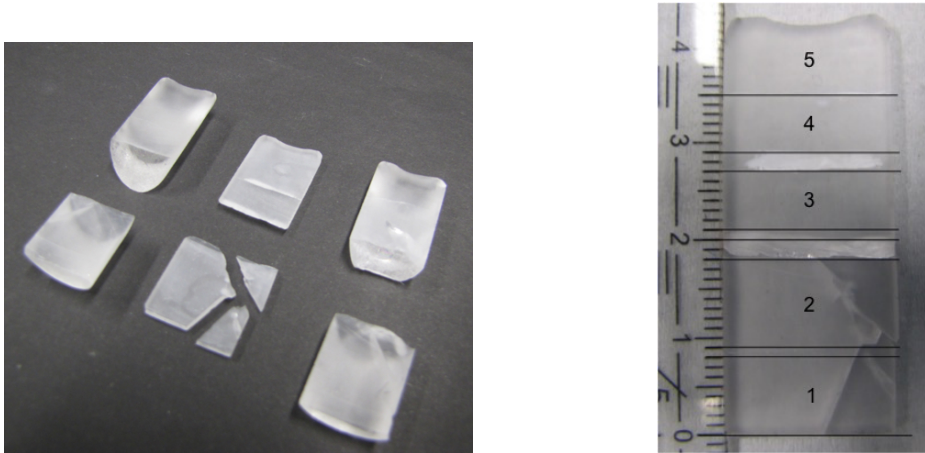


Figure 3.21: Sample preparation for NAA of the highly-doped  $^{232}\text{Th}:\text{CaF}_2$  crystal. The concentration profile was measured in the middle part cut out from crystal V040 (left image). This middle part was divided into 5 sample pieces (numbered in the right image). The  $^{232}\text{Th}$  concentration in the bulk and the surface was determined separately for each sample piece by NAA.

highest doping concentration is found in the bottom part and the middle of the crystal, just above the molten seed (fig. 3.23). The doping concentration in the bulk drops to 2/3 of the maximum in the crystal's top, whereas it shows a slight increase in the upper part of the crystal's surface.

The two investigated crystal parts of V041 (fig. 3.22) show a doping concentration comparable to V040. The doping concentration in both crystals does not exceed the calculated mean which could be an indication that there is a limit of how much thorium  $\text{CaF}_2$  accepts. This was not investigated further since the typically desired doping concentrations are much lower and the X-ray diffraction analysis, for which these crystals were grown, did not yield the desired results.

### VGF-grown $^{229}\text{Th}:\text{CaF}_2$

Three  $\text{CaF}_2$  crystals doped with a mixture of  $^{232}\text{Th}$  and  $^{229}\text{Th}$  were grown by means of the vertical gradient freeze method (sample preparation described in section 3.1.2). The expected doping concentrations were calculated from the masses of the raw materials and are listed in table 3.5.

The atom number of  $^{229}\text{Th}$  in the crystal is typically three orders of magnitude lower than for  $^{232}\text{Th}$ . However, the half-life of  $^{229}\text{Th}$  (7932(28) a) is considerably shorter compared to  $^{232}\text{Th}$  ( $1.40 \cdot 10^{10}$  a). The daughter nuclei of  $^{229}\text{Th}$  ( $^{225}\text{Ra}$ ) has gamma lines with sufficient intensities (fig. 3.12), which make gamma spectroscopy for  $^{229}\text{Th}$ -doped crystals possible. For the lightly-doped crystals V038

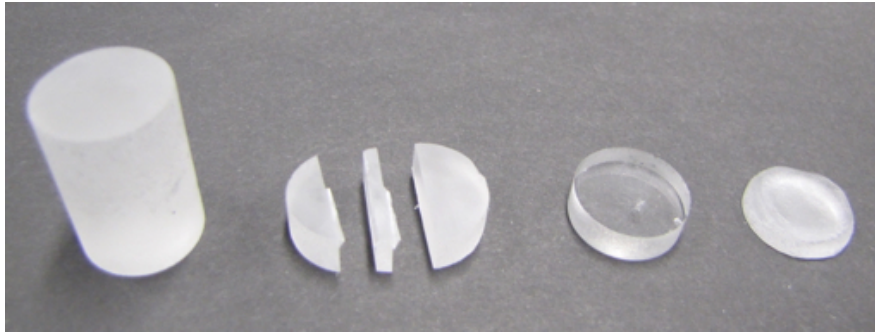


Figure 3.22: Highly-doped  $^{232}\text{Th}:\text{CaF}_2$  crystal V041 cut for NAA. The crystal was cut into 4 cylindrical pieces, whereas a sample for NAA was cut out of the middle of one of them. The top end cap (right) of the crystal was also used for determining the doping concentration by NAA.

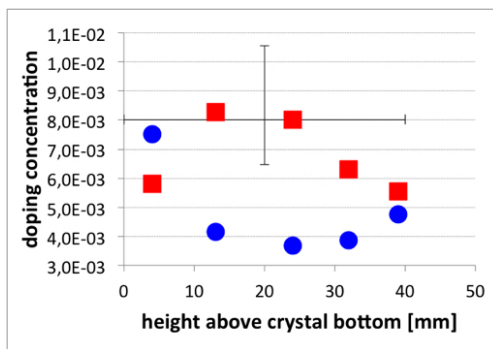


Figure 3.23: V040

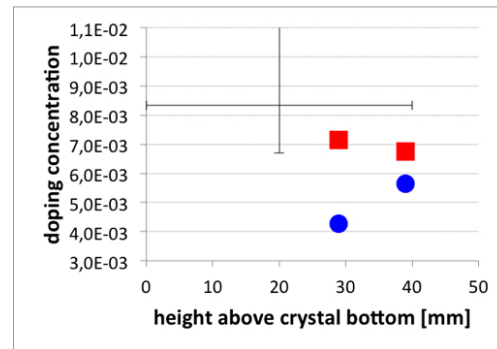


Figure 3.24: V041

$^{232}\text{Th}$  concentration in highly-doped  $\text{CaF}_2$  crystals measured by neutron activation analysis. The doping concentration ( $N_{\text{Th}}/N_{\text{Ca}}$ ) was determined separately for the bulk (red) and the crystal's surface (blue). The black vertical error bar marks the expected range of the doping concentration.

and V039, count rates of a few  $\text{s}^{-1}$  require a measurement time of a few hours for the remaining measurement uncertainty to decrease to the percent level.

Crystal V038 was cut into three pieces, whereas (V038bot) is the bottom part containing the seed, and V038top is the upper end cap. The upper part of the middle piece (V038mid) of the crystal was cut and polished to obtain a 5.1 mm thick disk (V038:4, fig. 4.5b). Table 3.6 lists the masses and the height of the cylindrical crystal parts, as well as the results of the gamma spectroscopy (section 3.5.1). All crystal pieces were oriented so that their bottom parts were closer to the detector during the measurement. The measured activity was normalized to the mass of the sample ( $A_{\text{meas}}^m$ ). The average of all four samples can be found in the last column of the table.

Seeding was incomplete during growth of V038, resulting in a layer of unsuffi-

Table 3.5: Expected  $^{229}\text{Th}$  concentration in VGF-grown  $\text{CaF}_2$ 

The lower value corresponds to the case in which the seed is molten completely, for the upper value it was assumed that the seed was not molten at all. The amount of  $^{232}\text{Th}$  in V039 could only be determined with an uncertainty of  $\sim 5\%$  that arose during the chemical sample preparation<sup>11</sup>.

crystal	$N_{232}/N_{229}$	expected Th-229 doping concentration		
		[ng/g]	$[\text{cm}^{-3}]$	$N_{Th}/N_{Ca}$
V038	4620	17-28	$(1.4 - 2.3) \cdot 10^{14}$	$(6 - 10) \cdot 10^{-9}$
V039	4200(200)	19-30	$(1.6 - 2.5) \cdot 10^{14}$	$(6 - 10) \cdot 10^{-9}$
V057	164	770-1220	$(6.4 - 10.1) \cdot 10^{15}$	$(2.6 - 4.1) \cdot 10^{-7}$

ciently molten  $\text{CaF}_2$  above the seed (fig. 2.10c), both contained in V038bot. The high doping concentration measured in the bottom part can be attributed to the intransparent layer (and eventually to material flowing down into the gap between seed and crucible), since only very little of the seed was molten. According to the coarse gamma spectroscopy analysis, the transparent middle part V038mid contains a factor five less dopants per volume than V038bot or the upper end cap (V038top). In  $^{232}\text{Th}:\text{CaF}_2$ , it was already shown by NAA that the doping concentration increases in the upper (i.e. later grown) parts of the crystal, which is also suggested by the outcome of this measurement.

 Table 3.6:  $^{229}\text{Th}$  concentration of V038 determined by gamma spectroscopy

crystal part	V038bot	V038mid	V038top	V038:4	average
height [mm]	25.3	15.0	1.5	5.1	
mass [g]	18.16	11.15	0.72	3,73	
$A_{meas}^m$ [Bq/g]	500	100	500	300	300(200)
$n_m(^{229}\text{Th})$ [ng/g]	70	20	70	30	50 (20)
$n_V(^{229}\text{Th})$ [ $\text{cm}^{-3}$ ]	$5 \cdot 10^{14}$	$1 \cdot 10^{14}$	$6 \cdot 10^{14}$	$3 \cdot 10^{14}$	$4(2) \cdot 10^{14}$
$N_{Th-229}/N_{Ca}$	$2 \cdot 10^{-8}$	$5 \cdot 10^{-9}$	$2 \cdot 10^{-8}$	$1 \cdot 10^{-8}$	$1.6(7) \cdot 10^{-8}$

The obtained results from gamma spectroscopy measurements of crystal V039 are given in the tables 3.7 and 3.8. A gamma spectrum of the crucible filled with the raw material was recorded before as well as after crystal growth (before cg, after cg). The crystal was then taken out of the crucible and measured again, once facing upwards ( $\uparrow$ ), i.e. with the bottom part closer to the detector, and once facing downwards ( $\downarrow$ ). No signal could be obtained for the empty crucible.

The  $^{229}\text{Th}$  atoms were redistributed in the crucible when the  $\text{CaF}_2$  powder was molten. Gamma spectroscopy therefore only allowed a coarse estimation of the doping efficiency. The three results<sup>12</sup> for the doping concentrations of the grown crystal were averaged. Comparison with the activity of the raw material (crucible

<sup>12</sup>crucible after growth, crystal  $\uparrow$  and  $\downarrow$

before crystal growth) shows the concentration of the contained  $^{229}\text{Th}$  is of the same order of magnitude (table 3.7).

Table 3.7:  $^{229}\text{Th}$  concentration of V039 determined by gamma spectroscopy

	crucible		crystal		average
	before cg	after cg	↑	↓	a.g. ↑ ↓
$A_{meas}^m$ [Bq/g]	60	30	40	150	80(50)
$n_m(^{229}\text{Th})$ [ng/g]	9	5	6	21	10 (7)
$n_V(^{229}\text{Th})$ [ $\text{cm}^{-3}$ ]	$7 \cdot 10^{13}$	$4 \cdot 10^{13}$	$5 \cdot 10^{13}$	$17 \cdot 10^{13}$	$9(6) \cdot 10^{13}$
$N_{Th-229}/N_{Ca}$	$3 \cdot 10^{-9}$	$2 \cdot 10^{-9}$	$2 \cdot 10^{-9}$	$7 \cdot 10^{-9}$	$4(2) \cdot 10^{-9}$

Crystal V039 was cut into three parts (table 3.8), whereas the bottom and the middle part have roughly the same height. Like in V038bot, the bottom part of the crystal (V039bot) contains a thin, intransparent layer of  $\text{CaF}_2$  powder which was not sufficiently molten. V039bot and V039mid were put on the gamma detector facing upwards and downwards. For both samples, the measured activity was lower in the lower part of the sample, i.e. the upwards-facing measurement yielded a lower activity (first value in the table) compared to downwards-facing measurement (second value). The doping concentration of the crystal's upper end cap (V039top) was only measured once due to the small sample thickness. The determined doping concentration was a factor of 5 – 10 higher than in the other parts of the crystal. Apart from the upper end cap of the crystal, the thorium activity is of the same order of magnitude (or even higher) as in the crucible before growth.

Table 3.8:  $^{229}\text{Th}$  concentration of V039 determined by gamma spectroscopy

crystal part	V039bot	V039mid	V039top
thickness [mm]	23.8	19.7	1.3
mass [g]	16.77	14.95	0.76
$A_{meas}^m$ [Bq/g]	45-170	190-250	1150
$n_m(^{229}\text{Th})$ [ng/g]	5-20	25-35	160
$n_V(^{229}\text{Th})$ [ $\text{cm}^{-3}$ ]	$(5 - 20) \cdot 10^{13}$	$(20 - 30) \cdot 10^{13}$	$1.3 \cdot 10^{15}$
$N_{Th-229}/N_{Ca}$	$(2 - 8) \cdot 10^{-9}$	$(9 - 10) \cdot 10^{-9}$	$5 \cdot 10^{-8}$

The crystals V038 and V039 were both doped with a mixture of  $^{232}\text{Th}$  and  $^{229}\text{Th}$ , but only  $^{232}\text{Th}$  can be detected in NAA due to its higher amount in the crystal. The thorium isotopes are chemically identical, and it is therefore safe to assume that their distribution in the crystal is the same. Knowing the ratio between  $^{229}\text{Th}$  and  $^{232}\text{Th}$  in the raw material (table 3.5), allows the extrapolation of the  $^{229}\text{Th}$  concentration from the NAA results of  $^{232}\text{Th}$  (section 3.5.2). These extrapolated  $^{229}\text{Th}$  concentrations are plotted in figs. 3.25 and 3.26.



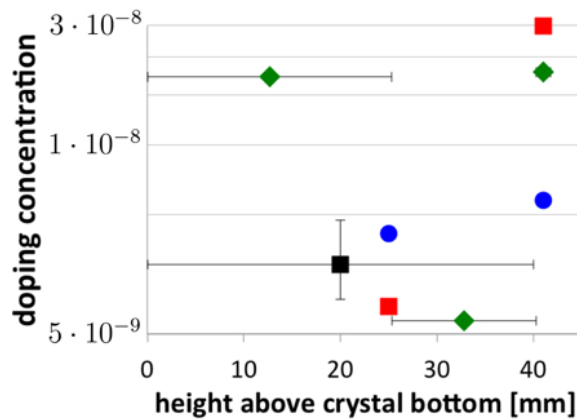


Figure 3.25:  $^{229}\text{Th}$  concentration in V038

given as  $N_{\text{Th-229}}/N_{\text{Ca}}$ . The values for the bulk (red) and the surface (blue) of the crystal were extrapolated from the  $^{232}\text{Th}$  concentration determined by NAA. A coarse estimation for the  $^{229}\text{Th}$  concentration of the different crystal parts (indicated by the horizontal error bars) is based on gamma spectroscopy measurements (green). The black square gives the expected doping concentration, whereas the vertical error bars show the range between a fully molten and a completely intact seed.

Only the intransparent layer above the seed and the crystal's upper end cap of the crystals V038 and V039 were used for the destructive NAA. A new crucible was used for the growth of V038 to avoid cross-transfer of doping material from former growth processes. The doping concentration in the intransparent layer of V038 is within the expected range in the bulk and the surface. Only the crystal's upper end piece shows a much higher concentration, like in V034, V036 and V037.

The bulk's doping concentration in the intransparent part of V039, however, is a factor of three higher than the expected mean value of the crystal, the concentration in the upper end cap more than a factor of two. The gamma spectroscopy measurements (table 3.8) indicate that the doping concentration increases from the bottom to the top of the crystal, and that there is also a significant number of  $^{229}\text{Th}$  atoms in the transparent part (V038mid) between the samples used for NAA. The significantly higher  $^{229}\text{Th}$  concentration of V039 might be explained by cross-transfer of doping material from the previously grown V038, for which the same crucible was used.

After V039, the highly-doped  $^{232}\text{Th}:\text{CaF}_2$  crystal was grown. Although a new crucible was used, the radioluminescence spectrum shows a feature attributed to a  $^{229}\text{Th}$  contamination of 0.8(1) ppm of the  $^{232}\text{Th}$  concentration, which would be of the same order of magnitude as the expected  $^{229}\text{Th}$  concentration in V038 and V039. A further indication of thorium cross-transfer between growth processes, that gives a much lower fraction of dopant carry-over, though, is discussed later.

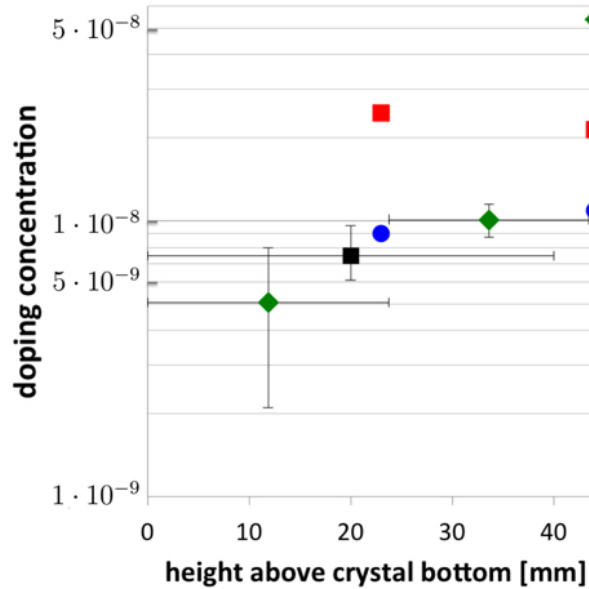


Figure 3.26:  $^{229}\text{Th}$  concentration in V039 given as  $N_{\text{Th-229}}/N_{\text{Ca}}$ . The values for the bulk (red) and the surface (blue) of the crystal were extrapolated from the  $^{232}\text{Th}$  concentration determined by NAA. The error bars due to the 5% uncertainty of the  $^{229}\text{Th}$  concentration in the raw material are within the size of the dots.

A coarse estimation for the  $^{229}\text{Th}$  concentration of the different crystal parts (indicated by the horizontal error bars) is based on gamma spectroscopy measurements (green). The grey triangle gives the mean value of the different gamma spectroscopy measurements of the entire crystal. The black square gives the expected doping concentration, whereas the vertical error bars show the range between a fully molten and a completely intact seed.

The crystal with the highest number of incorporated  $^{229}\text{Th}$  atoms so far is V057 (fig. 3.27). The expected doping concentration (table 3.9) is a factor of 25 – 70 higher than for the other two  $^{229}\text{Th}:\text{CaF}_2$  crystals (table 3.5), depending on how much of the seed crystal was molten. A coarse estimation of the  $^{229}\text{Th}$  concentration was determined by measuring the entire crystal by means of gamma spectroscopy (table 3.9).

Table 3.9:  $^{229}\text{Th}$  concentration of V057 determined by gamma spectroscopy. The crystal was measured once in the same direction as during growth ( $\uparrow$ ) and once upside down ( $\downarrow$ ). The gamma lines at 194 keV and 211 keV delivered different results, and are therefore listed separately.

	expected $^{229}\text{Th}$ conc.	$\uparrow$		$\downarrow$	
		194 keV	211 keV	194 keV	211 keV
$A_{meas}^m$ [Bq/g]	5700	2600	2900	2900	3300
$n_m(^{229}\text{Th})$ [ng/g]	770-1220	460	350	360	400
$n_V(^{229}\text{Th})$ [ $\text{cm}^{-3}$ ]	$(6.4 - 10.1) \cdot 10^{15}$	$4 \cdot 10^{15}$	$3 \cdot 10^{15}$	$3 \cdot 10^{15}$	$3 \cdot 10^{15}$
$N_{Th-229}/N_{Ca}$	$(2.6 - 4.1) \cdot 10^{-7}$	$2 \cdot 10^{-7}$	$1 \cdot 10^{-7}$	$1 \cdot 10^{-7}$	$1 \cdot 10^{-7}$

A 4.5 mm thick slice was cut from the crystal just beneath the upper end cap. The results of the gamma spectroscopy measurements of this sample can be found in table 3.10. From this slice, a cuboid was cut and polished to obtain a sample (fig. 3.28) for synchrotron measurements at the Metrology Light Source (MLS), Berlin [92].

After the highly-doped  $^{229}\text{Th}:\text{CaF}_2$  crystal V057, a  $^{232}\text{U}:\text{CaF}_2$  (V058) was grown. The results of gamma spectroscopy measurements suggest that there has been some carry-over of the dopant although a different crucible was used. However, the  $^{229}\text{Th}$  concentration in V058 is a factor of 5000(1000) lower than in the previous crystal.

Table 3.10:  $^{229}\text{Th}$  concentration determined by gamma spectroscopy in a 4.5 mm thick slice cut from the upper part of V057

The expected doping concentration is an average for the entire crystal, taken from table 3.5. The sample was measured once in the same direction as during growth ( $\uparrow$ ) and once upside down ( $\downarrow$ ). The gamma lines at 194 keV and 211 keV delivered different results, and are therefore listed separately.

	expected $^{229}\text{Th}$ conc.	sample $\uparrow$		sample $\downarrow$	
		194 keV	211 keV	194 keV	211 keV
$A_{meas}^m$ [Bq/g]	5700	9600	7900	6000	6600
$n_m(^{229}\text{Th})$ [ng/g]	770-1220	1300	1100	800	900
$n_V(^{229}\text{Th})$ [ $\text{cm}^{-3}$ ]	$(6.4 - 10.1) \cdot 10^{15}$	$11 \cdot 10^{15}$	$9 \cdot 10^{15}$	$7 \cdot 10^{15}$	$8 \cdot 10^{15}$
$N_{Th-229}/N_{Ca}$	$(2.6 - 4.1) \cdot 10^{-7}$	$4 \cdot 10^{-7}$	$4 \cdot 10^{-7}$	$3 \cdot 10^{-7}$	$3 \cdot 10^{-7}$

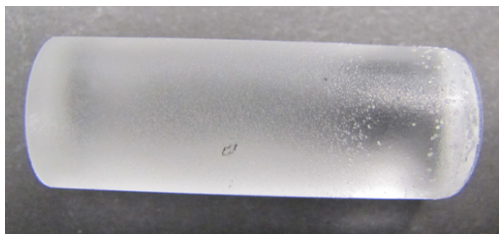


Figure 3.27: Highly-doped  $^{229}\text{Th}:\text{CaF}_2$  crystal V057

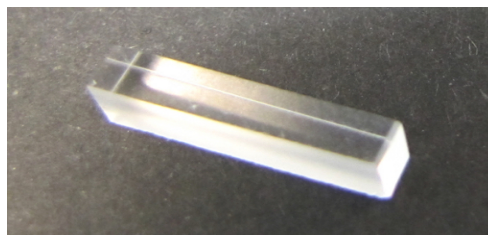


Figure 3.28: Polished sample of V057  
Dimensions:  $3.5 \times 2.5 \times 13 \text{ mm}^3$ .



Figure 3.29: Zr-doped  $\text{CaF}_2$  crystal

The crystal V027 was sliced into 9 pieces, three of which (number 3, 5 and 7; counting from the left) were used for determining the doping concentration by NAA.

### VGF-grown $\text{Zr}:\text{CaF}_2$

One crystal was doped with zirconium to study the effects of this byproduct in the  $^{229}\text{Th}$  sample. 57.8 mg of  $\text{ZrF}_4$  were added to 33.3 g of  $\text{CaF}_2$  before growth<sup>13</sup>. The resulting crystal V027 (fig. 3.29) showed an intransparent part (probably due to imperfect seeding) in the top half. A slice was cut out from the center of that part, as well as from the transparent parts above and below it. Bulk and surface were investigated separately by means of NAA like for the  $^{232}\text{Th}$ -doped crystals (section 3.5.2). Both, the 756 keV gamma peak of  $^{95}\text{Zr}$  and the 1147 keV gamma peak of  $^{97}\text{Zr}$  were investigated separately, but only a detection limit on the order of a few milligram could be determined. The samples were then sealed in glass vials and irradiated for 40 hours<sup>14</sup> in the TRIGA Mark II research reactor at the ATI. No zirconium could be found in the crystal. The detection limit was lowered to  $2 - 3 \mu\text{g/g}$  in these measurements. It can therefore be concluded that zirconium poses no complications in the growth of  $^{229}\text{Th}:\text{CaF}_2$  crystals because the doping efficiency of zirconium in  $\text{CaF}_2$  is too low.

<sup>13</sup>19.3 g  $\text{CaF}_2$  powder and 14 g  $\text{CaF}_2$  seed

<sup>14</sup>compared to previous irradiation times of a few hours

## 4 Optical crystal characterization

For exciting the nuclear transition of  $^{229}\text{Th}$  doped into  $\text{CaF}_2$  and detecting the emitted photons, the transparency of the crystal in the VUV region is of utmost importance. Optical characterization allows to determine how much of the nuclear spectroscopy signal (as well as the excitation light) is absorbed by the crystal. It will be shown that thorium-doped  $\text{CaF}_2$  shows a similar UV transmission as undoped  $\text{CaF}_2$  crystals grown by the same method (section 4.1).

Luminescence photons are the crystal's response to illumination with UV light (photoluminescence, section 4.2.2) or to radioactive decay of dopants/impurities in the crystal (radioluminescence, section 4.2.3). The luminescence spectrum as well as the temporal characteristic and the temperature-dependence of the photon emission are studied to allow a distinction between this kind of background noise and the actual signal, i.e. photoemission by deexcitation of the  $^{229}\text{Th}$  isomer.

### 4.1 VUV Transmission

The currently accepted value for the isomer energy of  $^{229}\text{Th}$  is  $7.8 \pm 0.5 \text{ eV}$  [4, 5], which corresponds to a wavelength region of 150 – 170 nm in the vacuum ultraviolet (VUV) part of the electromagnetic spectrum. When implanting  $^{229}\text{Th}$  into an ionic crystal, it must remain sufficiently transparent in that wavelength region so that (1) excitation light can reach the nucleus and (2) photons emitted during deexcitation of the isomeric state can reach a detector.

In a crystal, the possible energies of the electrons form bands due to the periodicity of the atoms or molecules in the lattice. The energy range between the highest occupied states<sup>1</sup> (valence band) and the unoccupied states (conduction band) is the band gap. The electronic band structure determines if a crystal is transparent at a certain wavelength since photons are only transmitted if there is no electronic state available that can be excited by the photon energy. The band gap sets a limit for the maximum energy a photon can have to still be transmitted through the crystal (cut-off energy). If electronic states are formed within the energy range of the band gap (forbidden zone)<sup>2</sup>, e.g. by defects or impurities, the maximum frequency that is still transmitted by the crystal is reduced.

---

<sup>1</sup>at zero temperature

<sup>2</sup>Per definition, the band gap is the energy range without electronic states. New states can therefore not be formed **within** the band gap. If new electronic levels occur, the energy range of the band gap is redefined.

In the VUV spectral range, only a few wide-band-gap materials, e.g. fused silica and the alkaline earth fluorides, offer an acceptable transmittance. Calcium fluoride is one of the most commonly used materials due to its favorable properties for lithography. Optical-grade  $\text{CaF}_2$  crystals have a cut-off wavelength<sup>3</sup> between 120 – 130 nm and the transmittance for sample thicknesses of a few millimeter can reach values greater than 60% above 150 nm [93–95].

Light passing through the crystal loses intensity due to absorption (section 4.1.1) and scattering (section 4.1.2). At each crystal surface, including inner surfaces like grain boundaries, inclusions, segregations etc, part of the light is reflected (section 4.1.3). The VUV transmission therefore depends on the quality of the grown crystal as well as the surface preparation.

For studying how the crystal properties are changed due to doping  $\text{CaF}_2$  with thorium, one can substitute the rare, artificial radioisotope  $^{229}\text{Th}$  (half-life of  $T_{1/2} = (7932 \pm 28) \text{ a}$  [79]) with the chemically identical and readily available isotope  $^{232}\text{Th}$  (half-life of  $T_{1/2} = 1.40 \cdot 10^{10} \text{ a}$  [79]).

A list of physical quantities for thorough optical characterization of  $\text{CaF}_2$  crystals can be found in [40].

#### 4.1.1 Absorption

Absorption of electromagnetic radiation is a process during which matter transforms energy of photons into internal energy of the absorber. The intensity of a beam of light propagating through matter is reduced because photons are absorbed by exciting electronic states in atoms, molecules etc. The excitation energy can be re-emitted as a photon (photoluminescence, section 4.2.2) or transformed, e.g. into thermal energy, phonons. As a coarse distinction, absorption can be seen as a process that removes energy from the electromagnetic field (at least for some time, in the case of photoluminescence), whereas scattering section 4.1.2) redirects light with only minimal losses.

The intensity  $I$  of light in matter typically decays exponentially with the path length  $x$ , an attenuation which is described by the Beer-Lambert law:

$$I(x) = I_0 \exp(-\alpha(\lambda) \cdot x). \quad (4.1)$$

The absorption coefficient  $\alpha$  depends on the absorbing material and the wavelength  $\lambda$  but in most cases not on the intensity of the light. However, if the intensity is high enough, like in a pulsed laser, two photons can be absorbed at once. If their combined energy is greater than the band gap and smaller than the ionization threshold, an electronic state in the conduction band can be excited.

---

<sup>3</sup>The crystals are intransparent beneath the cut-off wavelength.

Absorption involving two photons is considered by the effective absorption coefficient  $\beta_{eff}$ . It does not only include pure two-photon absorption ( $\beta$ ) but also two-step absorption ( $\beta_{2-step}$ ): the first photon excites a state in the forbidden zone induced by external atoms, defects or colour centers, a second photon drives a transition from this state to a state in the conduction band. Since  $\beta \ll \beta_{2-step}$ ,  $\beta_{eff}$  is to a large extent attributed to the influence of impurities or defects [96]. The differential form of the Beer-Lambert law (eq. 4.1) then becomes:

$$\frac{dI(x)}{dx} = -\alpha(\lambda)I - \beta_{eff}(\lambda)I^2. \quad (4.2)$$

Solving the differential equation and inserting the boundary conditions  $I(x = 0) = I_0$  yields the following term for the bulk absorption of the crystal:

$$I(x) = \frac{I_0}{\frac{\beta_{eff}(\lambda)}{\alpha(\lambda)} I_0 [\exp(\alpha(\lambda)x) - 1] + 1}. \quad (4.3)$$

The total absorptance  $A$  in a crystal, i.e. the fraction of the incident light intensity that is absorbed, can be modelled by taking three terms into account [97]:

$$A(\lambda, d, H, \Delta t, \sigma_{rms}) = \left| \frac{dI}{I} \right| = \underbrace{A_{surf}(\lambda, \sigma_{rms})}_{(1)} + \left( \underbrace{\alpha(\lambda)}_{(2)} + \underbrace{\beta_{eff}(\lambda, \Delta t) \frac{H}{\tau}}_{(3)} \right) d. \quad (4.4)$$

The first term, the surface absorptance  $A_{surf}$ , depends on the irradiation wavelength  $\lambda$  and the surface roughness  $\sigma_{rms}$ . The second term with the wavelength-dependent single-photon absorption coefficient  $\alpha$  describes the linear absorption in the bulk of the crystal. Two-photon absorption is covered by the third term, where  $\beta_{eff}$  is the the effective two-photon absorption coefficient (more details below) that also depends on the time interval  $\Delta t$  between laser pulses.  $H$  and  $\tau$  are the fluence and the pulse length of the laser and  $d$  is the sample thickness.

### Oxygen-induced absorption

The optical quality of  $\text{CaF}_2$  crystals is drastically decreased by oxygen incorporation. The UV transmission below 200 nm is reduced from  $> 80\%$  to  $< 40\%$  for oxygen concentrations of about 10 ppm. At concentrations around 100 ppm the crystals become practically opaque in the UV region. Measurements reveal an absorption peak between 185 and 230 nm, with a maximum around 197 nm. Generally, the absorption coefficient increases linearly with oxygen concentration.

The UV transparency is already reduced significantly at an oxygen level of a few 10 ppm and the crystal becomes opaque below 200 nm at oxygen concentrations of about 100 ppm [56, 69].

Water vapor but also molecular oxygen, are to a certain extent permanently present during crystal growth, either due to inevitable leaks or contamination of the raw material and the vacuum chamber. Especially the thermal insulation made of graphite can hold some air and water between its fibers. Oxygen-containing impurities penetrate the crucible and are ionized at the hot crucible walls. The resulting  $\text{OH}^-$  and  $\text{O}^{2-}$  ions dissolve into the melt and are embedded into the  $\text{CaF}_2$  lattice in the place of  $\text{F}^-$ -vacancies, where they form charge-compensating ions [40]. The resulting optically active centers cause absorption bands over a wide wavelength range from UV to IR [61].

At higher concentrations and temperatures above 850 K, the oxygen-containing ions react with Ca to CaO at high rates. The reaction product CaO precipitates as a separate phase during crystallization and forms a great number of micro-dispersed particles causing intensive light scattering (section 4.1.2). A drop in optical transmission, leading in the worst case to opacity, significant stoichiometric inhomogeneity, anisotropy, residual stresses, strong luminescence and reduced radiation hardness, can be the consequence [40].

In order to minimize oxygen-contamination,  $\text{CaF}_2$  crystals have to be grown in high-vacuum or in an inlet flow of purified argon<sup>4</sup>. Growth in a reactive HF atmosphere is reported to cause an absorption band in the UV [40] (and references therein).

The oxygen diffusion into the crucible should be minimized (section 2.2.5) as well as the oxygen content of the raw material.  $\text{CaF}_2$  powder has a high specific surface area which favors adsorption of moisture. Its removal from the starting material is difficult due to the high binding energy between the water molecules and the  $\text{CaF}_2$  powder. Oxygen can be removed chemically by adding a metal scavenger to the raw material. Reactions of the scavenger with the water vapor and the CaO produce volatile metal oxides or gases like HF and  $\text{CO}_2$ , which can easily be removed under high-vacuum and high-temperature conditions.

Although  $\text{PbF}_2$  is the most commonly used scavenger for  $\text{CaF}_2$  [98–100], other metal fluorides like  $\text{ZnF}_2$ ,  $\text{CdF}_2$  or  $\text{MnF}_2$  are used for removing oxygen from  $\text{CaF}_2$  [100, 101]. Fluorine-containing reactive gases like HF,  $\text{NF}_3$ ,  $\text{SF}_6$  and  $\text{CF}_4$  can also be used for scavenger processes [101–103]. An analysis of how the UV transmission depends on the admixture of different concentrations of  $\text{PbF}_2$  or  $\text{ZnF}_2$  can be found in [40].

---

<sup>4</sup>level of contaminants: < 1 ppm by volume [40]



### 4.1.2 Scattering

Light can be forced to deviate from a straight trajectory by non-uniformities in a crystal or on its surface, which causes a weakening of the light intensity in the beam's direction. The list of possible scattering centers in crystals is long, including incorporated particles or bubbles, defects, grain boundaries, inclusions, material segregation at free or internal surfaces, crystallites in polycrystalline solids, plastic deformations etc. Irregularities on the crystal due to contamination or bad polishing can also be the reason for scattering losses. Diffuse reflections, where an incident ray is reflected in many different directions, are also a form of scattering since the angle of the reflected beam differs from the predictions of the law of reflection.

This underlines the importance of controlling the crystal growth process so that single crystals (no grain boundaries) with a low number of inhomogeneities are produced.

### 4.1.3 Reflection

UV light that passes through a  $\text{CaF}_2$  crystal experiences reflection losses at both surfaces. If the surface roughness is much smaller than the wavelength of the light, the reflection is specular (instead of diffuse). For normal incidence ( $\Theta_i = 0$ ), the simplified Fresnel equation can be used to calculate the reflectance  $R$  for one surface:

$$R(\Theta_i = 0) = \left( \frac{n_{amb} - n_{\text{CaF}_2}}{n_{amb} + n_{\text{CaF}_2}} \right)^2. \quad (4.5)$$

$n_{amb}$  is the refractive index of the ambient gas in the wavelength region 150 – 170 nm (1.0003 for nitrogen, 1 for vacuum) and  $n_{\text{CaF}_2}$  is the refractive index of calcium fluoride (between 1.58 at 150 nm and 1.53 at 170 nm [104]). Even for perfectly parallel crystal end faces and for perfect alignment of the crystal with respect to the beam of light ( $\Theta_i = 0$ ), the reflection loss per surface is between 4.4% (at 170 nm) and 5.0% (at 150 nm). This results in a total reflection loss for both surfaces<sup>5</sup>  $2R/(1 + R)$  of (8.4 – 9.6)%. Antireflection coatings can decrease the reflectivity per surface to  $R < 0.8\%$  at 157 nm [105] but were not used for our crystal samples.

<sup>5</sup>taking into account multiple reflections between the crystal surfaces without interference

#### 4.1.4 Transmission of (doped) CaF<sub>2</sub> crystals between 120-190 nm

This section describes transmittance measurements with a broad-band excitation source emitting a continuous spectrum above 120 nm (fig. 4.1b).

##### Spectrometer setup

A spectrometer (McPherson model 234/302; see fig. 4.1a) was used to measure the VUV transmittance of the (doped) CaF<sub>2</sub> crystals. In these measurements, the intensity of the light transmitted through the crystal ( $I_{crystal}$ ) was compared to the unattenuated light intensity  $I_{ref}$  (without the crystal in the beam path) in order to obtain the transmittance  $T$ :

$$T(\lambda, d) = \frac{I_{crystal}(\lambda, d)}{I_{ref}(\lambda)} \quad (4.6)$$

where  $\lambda$  is the wavelength of the incident light and  $d$  stands for the sample thickness.

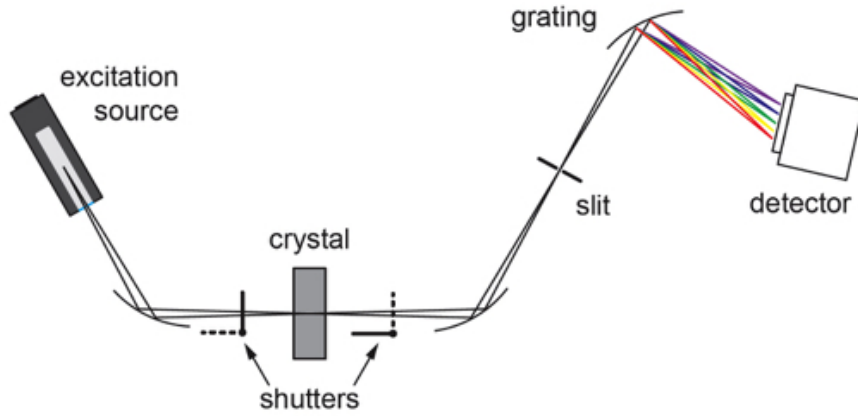
The deuterium lamp is a gas-discharge light source which emits a continuous spectrum between 120 nm and 160 nm (fig. 4.1b) created by light emission of excited states in molecular deuterium (D<sub>2</sub>). The characteristic peaks of the spectrum can be used for wavelength calibration of the spectrometer. A manual actuator allowed to place different samples in the central region where the light intensity on the crystal was a few W/cm<sup>2</sup> with a spot size of 3 mm. The crystal was imaged onto a slit with a typical width of 600  $\mu$ m, and the slit in turn was imaged onto the sensor of a CCD<sup>6</sup> camera by a concave holographic diffraction grating. The grating directs the different wavelengths of the incident light onto different positions (vertical stripes) of the CCD, thereby imaging the spectrum. For the transmittance measurements, gratings with a groove density between 300 and 1200 g/mm were used, most measurements were carried out with a 1200 g/mm grating. An Andor Newton camera (940 model) with a pixel size of 13.5  $\mu$ m was used. Its CCD chip was cooled to temperatures below  $-80^\circ\text{C}$  for the measurements. The pixels of the CCD were typically binned vertically, i.e. the signals of pixels in the same column (same wavelength) were electronically added together in order to improve the signal-to-noise ratio<sup>7</sup>.

Since molecular oxygen absorbs light at wavelengths below 180 nm, all measurements have to be carried out in an oxygen-depleted environment. Therefore the

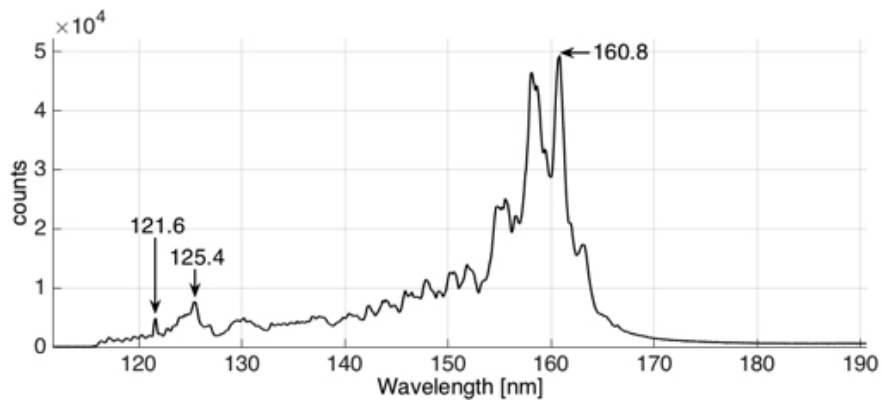
---

<sup>6</sup>charge-coupled device

<sup>7</sup>Electronic readout noise is created during each readout process (determination of the charge accumulated by light exposure). If the charge of several pixels is accumulated and then read out, this kind of noise can be minimized.



(a) spectrometer setup (image taken from [87])



(b) Emission spectrum of the deuterium lamp with calibration peaks

Figure 4.1: UV spectrometer for measuring the crystal transmittance between between 120 – 190 nm.

spectrometer's components are housed in a vacuum chamber for obtaining pressures below  $5 \cdot 10^{-5}$  mbar to avoid spurious signals from atoms and molecules in the residual gas [106, 107].

The instrumental resolution was determined by setting the grating to the blaze angle, thereby imaging the spectrometer's slit directly onto the camera. The best resolution obtained for minimum slit widths was 0.5 nm.

The total efficiency of the spectrometer<sup>8</sup> is  $2 \cdot 10^{-7}$ , which is largely limited by the small solid angle and a grating efficiency of a few percent. The absolute calibration and its reproducibility are better than 1 nm.

### **Transmission spectra between 120-190 nm**

The transmittance of **undoped CaF<sub>2</sub>** crystals depends strongly on the crystal quality, which is determined by the conditions during the growth process. VUV spectra of five different samples (fig. 4.2) taken from four different crystals are compared in figure 4.4. A grating with a groove density of 1200 g/mm was used in all measurements but for V025:3, for which a 300 g/mm grating (lower resolution) was used. The measured transmittance values above 170 nm scatter stronger than for smaller wavelengths since the low intensity of the deuterium lamp leads to a decrease of the signal-to-noise ratio.

Table 4.1 lists the sample thicknesses and doping concentrations of the investigated crystals<sup>9</sup>. For the sample thickness, a lower and an upper limit is given since the polished end faces are not always perfectly parallel. Column 3 lists the mass of thorium fluoride added to CaF<sub>2</sub> before growth. The <sup>232</sup>Th concentration, given in  $N_{Th}/N_{Ca}$ , was determined via NAA (section 3.5.2). The two values given in column 4 were measured directly below and above the crystal samples listed in column 1 (for V029:9, the <sup>232</sup>Th concentration was only measured in the part below the crystal sample).

In some of the samples, white inclusions are visible in the crystal's bulk. They originate from a too low axial temperature gradient during growth (compare section 2.2.4), which probably led to an inward crystallization. This effect is more pronounced in the lower (i.e. the first grown) parts of the crystals: the inclusions are bigger in size and more numerous in V011:3 and V025:2 compared to V011:4 and V025:3 (fig. 4.2b and 4.2d). For the transmittance measurements, the crystal parts with the fewest inclusions were chosen for the beam path.

The pink colour of V014:3 (fig. 4.2c) is due to a growth process abortion because

---

<sup>8</sup>taking into account the solid angle of the focusing mirror, the mirror reflectivity, the grating efficiency and the detection efficiency of the CCD

<sup>9</sup>The part of V038, which was investigated here, was later cut into two pieces (V038:3 and V038:4) for further measurements.

of a vacuum leak. After an emergency switch-off<sup>10</sup>, the partially-grown crystal cooled down very rapidly. The crystal part from which V014:3 was cut out had probably already solidified compared to the upper parts, which are completely opaque. The thermal stress induced by the rapid cool-down together with the oxygen inflow (before the pressure reached the shut-off threshold) caused the pink colouring of the crystal. The resulting low crystal quality is also reflected in the poor VUV transmittance (fig. 4.4).

A difference in crystal quality can also be seen between the two parts of V011, where the upper (later grown) part V011:4 with fewer and smaller inclusions has better transmission properties than V011:3, especially above 150 nm.

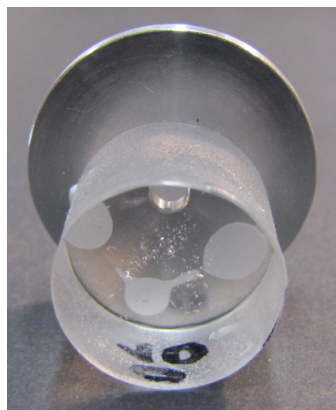
Crystal V025 had a much larger inclusion (bubble) near the crystal bottom, which led to the conclusion that most or maybe all of the seed was molten (the seed showed no such inclusion before growth). The dip in the transmittance curve beneath 150 nm might be explained by that.

The VUV transmission of **thorium-doped CaF<sub>2</sub>** crystals remains at transmittance values comparable to the undoped crystals (fig. 4.5). The theoretically predicted slight reduction of the transmission window (section 3.1.1), i.e. an increase of the lower cut-off frequency, could be observed for several crystals. An increasing thorium concentration often correlated with a reduction of the VUV transmittance, e.g. for V037 (fig. 4.5a), where the <sup>232</sup>Th concentration increases towards the upper parts (V037:6) of the crystal. Since the crystal quality sometimes varied even within the same crystal (like in V011 or V025), the observed correlation could also be attributed to other effects than doping concentration. The crystals doped with a mixture of <sup>229</sup>Th and <sup>232</sup>Th (fig. 4.5b) showed lower transmittance values than undoped or <sup>232</sup>Th-doped CaF<sub>2</sub> probably due to imperfect seeding (compare figs. 2.10b and 2.10c).

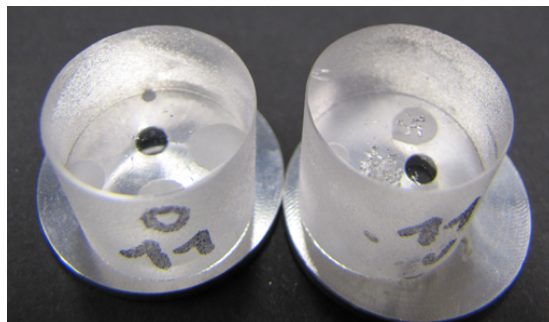
Uranium-doped CaF<sub>2</sub> crystals were investigated to check the feasibility of an alternative experimental approach to indirectly populate the isomeric state of <sup>229</sup>Th inside the bulk of a crystal (section 3.2, [78]). Although U:CaF<sub>2</sub> is widely used as a laser material (references in section 3.2.2), transmission curves in the required spectral range below 200 nm have not been available so far [83, 108]. A 4.1 mm thick disc was cut off of a <sup>238</sup>U:CaF<sub>2</sub> crystal with a doping concentration of  $5 \cdot 10^{-5}$  for transmittance measurements (fig. 4.6). For a wavelength of 160 nm, we measure an absorption coefficient of  $\xi_U(160 \text{ nm}) = 6.3(8) \cdot 10^{-5} \text{ cm}$  (section 3.2.3).

---

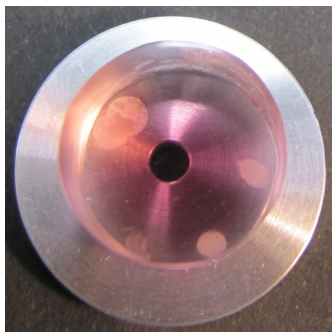
<sup>10</sup>in order to prevent destruction of the graphite insulation by oxidation



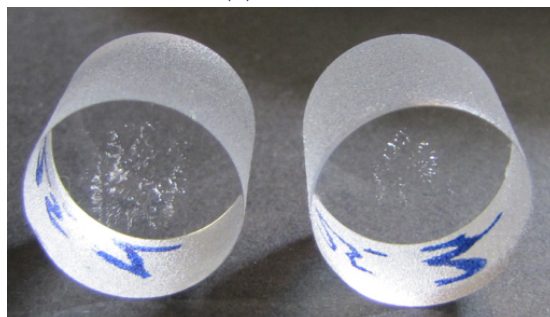
(a) V010:2



(b) V011:4 and V011:3

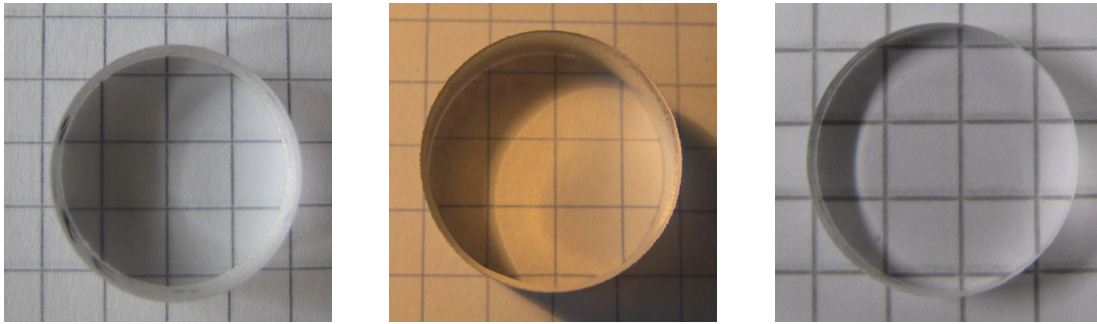


(c) V014:3



(d) V025:2 and V025:3

Figure 4.2: Undoped CaF<sub>2</sub> crystals for VUV transmittance measurements. The crystal diameter, which is determined by the crucible's dimensions, typically is 17.1 – 17.5 mm. The earlier grown crystals were glued onto aluminum sample holders (diameter of 1 inch with a 3 mm aperture) for transmittance measurements.



(a) V037:4

(b) V037:6

(c) V038:4

Figure 4.3: Th-doped  $\text{CaF}_2$  crystals for VUV transmittance measurements. V037 is a  $^{232}\text{Th}:\text{CaF}_2$  crystal, V038 was doped with a mixture of  $^{229}\text{Th}$  and  $^{232}\text{Th}$  (details on the doping concentration in sections 3.5.2 and 3.5.2).

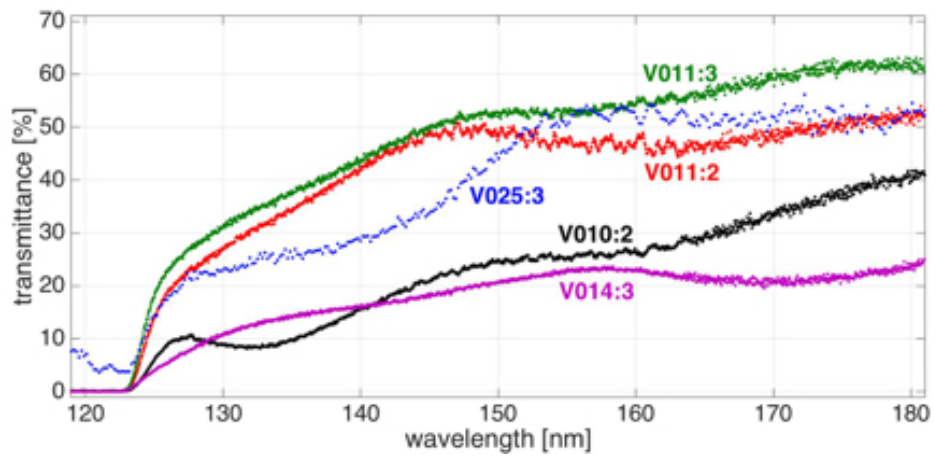
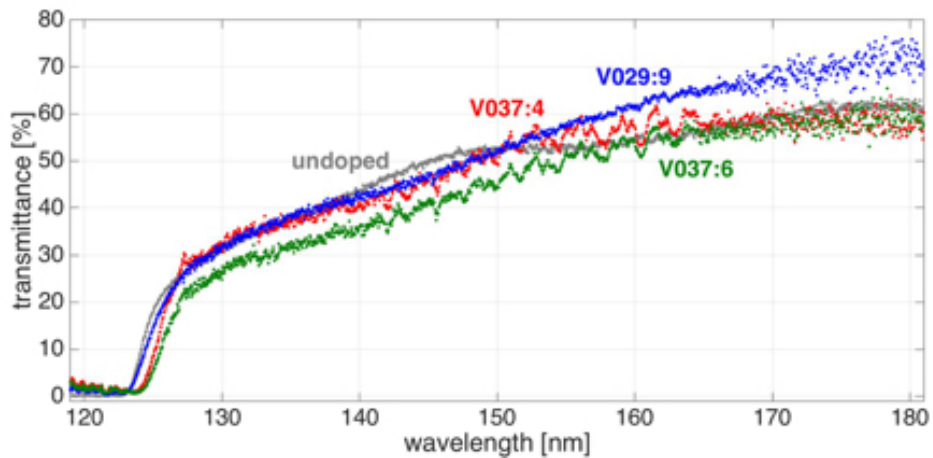


Figure 4.4: VUV transmittance of undoped  $\text{CaF}_2$  crystals

(a)  $^{232}\text{Th}:\text{CaF}_2$



(b)  $^{229}\text{Th}:\text{CaF}_2$

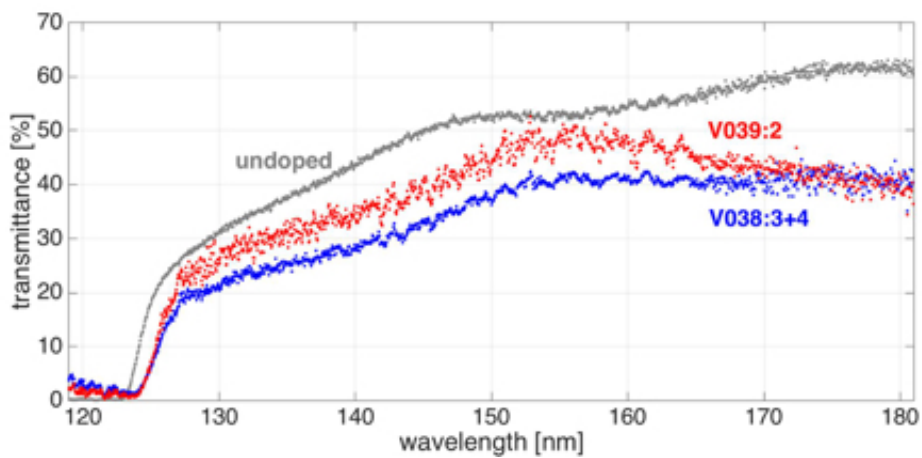


Figure 4.5: VUV transmittance of Th-doped crystals. The transmission spectrum of the undoped  $\text{CaF}_2$  crystal V011:3 is given for comparison.



Table 4.1: Sample thickness and doping concentration of crystal samples.

crystal sample	sample thickness [mm]	dopant	$m_{\text{ThF}_4}$ [mg]	concentration of $^{232}\text{Th}$
V010:2	14.6-14.7	none	0	n/a
V011:3	15.2-15.3	none	0	n/a
V011:4	15.5-15.6	none	0	n/a
V014:3	14.8-14.9	none	0	n/a
V025:3	16.4	none	0	n/a
V029:9	6.0	$^{232}\text{Th}$	6.3	$2.3 \cdot 10^{-5}$ - n/a
V037:4	10,2-10,3	$^{232}\text{Th}$	6.3	$(1.6 - 5.6) \cdot 10^{-5}$
V037:6	11,0-11,1	$^{232}\text{Th}$	6.3	$(5.6 - 19) \cdot 10^{-5}$
V038:3+4	15.0	$^{232}\text{Th}$ and $^{229}\text{Th}$ 1 : 4620	3.3	$(2.5 - 13) \cdot 10^{-5}$
V039:2	19.0	$^{232}\text{Th}$ and $^{229}\text{Th}$ 1 : 4200(200)	3.7	$(9.9 - 11) \cdot 10^{-5}$

#### 4.1.5 Energy-dependent transmission of laser pulses around 160 nm

For the transmittance measurements described in this section, laser pulses at 157 nm and 160 nm were used in contrast to the continuous, broad-band excitation source of the previous section 4.1.4.

Transmittance measurements of several crystal samples were carried out by B. Ullmann with a pulsed fluorine excimer laser<sup>11</sup> at 157 nm [91]. The intensities were determined by means of a pyroelectric energy sensor<sup>12</sup>.

The samples covered cleaved  $\text{CaF}_2$  crystals<sup>13</sup> and commercially available<sup>14</sup> high-quality  $\text{CaF}_2$  (both grown by the Bridgman-Stockbarger method) as well as a Czochralski-grown  $^{232}\text{Th}:\text{CaF}_2$  (fig.3.13), which was cut and polished at the ATI, and several other fluoride crystals. The samples were glued onto sample holders<sup>15</sup> for the transmittance measurements.

The 10.3 mm thick, commercially available  $\text{CaF}_2$  crystal showed a small linear absorptance (transmittance values above 80% for intensities between 200 and 2300 W/mm<sup>2</sup>) and a small absorptance coefficient for effective two-photon-absorptance  $\beta_{eff}$ . The 8.1 mm thick  $^{232}\text{Th}:\text{CaF}_2$  showed a similar transmission

<sup>11</sup>Gamlaser EX5F, VUV 157 nm Fluorine Laser, repetition rate: 20 to 250 Hz, pulse width: 8 ns, maximum energy per pulse: 1.5 mJ, laser beam cross section: 3 mm × 6 mm

<sup>12</sup>Ophir probe PE25-C

<sup>13</sup>grown at the Fraunhofer IISB, Erlangen

<sup>14</sup>purchased from Hellma materials

<sup>15</sup>diameter of 1 inch, aperture of 3.6 mm

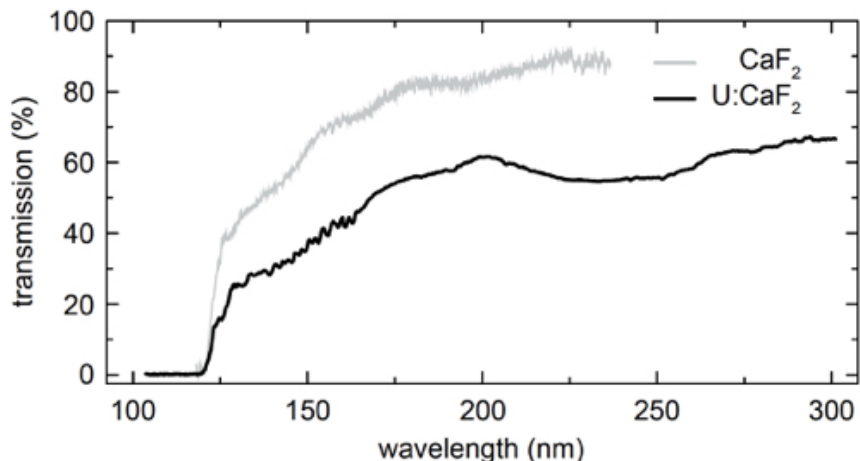


Figure 4.6: UV Transmission of  $^{238}\text{U}:\text{CaF}_2$

The black curve was taken with a crystal of 4.1mm thickness and  $5 \cdot 10^{-5}$  doping concentration, the grey curve shows the transmission of an undoped specimen.

Image taken from [78].

performance although the surface roughness was measured to be one order of magnitude higher for this crystal (root mean square surface deviation of  $R_{rms} = 12$  nm compared to  $R_{rms} = 1.3$  nm).

The cleaved  $\text{CaF}_2$  crystals reached even better surface roughness values locally ( $R_{rms} = 0.3$  nm) but showed atomic steps which can lower the transmittance. Apart from a higher linear absorptance, a non-linear transmittance behavior could be observed for the cleaved crystals.

The transmittance of  $\text{CaF}_2$  crystals<sup>16</sup> doped with cerium (fig. 4.7a) or zirconium (fig. 4.7c) were investigated with the pulsed VUV laser as well [89]. The crystals showed an intense colouring of the illuminated surface region that was continued along the beam path a few millimeters into the bulk. No measurable transmittance of these crystals could be detected. However, the colouring disappeared over the course of a few days.

Creation of colour centers that are visible for the naked eye could also be observed for  $\text{Ce}:\text{CaF}_2$ <sup>17</sup> (fig. 4.7a) and  $^{232}\text{Th}:\text{CaF}_2$ <sup>18</sup> (figs. 4.7b and 3.13) when illuminating them with sub-50-fs pulses at 160 nm (experimental details in section 4.2.1). The intensity of the colouring typically faded within several hours and was completely vanished after few days.

Energy-dependent transmission measurements at 160 nm were also carried out at

<sup>16</sup>grown at the Institut für Kristallzüchtung (IKZ) in Berlin by means of the Czochralski method

<sup>17</sup>grown at the IKZ Berlin with the Czochralski method, see section 3.4

<sup>18</sup>grown at the IKZ Berlin with the Czochralski method, see section 3.5.2

(a) Ce:CaF<sub>2</sub>(b) <sup>232</sup>Th:CaF<sub>2</sub>(c) Zr:CaF<sub>2</sub>

Figure 4.7: Crystal samples used for transmittance measurements

(a) Creation of colour centers in Ce:CaF<sub>2</sub> by illumination with high-intensity laser pulses at 157 nm. Different illumination spots of two measurements with a small beam diameter (2 – 3 mm) are clearly distinguishable. The very left one has already faded compared to brighter spot of the most recent illumination.

The length of the black bar is 18 mm, the sample thickness is 12.8 mm.

(b) This 5 mm thick sample was cut out of the Czochralski-grown <sup>232</sup>Th:CaF<sub>2</sub> crystal in fig. 3.13. The crystal was glued onto a sample holder (diameter of 1 inch) afterwards for measurements described in section 4.1.5.

(c) The middle part (sample thickness: 2 mm) of this Czochralski-grown Zr:CaF<sub>2</sub> was used for transmittance measurements described in section 4.1.5.

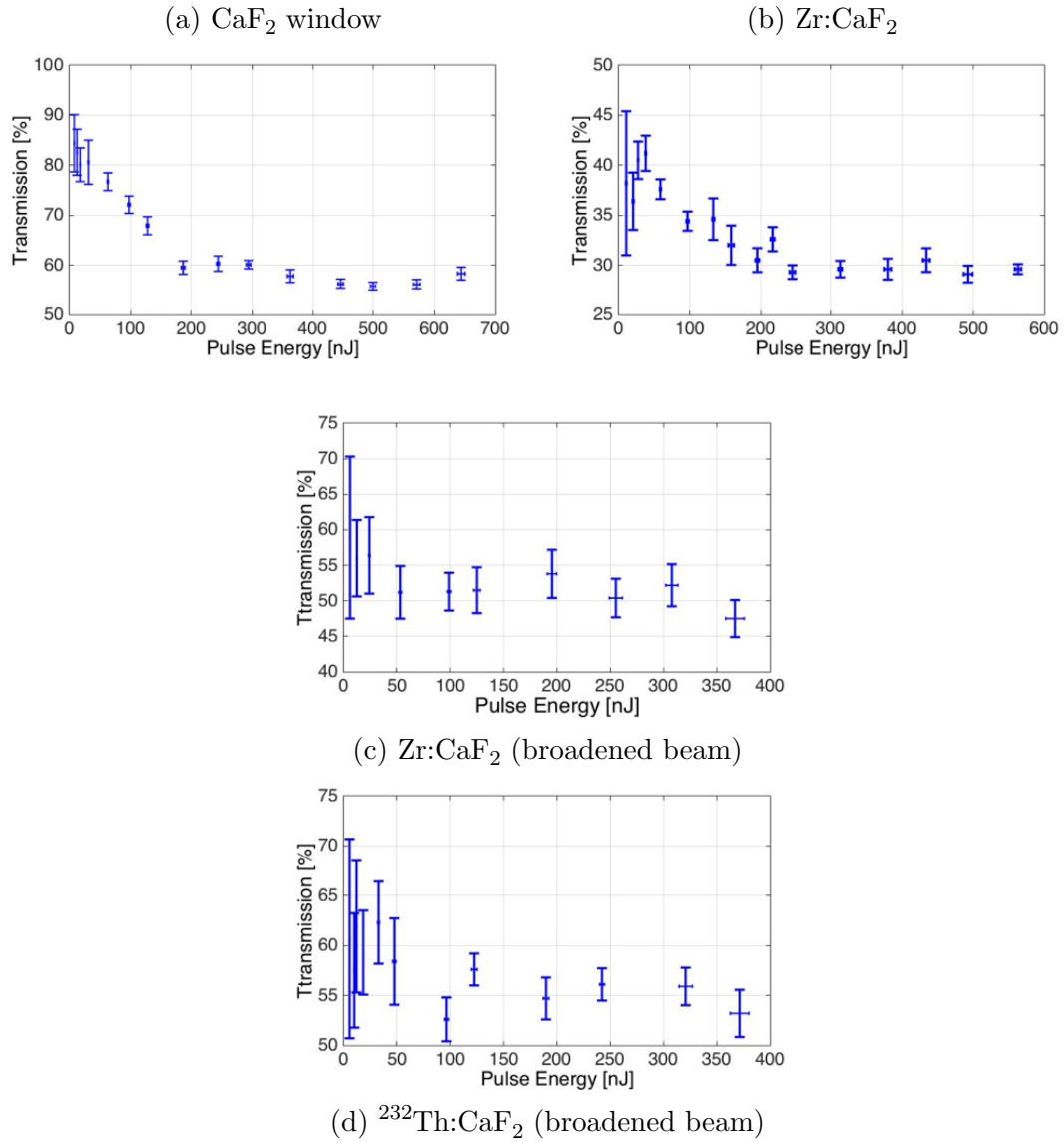


Figure 4.8: Energy-dependent transmittance at 160 nm  
 The beam diameter (measured at 1/e of the maximum intensity) was 2.5(5) mm  
 and 16.5(5) mm (broadened beam).

the MBI Berlin. The transmittance of a commercially available  $\text{CaF}_2$  window<sup>19</sup>, as well as a zirconium-doped  $\text{CaF}_2$  crystal<sup>20</sup> (fig. 4.7c) showed a clear energy-dependence (figs. 4.8a and 4.8b). The beam was broadened from 2.5(5) mm to 16.5(5) mm in diameter for the subsequent measurements. The transmittance of the  $\text{Zr}:\text{CaF}_2$  crystal increased significantly and no intensity-dependence could be observed (fig. 4.8c). The  $^{232}\text{Th}:\text{CaF}_2$  transmittance was only measured with the broadened beam in order to prevent damage to the sample. No clear energy-dependence was found either (fig. 4.8d).

For a pulse length of 50 fs and a beam diameter of 2 mm, we obtain laser intensities on the order of 1 – 400  $\text{MW}/\text{cm}^2$  for the pulse energy range covered by our measurements (1 – 600 nJ). These intensities are still orders of magnitude lower than those for which two-photon processes are expected (1 – 100  $\text{GW}/\text{cm}^2$ ) [109, 110].

## 4.2 Luminescence

Luminescence is the light emitted by matter in response to a stimulus or excitation [111].

First luminescence measurements of doped and undoped  $\text{CaF}_2$  crystals were carried out at the MBI Berlin, where a high-power, short-pulsed VUV laser is available at 160 nm (section 4.2.1). Very long-living luminescence components were found during these experiments, calling for a thorough investigation of the photoluminescence (section 4.2.2) as well as the radioluminescence (section 4.2.3) of the thorium-doped  $\text{CaF}_2$  crystals.

### 4.2.1 Preliminary measurements with short high-power laser pulses at 160 nm

The effect of short high-power VUV laser pulses on doped  $\text{CaF}_2$  was investigated at the Max Born Institute for Nonlinear Optics and Short Pulse Spectroscopy (MBI-Berlin), which houses one of the strongest VUV laser systems at the desired wavelength of 160 nm. It is capable of producing sub-50-fs pulses with energies up to 240 nJ and a repetition rate of 1 kHz. The laser pulses are created by four-wave mixing<sup>21</sup> of the fundamental frequency ( $\cong 800$  nm) and the third harmonic ( $\cong 266$  nm) of a Ti:sapphire laser in argon [112]. A tunable source in the VUV spectral range can be realized in the future by mixing the third harmonic with the output of an optical parametric amplifier. This makes the laser setup at the

<sup>19</sup>manufacturer unknown, thickness of 0.5 mm

<sup>20</sup>grown at the IKZ Berlin

<sup>21</sup>The resulting frequency is  $f_{160\text{nm}} = FF + 2 \cdot TH$ , where  $FF$  is the fundamental frequency and  $TH$  the third harmonic of the Ti:sapphire laser.

MBI Berlin a potential candidate for contributing to the search for the isomeric transition in  $^{229}\text{Th}$ .

Luminescence of  $\text{CaF}_2$  along the beam path of the laser is already visible with the naked eye but Photomultiplier tubes (PMT) allow single-photon detection with a time resolution below 10 ns. Their spectral detection range depends on the material of the photocathode and the entrance window<sup>22</sup>. We used a Hamamatsu R6835 with a Cs-Te photocathode in combination with a  $\text{MgF}_2$  entrance window, having a detection range from 115 nm to 320 nm.

After the illumination of the crystal for a specific time, a mechanical shutter blocked the laser light and the PMT shutter opened. A wait time of around 10 ms ensured that the shutters were fully closed/opened. The PMT signal was amplified and recorded by a SR430 Multi-Channel scaler, which also allows noise discrimination. The photon counts were sorted into time bins<sup>23</sup>, whose bin width could be set from 5 ns to 10 ms. A measurement consisted of several repetitions (records) of the previously described procedure. For each time bin, the counts of all records were added together.

The  $^{232}\text{Th}:\text{CaF}_2$  and the  $\text{Ce}:\text{CaF}_2$  crystal were both illuminated for 1 s with pulse energies of 624(12) nJ and 612(12) nJ respectively and a 3-exponential fit was applied to the luminescence signal (fig. 4.9):

$$\frac{dN}{dt}(t) = a + b \cdot \exp(c \cdot t) + d \cdot \exp(f \cdot t) + g \cdot \exp(h \cdot t). \quad (4.7)$$

The constant offset parameter  $a = 19.8 \text{ ms}^{-1}$  and  $15.6 \text{ ms}^{-1}$  respectively had to be added to take a long-term decaying component into account that could not be included in the faster decaying exponential terms. Similar measurements with an illumination time of 30 ms yielded a lower offset of  $a \simeq 2 \text{ ms}^{-1}$ .

A commercially available<sup>24</sup>, high-quality  $\text{CaF}_2$  crystal was investigated under the same conditions (illumination time of 30 ms, pulse energy of 618(12) nJ), and a much lower long-term luminescence ( $a = 0.6 \text{ ms}^{-1}$ ) was found, which was attributed to the higher crystal quality.

The half-lives of the different components can be found in table 4.2. However, the given values have to be seen a bit skeptically since the measurement time for one record was only 1.34 s (compared to half-lives of a few 100 ms) and an accumulation effect could be observed in other experiments (as described later). These two measurements, on the other hand, were the first ones carried out with these crystals so that no remaining excitations from previous measurements were

---

<sup>22</sup>Spectral filters can be used in addition.

<sup>23</sup>1000 to 32000

<sup>24</sup>purchased from Hellma materials

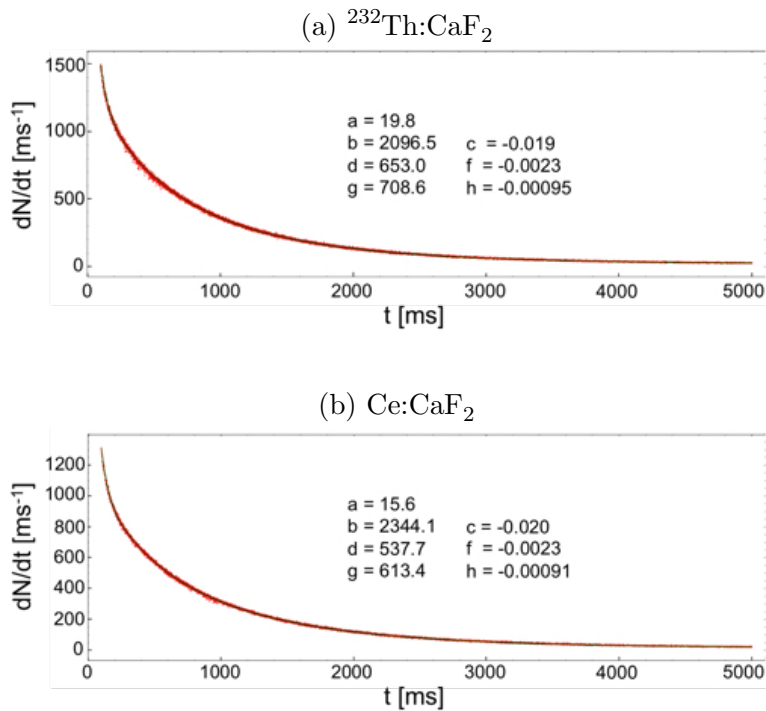


Figure 4.9: Crystal luminescence signal after 1 s illumination with a pulse energy of 620(25) nJ. The parameters for a 3-exponential fit (eq. 4.7) are given in the figures. The corresponding half-lives can be found in table 4.2.

present. An accumulation of excitations from one record of the measurement to the other could not be excluded.

Table 4.2: Luminescence of  $^{232}\text{Th}:\text{CaF}_2$  and  $\text{Ce}:\text{CaF}_2$   
illumination time: 1 s  
pulse energy: 620(25) nJ

luminescence component	$t_{1/2}$ [ms]		relative amplitude [%]	
	Ce:CaF <sub>2</sub>	$^{232}\text{Th}:\text{CaF}_2$	Ce:CaF <sub>2</sub>	$^{232}\text{Th}:\text{CaF}_2$
short-lived	36	34	67	61
medium-lived	298	297	15	19
long-lived	733	761	18	20

In order to determine the long-term luminescence component of the Czochralski-grown  $^{232}\text{Th}:\text{CaF}_2$  crystal, two measurements were compared, during which the crystal was not illuminated. Long-living excitations from previous measurements had not decayed yet. Knowing the time between the two consecutive non-illumination experiments allowed the determination of the long-term luminescence component's half-life of 276 s. This was on the same order of magnitude

as the typical time of many measurements and the time between measurements. Therefore, in many cases excitations from previous measurements had not decayed sufficiently and useful data could only be obtained for the shorter-lived components of the crystal luminescence.

Comparing measurements of the Czochralski-grown  $^{232}\text{Th}:\text{CaF}_2$  crystal with different pulse energies yielded the results given in chronological order in table 4.3 (illumination time was 30 ms) and table 4.4 (illumination time was 240 ms). The measurement time for each record was 350 ms and 560 ms respectively. Therefore, only two exponential curves were fitted to the data. The half-lives of the short- and medium-lived components of the luminescence are given in the tables. Luminescence effects with a longer life-time contribute to the parameter  $a$  (compare to eq. 4.7).

The half-life of the short-term components remained more or less constant. An accumulation effect for the medium-lived component was clearly visible for longer illumination times (table 4.4). For shorter illumination times (table 4.3), only 3 – 4 half-lives passed during the measurement time of one record (350 ms) so that a significant amount of the medium-lived luminescence component of the previous illumination had not decayed yet. The large scattering of the values for parameter  $a$  illustrates the dependence of these values on conditions during previous experiments.

Table 4.3: Luminescence of  $^{232}\text{Th}:\text{CaF}_2$   
with varying pulse energy  
(illumination time: 30 ms)

pulse energy [nJ]	312(9)	127(6)	624(19)
$t_{1/2, short}$ [ms]	27	25	24
$t_{1/2, medium}$ [ms]	100	84	90
$a$ [ $\text{ms}^{-1}$ ]	18	26	73

Table 4.4: Luminescence of  $^{232}\text{Th}:\text{CaF}_2$   
with varying pulse energy.  
(illumination time: 240 ms)

pulse energy [nJ]	611(12)	25(1)	25(1)	124(6)
$t_{1/2, short}$ [ms]	26	30	31	30
$t_{1/2, medium}$ [ms]	161	220	240	275
$a$ [ $\text{ms}^{-1}$ ]	710	7	6	31

These first luminescence measurements at the MBI Berlin revealed unexpected long-term components of crystal luminescence. After the data analysis, it became clear that longer times are required (1) for the single records for better quantification as well as (2) between the measurements to give the long-lived components



enough time to decay between the measurements. The measurements also showed that the crystal's photoluminescence depends less on the dopant and the doping concentration than on the properties of the  $\text{CaF}_2$  host crystal. This emphasizes the importance of the growth process which determines the crystal quality.

#### 4.2.2 Photoluminescence

The strong and long-lived luminescence measured in doped and undoped  $\text{CaF}_2$  crystals (see previous section 4.2.1) required further investigation. Therefore, an Excimer-laser (section 4.1.5) operating at 157 nm was set up [89, 91]. Since the laser beam is absorbed by (atmospheric) oxygen, measurements had to be carried out either in a nitrogen atmosphere or in vacuum. Two photomultiplier tubes (PMTs) of different design and different spectral detection range<sup>25</sup> were used for measuring the emitted luminescence photons. A summary of the experimental results obtained by Christoph Tscherne [113] and Simon Stellmer [87] is given in the following.

First, an undoped  $\text{CaF}_2$  crystal<sup>26</sup> was compared to a  $^{232}\text{Th}:\text{CaF}_2$  crystal<sup>27</sup> (fig. 3.13) in the wavelength range 115 – 320 nm. A linear relation between the emitted photon counts and the absorbed energy was found in both crystals, whereas the temporal evolution of the luminescence signal (normalized to the maximum intensity) was independent of the energy deposited during illumination.

The  $^{232}\text{Th}:\text{CaF}_2$  crystal showed a significantly slower decay of its luminescence signal compared to the  $\text{CaF}_2$  crystal (fig. 4.10). Exponential fitting with two or three decay constants (eq. 4.7) yielded half-lives around 70 ms, 350 ms (relative amplitudes of 0.7 and 0.3) and  $> 7$  s for the luminescence components of the  $\text{CaF}_2$  crystal. For the  $^{232}\text{Th}:\text{CaF}_2$  crystal, the half-lives of the luminescence components were around 70 ms, 1.4 s (relative amplitudes of 0.8 and 0.2) and  $> 9$  s. Using the PMT with the extended spectral range (115 – 320 nm) did not only increase the luminescence signal (due to self-trapped excitons, described later) but added a longer living decay component (half life around 70 s, relative amplitude of 0.1) to the luminescence signal of the  $^{232}\text{Th}:\text{CaF}_2$  signal.

Since the experimental conditions in the measurements of section 4.2.1 were quite different (pulse energy, illumination time, repetition rate, previous treatment of the crystals etc.), the exact reasons for the different half-lives obtained here (compared to tables 4.2, 4.3 and 4.4) remain unclear.

The VUV-photoluminescence of  $^{232}\text{Th}:\text{CaF}_2$  and  $\text{CaF}_2$  crystals grown by the vertical gradient freeze method was spectrally resolved by the UV spectrometer de-

<sup>25</sup>Hamamatsu R6836 (type: head on), detection range: 115 – 320 nm and Hamamatsu R8487 (type: side-on), detection range: 115 – 195 nm

<sup>26</sup>grown by the Bridgman-Stockbarger method in Fraunhofer Institute IISB, Erlangen

<sup>27</sup>grown at the Institut für Kristallzüchtung (IKZ) in Berlin by means of the Czochralski method

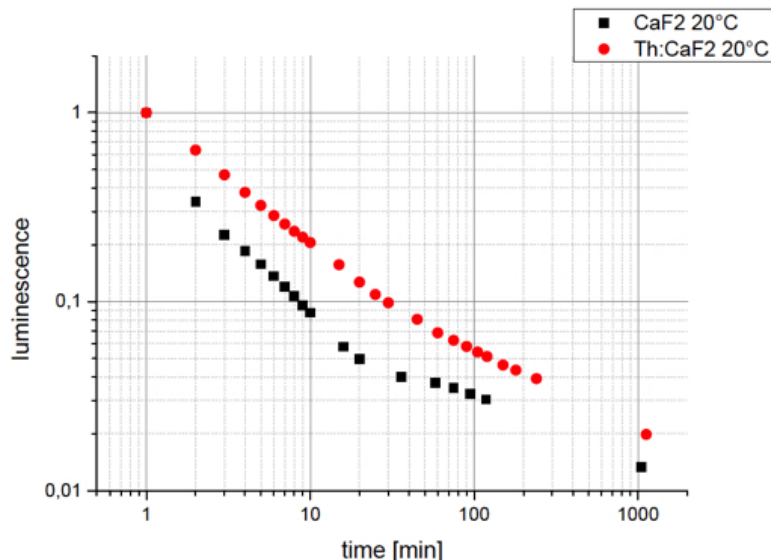


Figure 4.10: Temporal evolution of the luminescence of  $\text{CaF}_2$  and  $^{232}\text{Th}:\text{CaF}_2$ . The measurements have been carried out at  $20^\circ\text{C}$  in a spectral range of  $115 - 320\text{ nm}$  after an illumination time of  $60\text{ s}$ . The decay curves were normalized to their maxima. Image taken from [113].

scribed in section 4.1.4. This revealed a self-trapped exciton (STE) spectrum consisting of nine overlapping lines between  $260$  and  $500\text{ nm}$  (fig. 4.11b), but no discernable features below  $260\text{ nm}$  (fig. 4.11a). The peak energies of the fitted Gaussian functions were almost equally spaced (inset of fig. 4.11b), suggesting that they represent oscillator states in the harmonic STE potential. Their spectral positions are independent of crystal temperature, wait time after illumination, light intensity and emission spectrum of the deuterium lamp. Their relative amplitudes, however, do change with time and depend on the spectrum of the excitation source. The magnitude of the luminescence emission depends on the quality and purity of the crystal, rather than on the influence of the thorium doping concentration.

Using an excimer laser at  $157\text{ nm}$  as an excitation source shows a double-exponential decay for time-scales shorter than  $100\text{ s}$  (fig. 4.11c) and a power-law decay (fig. 4.11d) for times longer than one minute. The amplitude of the faster decay is at least 10-times larger compared to the slower branch. A detailed description can be found in [87].

### 4.2.3 Radioluminescence

Alpha decays of  $^{229}\text{Th}$  in the crystal create a lot of defects. The alpha particle and the  $^{225}\text{Ra}$  nucleus obtain kinetic energies of  $5.1\text{ MeV}$  and  $90\text{ keV}$ , enough for traveling ranges of  $30000$  and  $30$  lattice constants through the crystal and

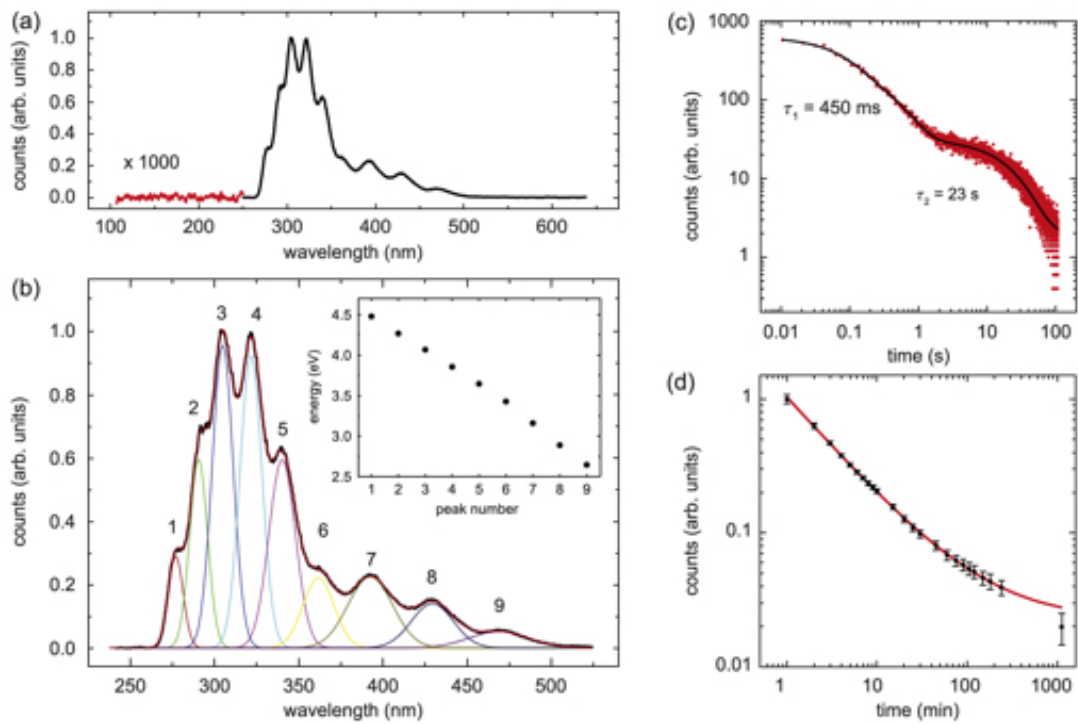


Figure 4.11: VUV-photoluminescence of  $\text{CaF}_2$

The STE spectrum is an overlap of nine different oscillator states above 260 nm in a harmonic potential (a&b). For timescales shorter than 100 s, the photoluminescence shows a double-exponential decay ( $\exp(-t/\tau_n)$ ) with the life-times given in (c). For timescales up to 20 h, a power law,  $I(t) = I_0 \cdot (c + t^{-k})$  with  $k = 0.75(2)$ , is observed (d). The offset  $c$  is related to radioluminescence (section 4.2.3). Image taken from [87].

leaving behind a track of defects. Some of these defects relax via emission of photons, a phenomenon known as scintillation. While each alpha decay releases enough energy to create  $10^6$  photons, only  $1.0(2) \cdot 10^4$  photons in the UV range are generated in  $\text{CaF}_2$ , while most of the kinetic energy is converted into phonons. The UV photons following an alpha decay are released in flashes with durations of a few  $\mu\text{s}$ . Typically, about 200 counts are detected by a PMT during such a photon flash, enabling a very effective detection of alpha decays in  $\text{CaF}_2$  crystals. The rate of such events matches the  $^{229}\text{Th}$  concentration determined by neutron activation analysis.

In addition, all the daughter products of  $^{229}\text{Th}$  down to  $^{209}\text{Bi}$  are short-lived (half-lives between  $3.7 \mu\text{s}$  and 15 days), such that each  $^{229}\text{Th}$  decay is followed by a chain of four alpha and three beta decays. The results of the radioluminescence measurements obtained by Simon Stellmer [78, 87] are summarized in the following.

In order to spectrally resolve the radioluminescence of a  $^{229}\text{Th}:\text{CaF}_2$  (fig. 4.12a) crystal<sup>28</sup> with the UV spectrometer (section 4.1.4), long integration times up to 100 h are necessary. For comparison, a  $^{232}\text{Th}:\text{CaF}_2$  crystal was measured, whose doping concentration was very high<sup>29</sup> to compensate for the significantly longer half-life of  $^{232}\text{Th}$  ( $1.4 \cdot 10^{10}$  a) compared to that of  $^{229}\text{Th}$  (7932(28) a). The obtained radioluminescence spectrum of the highly-doped  $^{232}\text{Th}:\text{CaF}_2$  crystal was identical to that of fig. 4.12a. The radioluminescence spectrum of thorium-doped  $\text{CaF}_2$  crystals showed no emission below 220 nm, allowing spectral distinction from the expected photon emission of the isomeric transition in  $^{229}\text{Th}$ .

Recording the radioluminescence of a previously annealed  $^{229}\text{Th}:\text{CaF}_2$  crystal yields the histogram plotted in fig. 4.13a. Feature  $3_I$  contains the photon flash following an alpha decay of  $^{229}\text{Th}$ , features  $3_{II}$  and  $3_{III}$  those of two or three alpha decays within a short time. Feature 2 consists of beta decay photons of  $^{229}\text{Th}$  daughters and possibly of contaminations in the crystal, whereas feature 1 will be explained in section 4.2.3. The highly-doped  $^{232}\text{Th}:\text{CaF}_2$  crystal yields similar features, except for the peak B, attributed to a crystal contamination of  $^{229}\text{Th}$  at a level of 0.8(1) ppm relative to the  $^{232}\text{Th}$  content (details in [87]). The Czochralski-grown  $^{232}\text{Th}:\text{CaF}_2$  crystal (doping concentration of  $2 \cdot 10^{-4}$ ), which showed negligible signs of photoluminescence, yielded the same feature A, corresponding to alpha decays of  $^{232}\text{Th}$ . We conclude that the observed radioluminescence is a generic scintillation feature of  $\text{CaF}_2$  and does not depend on the details of the crystal growth and in particular of the doping.

**U:CaF<sub>2</sub>** crystals showed the same characteristic photon bursts (same photon numbers, temporal evolution, luminescence spectrum and temperature depen-

---

<sup>28</sup>grown at ATI by the vertical gradient freeze method, doping concentration  $N(^{229}\text{Th})/N(\text{Ca}^{2+}) > 1 \cdot 10^{-8}$   
<sup>29</sup> $N(^{232}\text{Th})/N(\text{Ca}^{2+}) > 4 \cdot 10^{-3}$

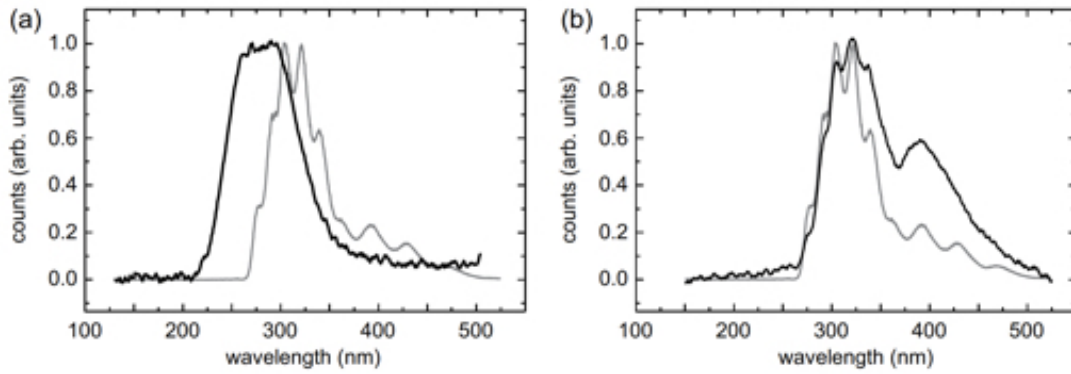


Figure 4.12: Radioluminescence spectra of  $^{229}\text{Th}:\text{CaF}_2$

(a) Spectrum of “prompt” scintillation (black line), compared to a scaled photoluminescence spectrum (gray line). The instrumental resolution was 15 nm.  
 (b) Thermoluminescence spectrum, obtained while heating the crystal to  $150^\circ\text{C}$  (black line). The heating anneals semi-permanent defects under photon emission. The positions of the individual peaks were identical to those observed in photoluminescence (gray line). The resolution here was 1.5 nm.

Image taken from [87].

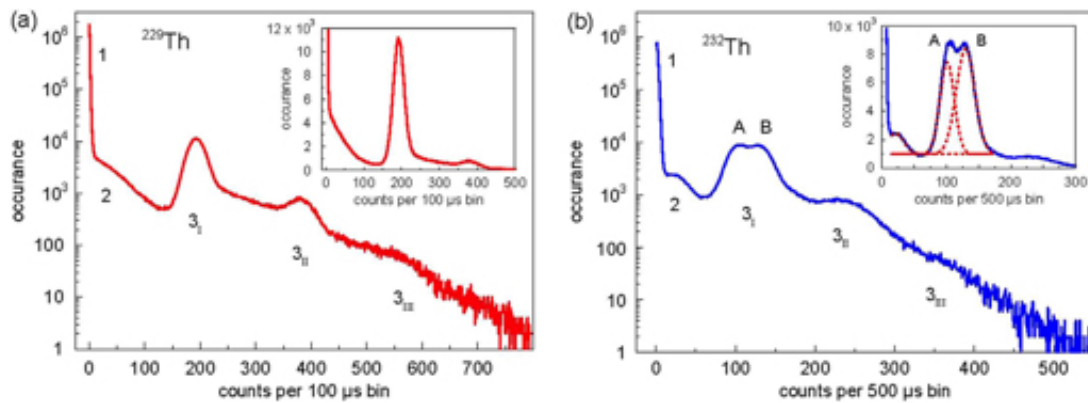


Figure 4.13: Radioluminescence bursts induced by alpha decay

- (a)  $^{229}\text{Th}:\text{CaF}_2$   
 (b)  $^{232}\text{Th}:\text{CaF}_2$

The histograms were obtained by measuring with a PMT (sensitivity range 115 to 320 nm, bin width:  $100\ \mu\text{s}$  and  $500\ \mu\text{s}$ ) at the single-photon level. A section of the data is also plotted on a linear scale (inset). Image taken from [87].

dence) with an occurrence corresponding to the alpha activity of the dopant.

In order to identify the kind of radiation that causes the major peak of the radioluminescence spectrum between 220 and 360 nm, selective absorbers were placed between a  $^{233}\text{U}$  sample and a  $\text{CaF}_2$  crystal. Shielding the crystal from  $^{229}\text{Th}$  recoil nuclei causes a 20% drop of the radioluminescence signal. It drops to 10% by blocking the alpha particles in addition. The measurement suggests that the radioluminescence background is caused predominantly by alpha particles, with much smaller contributions from recoil nuclei and gammas. This finding is consistent with the fact that more than 99% of the energy deposited into the crystal from radioactive decay of our  $^{233}\text{U}$  source is via alpha particles [78].

Placing a commercial, high-quality  $\text{CaF}_2$  crystal into the core of a shut-down TRIGA Mark II reactor, where it is exposed to a massive flux of gamma rays but shielded from alpha and beta radiation by the water surrounding the fuel rods, shows that in the absence of crystal contaminations, gamma radiation does not induce noticeable long-lived defects.

Exposing the crystals to a strong source of alpha radiation did neither create any damage or coloring of the crystal, nor reduced the optical transmission. Ten minutes after the exposure, no long-lived defects could be observed (alpha-induced radioluminescence decays on the order of  $\mu\text{s}$ ).

### Thermoluminescence

Heating up the  $\text{CaF}_2$  crystal leads to an increase in luminescence photons, which peaked around  $60^\circ\text{C}$ , followed by a strong decrease up to  $100^\circ\text{C}$  (fig. 4.14). By adding thermal energy, defects can leave their metastable states between valence and conduction band, returning to their ground state under emission of photons (increase in luminescence). For higher temperatures, non-radiative transitions become more likely. When the thermal energy exceeds the so-called quenching energy, the photon yield diminishes (extinction of luminescence) [114]. These competing effects explain the maximum in fig. 4.14.

In doped  $\text{CaF}_2$  crystals, ionizing radiation can create semi-permanent defects with lifetimes of several weeks or months. Such excitations are often related to impurities or already-existing crystal defects. By heating the crystal, these excitations can be annealed, i.e. excited electrons can leave their traps and relax into the ground state by photon emission. This effect is also exploited in thermoluminescence dosimeters based on  $\text{CaF}_2$ , where the glow curve, i.e. photons emitted during heating, provides information about the absorbed radiation. In the following, the results presented in [87] will be summarized.

When heating a  $^{229}\text{Th}:\text{CaF}_2$  crystal that had accumulated long-lived defects for several weeks, the spectrum shown in fig. 4.12b is obtained. The position

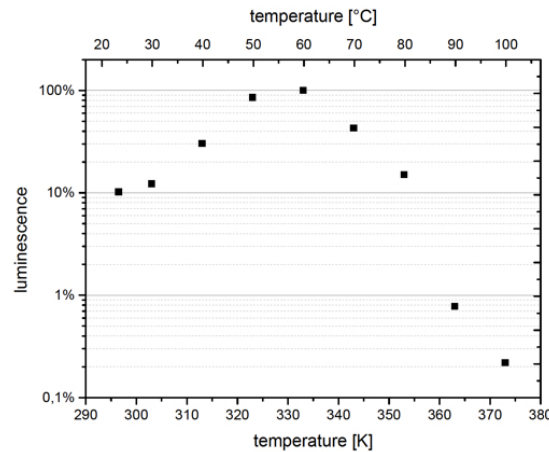


Figure 4.14: Temperature dependence of  $\text{CaF}_2$  luminescence. The crystal was previously heated to  $130^\circ\text{C}$  and the temperature kept at  $100^\circ\text{C}$  for annealing. Then, the crystal temperature was reduced stepwise. For each step, 60 s after illuminating the crystal for 60 s, the luminescence counts between 115 and 320 nm were recorded. Image taken from [113].

of the overlapping lines (but not their relative amplitudes) coincide with those of the photoluminescence spectrum. The crystal defects created by alpha decays have a lifetime of months, and slowly relax under emission of single uncorrelated photons. These photons pose a permanent background in nuclear spectroscopy measurements and can only be reduced by periodic annealing of the crystal. They, and not the PMT dark counts, are the reason for the observed feature 1 in fig. 4.13.

The temperature dependence of the radioluminescence in  $^{229}\text{Th}:\text{CaF}_2$  is shown in fig. 4.15. In future nuclear spectroscopy measurements of  $^{229}\text{Th}$ , additionally to a PMT for detecting the photons emitted by the nuclear transition, a second PMT that is sensitive around 300 nm could be used for detecting photon flashes following an alpha decay event. The radioluminescence background could be drastically reduced by eliminating the time intervals of the photon bursts (veto time) during post-processing of the data or on-line with a suitable gating scheme. Furthermore, the radioluminescence can be reduced by a factor of 10 by heating the crystal to around  $100^\circ\text{C}$ . In addition, the duration of characteristic flashes would decrease, which in turn reduces the veto time imposed onto the primary detector.

### Cherenkov radiation

Cherenkov radiation is caused by charged particles (electrons, in our case) passing through the crystal at velocities larger than the speed of light in the medium. This

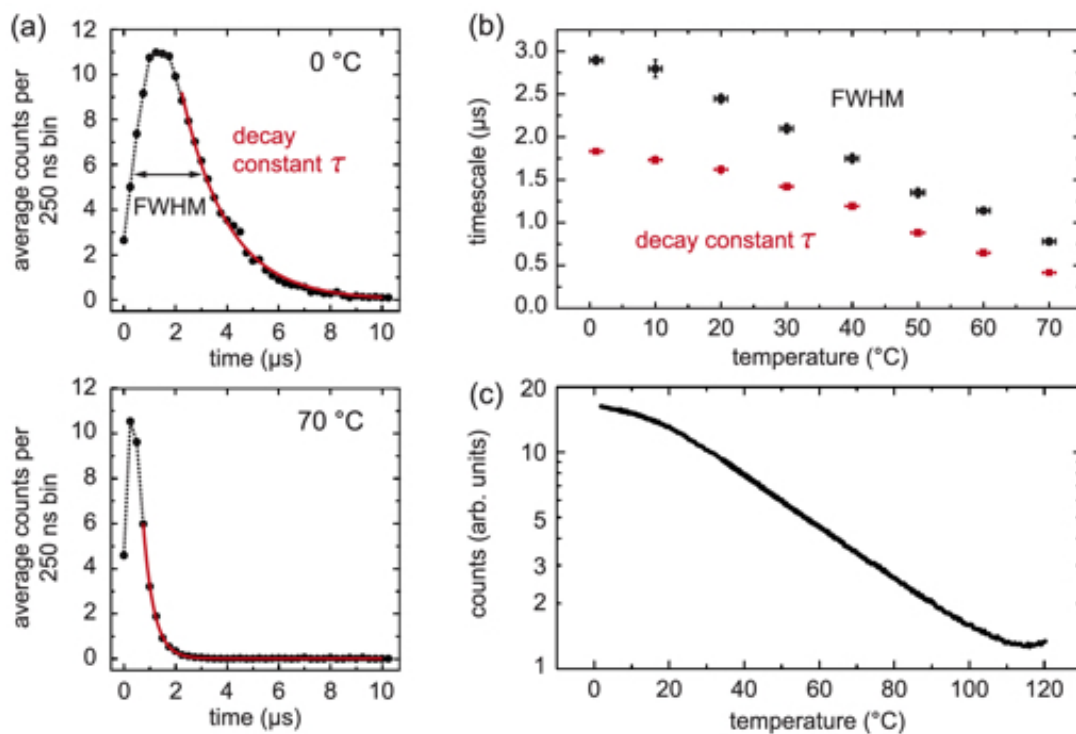


Figure 4.15: Temperature dependence of radioluminescence in  $^{229}\text{Th}:\text{CaF}_2$   
 (a) Time evolution of a burst of photons following an alpha decay, shown for two different temperatures. An exponential decay (red line) is fit to the tail of the distribution.  
 (b) The duration of a burst depends on temperature, quantified here by the full width at half maximum (FWHM) and the decay constant  $\tau$  of the burst.  
 (c) The integrated photon emission changes by a factor of 10 between 20 and 100 °C.

Image taken from [87].



speed is determined by the wavelength-dependent refractive index of the material. Therefore, the emission spectrum is a convolution of the crystal's transmission and its refractive index, both of which change smoothly with wavelength. Cherenkov radiation thus poses a locally homogeneous background rather than a sharp peak that could interfere with the sought-after isomeric signal. A detailed treatment can be found in [78], a summary thereof will be given in the following.

The sources of Cherenkov radiation (or the electrons causing it) are conversion electrons accompanying radioactive transformations of nuclei, electrons from beta decays and highly energetic gammas, which interact with the crystal via the photoelectric effect (predominantly below 100 keV), Compton scattering (100 keV to 10 MeV) and pair production (above 10 MeV). In  $\text{CaF}_2$  crystals, only Compton scattering of gamma radiation needs to be taken into account since the typical energy generated by the photoeffect is too low for generating electrons that are fast enough. The energy required for pair production on the other hand is too high to be caused by radioactive decay of any of our dopants or their daughter nuclei.

Cherenkov radiation can be separated from other forms of radioluminescence due to its temperature-independence. In  $^{229}\text{Th}:\text{CaF}_2$ , less than 1% of the photons emitted as a result of radioactivity comprised of Cherenkov radiation [87].

In  $^{233}\text{U}:\text{CaF}_2$  crystals, used for indirectly populating the isomeric state of  $^{229}\text{Th}$  (section 3.2.1), Cherenkov radiation from  $^{232}\text{U}$  contamination (see below) poses the dominant background, possibly masking the signal from the optical deexcitation of the  $^{229}\text{Th}$  isomer.

A minimum energy is required for creating electrons with a sufficiently high energy to cause Cherenkov radiation at a specific wavelength. Therefore, quite a few isotopes and/or decay channels can be excluded to be the source of Cherenkov radiation in our crystals (details in [87]). Alpha decay of  $^{233}\text{U}$  alone is not accompanied by a large enough number of conversion electrons or gammas of sufficiently high energy. Daughter nuclei of  $^{229}\text{Th}$  on the other hand produce enough high-energy electrons via beta decay, electron conversion or gamma radiation. Chemical purification of the  $^{233}\text{U}$  is expected to remove 99.5% of the thorium, reducing the initial Cherenkov radiation by a factor of 200, with a very slow build-up over the  $^{229}\text{Th}$  lifetime.

$^{233}\text{U}$  typically contains non-negligible amounts of  $^{232}\text{U}$  as a by-product. The short half-life of  $^{232}\text{U}$  (70.6 a) and its daughter nucleus  $^{228}\text{Th}$  (1.9 a) lead to a high activity of the entire chain. Unlike the  $^{233}\text{U}$  chain, which pauses at  $^{229}\text{Th}$  for nearly 8000 years, the  $^{232}\text{U}$  chain proceeds down to the stable  $^{208}\text{Pb}$  on timescales comparable to the duration of the experiment, including strong gamma emission. The content of  $^{232}\text{U}$  in the  $^{233}\text{U}$  source has been measured to be 11.6(1.0) ppm using gamma spectroscopy. At this level, gamma and beta decays of the  $^{232}\text{U}$  chain clearly dominate over the  $^{233}\text{U}$  chain [87]. For the experiment proposed in section

3.2.1, the  $^{232}\text{U}$  content must therefore be minimized in the  $^{233}\text{U}$  source.

### 4.3 Spectrally narrow features with a long life-time

Exposing various commercially available  $\text{CaF}_2$  crystals to intense gamma radiation<sup>30</sup> of a shut-down TRIGA Mark II reactor yields (in some cases) two spectrally narrow features in the luminescence spectrum. The dominant one is at 312 nm and has a linewidth of less than 1.2 nm and a lifetime of 3.1(1) hours, matching expected values for the  $^{229}\text{Th}$  isomeric signal. The same narrow feature can be induced by VUV light from a deuterium lamp (section 4.1.4) [78]. Another peak is observed at 420 nm, which is caused by F-centers.

Typically, crystal defects show broad features in the spectrum with a width of 10 nm and a much faster, non-exponential decay. However,  $\text{Gd}^{3+}$  ions show a narrow emission at a wavelength of 312 nm<sup>31</sup>, leading to the speculation that crystal defects induced by the gamma radiation slowly transfer their energy onto these  $\text{Gd}^{3+}$  ions, which radiate with the mentioned characteristics.

Such spectral features resembling the sought-after isomeric photons have to be excluded by comparing different types of crystals, which differ in material of the host crystal, growth techniques and conditions, dopants (and contaminations) and doping concentration. Furthermore, different isotopes follow different decay chains and therefore introduce different daughter nuclei as crystal contaminations. Such a comparison can also help excluding signals similar to the photonic isomeric transition.

---

<sup>30</sup>The crystals were shielded from alpha and beta radiation by the water surrounding the fuel rods.

<sup>31</sup>private communication with E. Peik

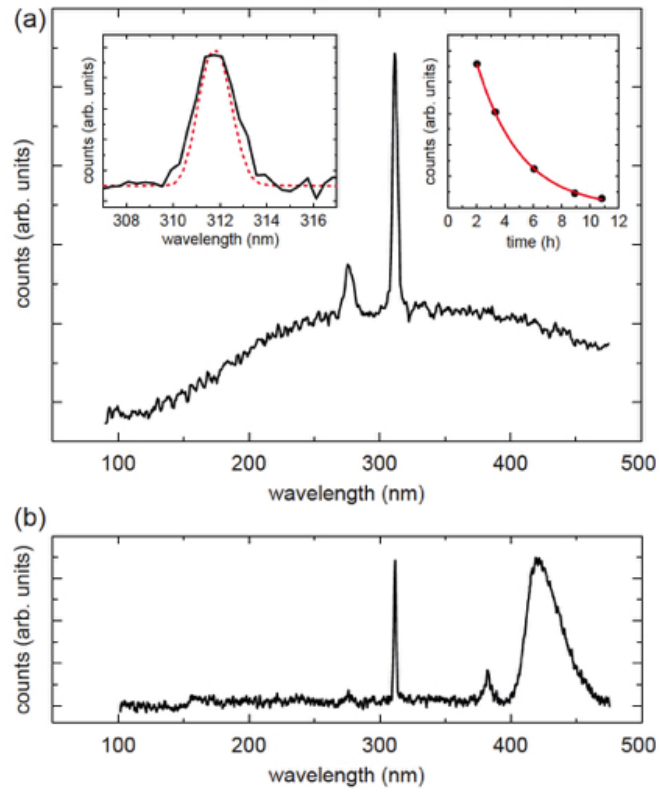


Figure 4.16: Spectrally narrow feature caused by contamination in CaF<sub>2</sub>. The peak around 312 nm occurs in the luminescence spectrum of commercially available CaF<sub>2</sub> after illumination with either gamma radiation (a) or UV light (b). The exponential decay of this peak is plotted in the right inset of (a). The peak at 420 nm is attributed to F-centers. Image taken from [78].



## 5 Conclusion & outlook

The isomeric transition in  $^{229}\text{Th}$  is predicted in an energy range corresponding to wavelengths in the UV (150 – 170 nm). Calcium fluoride was investigated as a possible host crystal for a spectroscopic search for the nuclear transition. The simply cubic lattice and similar ionic radii, that could facilitate embedding of thorium atoms, made  $\text{CaF}_2$  an interesting candidate. Very little was known beforehand, how the dopant affects crystal properties like the UV transmission.

Thorium is embedded into the  $\text{CaF}_2$  lattice as  $\text{Th}^{4+}$  where it replaces a  $\text{Ca}^{2+}$  ion. The charge imbalance between those ions has to be compensated, introducing inhomogeneities into the lattice. Numerical modeling by means of the GULP code showed that charge compensation by two fluorine interstitials in a  $90^\circ$  configuration is energetically favorable compared to a calcium vacancy. Ab-initio calculations based on the VASP code yielded an only slightly reduced band gap of the crystal, thus predicting that thorium-doped  $\text{CaF}_2$  is still transparent in the UV range.

At the moment, the chemical environment of thorium in the  $\text{CaF}_2$  lattice can only be predicted theoretically. The achievable doping concentrations are still too low for experimental techniques like x-ray diffraction, neutron scattering or nuclear magnetic resonance. The quadrupole level structure of the isomer and the ground state could reveal more information about neighbouring atoms of  $^{229}\text{Th}$ . Different charge compensation configurations generate different electric field gradients at the location of the nucleus. The quadrupole level splittings caused thereby can be distinguished by future laser spectroscopy.

Thorium-doped crystals were required to experimentally determine their optical properties. The readily available isotope  $^{232}\text{Th}$  is chemically identical to  $^{229}\text{Th}$ , and could therefore be used in the growth of doped crystals for optical characterization. The first  $^{232}\text{Th}:\text{CaF}_2$  crystal, grown by means of the Czochralski method, showed a promising doping efficiency of  $\sim 30\%$  and the UV transmission in the wavelength region 150 – 170 nm above 50%.

The production of  $^{229}\text{Th}:\text{CaF}_2$  crystals could not be carried out at an external crystal growth facility since small-volume crystals with a high doping concentration of  $^{229}\text{Th}$  were required. The much higher radioactivity of  $^{229}\text{Th}$  compared to  $^{232}\text{Th}$  made the development of our own furnace for crystal growth necessary.

By using the vertical gradient freeze method, a total number 53 crystals were grown, typically taking a week for each growth process. Most of them (32) were

pure calcium fluoride crystals in order to find suitable parameters for optimal growth conditions. By adding different dopants, we have produced 21 doped crystals:  $^{232}\text{Th}:\text{CaF}_2$  (10),  $^{229/232}\text{Th}:\text{CaF}_2$  (3),  $\text{U}:\text{CaF}_2$  (7),  $\text{Zr}:\text{CaF}_2$  (1). Finding the correct temperature settings, for which the seed is only partially molten, proved to be the most difficult challenge, especially for varying dopants and doping concentrations.

It was shown that very high doping concentrations of  $^{232}\text{Th}$  (replacing up to 0.7% of the calcium atoms) could be achieved. The dopants were typically concentrated in the bulk rather than near the surface of the crystals. There is an increase in doping concentration throughout the process, leading to the highest concentration in the region that crystallizes last. A carry-over of doping material between growth processes was found that still requires more investigations.

A highly-doped  $^{229/232}\text{Th}:\text{CaF}_2$  crystal, containing  $\sim 10^{15}$   $^{229}\text{Th}$  nuclei per  $\text{cm}^3$ , was grown for a future search of the isomeric transition with a synchrotron. Measurements at the Metrology Light Source, Berlin are currently in preparation.

UV spectroscopy confirmed that the UV transmittance of the  $^{232}\text{Th}:\text{CaF}_2$  and  $^{229/232}\text{Th}:\text{CaF}_2$  crystals is smaller than in commercially available, high-quality  $\text{CaF}_2$  but still sufficiently high ( $> 40\%$ ) in the wavelength range corresponding to the expected isomer energy.

The photonic signal coming from the isomer is possibly hidden in background noise posed by photo- and radioluminescence. A thorough characterization is required for estimating the expected signal-to-noise ratio.

The photoluminescence spectrum of (doped)  $\text{CaF}_2$  shows nine overlapping lines between 260 and 500 nm caused by self-trapped excitons. The magnitude of the luminescence emission varies by a factor of 5 within our grown crystals (not correlated with the doping concentration) and is at least four orders of magnitude higher than in commercially available high-quality  $\text{CaF}_2$  crystals. It was shown that photoluminescence depends rather on the crystal quality and purity than on the influence of the dopant. Improvements in the growth process or in the quality of the raw material are therefore necessary for reducing this kind of background in the search for isomeric photons. However, no photoluminescence features were found below wavelengths of 260 nm, so that spectral filtering can eliminate most of the noise between 150 and 170 nm, where the isomeric transition is predicted.

The radioluminescence background is mainly caused by alpha particles, with much smaller contributions from recoil nuclei and gammas. Photon bursts with durations of a few  $\mu\text{s}$  follow each alpha decay in  $\text{CaF}_2$  and were observed in uranium- and in thorium-doped crystals. This prompt photons are a generic scintillation feature of  $\text{CaF}_2$  and their spectrum does not depend on the crystal quality. Prompt radioluminescence photons are emitted above 220 nm in  $\text{CaF}_2$ , allowing to distinguish them from isomeric photons, both spectrally and due to the temporal evolution of their emission. Radiation damage also causes the emission of

---

delayed photons, which can be reduced by annealing the crystal.

Spectrally narrow features with a long life time can be induced by gamma or UV radiation in  $\text{CaF}_2$  crystals. They resemble the sought-after photonic deexcitation of the isomer and can be excluded by comparing various types of crystals, which differ in material of the host crystal, growth techniques and conditions, dopants (and contaminations) and doping concentration.

An alternative experimental approach of populating the  $^{229}\text{Th}$  isomer is based on the alpha decay of  $^{233}\text{U}$ . Estimations give an isomeric photon emission rate that is a factor 160 higher in uranium-doped crystals compared to surface implantation techniques. Seven  $\text{U}:\text{CaF}_2$  doped with the isotopes  $^{238}\text{U}$  (4),  $^{233}\text{U}$  (2) and  $^{232}\text{U}$  (1), were grown. In  $^{233}\text{U}:\text{CaF}_2$  crystals, Cherenkov radiation poses the dominant background, possibly masking the signal from the optical deexcitation of the  $^{229}\text{Th}$  isomer. Reduction of the  $^{232}\text{U}$  content, whose gamma and beta radiation dominate over the  $^{233}\text{U}$  chain, is crucial. A measurement time of a few days to weeks is predicted for the isomeric signal to exceed the noise of the Cherenkov background. These measurements are currently performed in our lab.

Another experimental approach consists in driving the transition from the nuclear ground state to the 29 keV level, which is in the same rotational band as the isomer. From there, the probability of populating the isomer is very high. A part of the highly-doped  $^{229/232}\text{Th}:\text{CaF}_2$  will be used for this measurement at the SPring-8 facility in Japan.

Other fluoride crystals, most prominently  $\text{MgF}_2$ , might be an alternative material for thorium-doping. Their material properties, like UV and x-ray transparency, are comparable or even more favorable than those of calcium fluoride. Since scintillation turned out to depend mainly on the host crystal and not on the specific dopant, an improvement of the radioluminescence background could be achieved by the use  $\text{MgF}_2$ , for which the highest-energy peak occurs at  $> 400$  nm, showing a much smaller amplitude than in  $\text{CaF}_2$ . Future investigations will include comparisons of other host crystals with  $\text{CaF}_2$ .





## List of Figures

2.1	Vertical gradient freeze method . . . . .	14
2.2	Czochralski method . . . . .	16
2.3	Numerical simulation of the temperature field and the shape of the phase boundary . . . . .	22
2.4	Thermal insulation of the furnace and crucible . . . . .	23
2.5	Undesired crystallization direction . . . . .	25
2.6	Lower heaters and position of the lower TEs . . . . .	27
2.7	A Horizontal thermoelement . . . . .	27
2.8	Process diagram of a typical $\text{CaF}_2$ growth . . . . .	32
2.9	Crystals grown with a too low axial temperature gradient . . . . .	36
2.10	Undesired growth conditions . . . . .	37
2.11	Cutting marks in the seed crystal . . . . .	41
2.12	Remainder of the sliced seed . . . . .	42
2.13	U: $\text{CaF}_2$ crystal V042 cut into 10 pieces . . . . .	42
3.1	Charge compensation configurations for thorium-doping of $\text{CaF}_2$ . . . . .	48
3.2	Forces acting on the atoms in thorium-doped $\text{CaF}_2$ . . . . .	49
3.3	Charge densities around the dopant side of Th: $\text{CaF}_2$ . . . . .	49
3.4	Density of states of undoped $\text{CaF}_2$ per supercell . . . . .	50
3.5	Density of states for Th-doped $\text{CaF}_2$ with two $\text{F}_i^-$ ions in the $90^\circ$ configuration for charge compensation . . . . .	50
3.6	Density of states for Th-doped $\text{CaF}_2$ with a calcium vacancy for charge compensation . . . . .	51
3.7	Charge compensation configurations in Th: $\text{CaF}_2$ with oxygen present . . . . .	52
3.8	Density of states for with $\text{O}^{2-}$ at an interstitial site . . . . .	52
3.9	Lead from the scavenger process forms a film on the top of a crystal . . . . .	57
3.10	Ce: $\text{CaF}_2$ crystal grown by the Czochralski method . . . . .	59
3.11	Gamma spectrum of $^{233}\text{Pa}$ . . . . .	61
3.12	Gamma spectrum of $^{229}\text{Th}$ . . . . .	63
3.13	Czochralski-grown $^{232}\text{Th}:\text{CaF}_2$ crystal . . . . .	66
3.14	$^{232}\text{Th}$ concentration in V029 . . . . .	68
3.15	$^{232}\text{Th}$ concentration in V034 . . . . .	68
3.16	$^{232}\text{Th}$ concentration in V036 . . . . .	69
3.17	$^{232}\text{Th}$ concentration in V037 . . . . .	69
3.18	$^{232}\text{Th}$ concentration in V038 . . . . .	69
3.19	$^{232}\text{Th}$ concentration in V039 . . . . .	69
3.21	Sample preparation for NAA of the highly-doped $^{232}\text{Th}:\text{CaF}_2$ crystal . . . . .	71

3.22	Highly-doped $^{232}\text{Th}:\text{CaF}_2$ crystal V041 cut for NAA . . . . .	72
3.23	$^{232}\text{Th}$ concentration in V040 . . . . .	72
3.24	$^{232}\text{Th}$ concentration in V041 . . . . .	72
3.25	$^{229}\text{Th}$ concentration in V038 . . . . .	75
3.26	$^{229}\text{Th}$ concentration in V039 . . . . .	76
3.27	Highly-doped $^{229}\text{Th}:\text{CaF}_2$ crystal V057 . . . . .	78
3.28	Polished sample of V057 . . . . .	78
3.29	Zr-doped $\text{CaF}_2$ crystal . . . . .	78
4.1	UV spectrometer for measuring the crystal transmittance . . . . .	85
4.2	Undoped $\text{CaF}_2$ crystals for VUV transmittance measurements . . . . .	88
4.3	Th-doped $\text{CaF}_2$ crystals for VUV transmittance measurements . . . . .	89
4.4	VUV transmittance of undoped $\text{CaF}_2$ crystals . . . . .	89
4.5	VUV transmittance of Th-doped crystals. . . . .	90
4.6	UV Transmission of $^{238}\text{U}:\text{CaF}_2$ . . . . .	92
4.7	Crystal samples used for transmittance measurements . . . . .	93
4.8	Energy-dependent transmittance at 160 nm . . . . .	94
4.9	Crystal luminescence signal after 1 s illumination . . . . .	97
4.10	Temporal evolution of the luminescence of $\text{CaF}_2$ and $^{232}\text{Th}:\text{CaF}_2$ . . . . .	100
4.11	VUV-photoluminescence of $\text{CaF}_2$ . . . . .	101
4.12	Radioluminescence spectra of $^{229}\text{Th}:\text{CaF}_2$ . . . . .	103
4.13	Radioluminescence bursts induced by alpha decay . . . . .	103
4.14	Temperature dependence of $\text{CaF}_2$ luminescence. . . . .	105
4.15	Temperature dependence of radioluminescence in $^{229}\text{Th}:\text{CaF}_2$ . . . . .	106
4.16	Spectrally narrow feature caused by contamination in $\text{CaF}_2$ . . . . .	109

## Bibliography

- [1] L. A. Kroger and C. W. Reich. Features of the low-energy level scheme of  $^{229}\text{Th}$  as observed in the alpha-decay of  $^{233}\text{U}$ . *Nuclear Physics, Section A*, 259(1):29–60, 1976. doi:[10.1016/0375-9474\(76\)90494-2](https://doi.org/10.1016/0375-9474(76)90494-2).
- [2] R. G. Helmer and C. W. Reich. An excited state of  $\text{Th}^{229}$  at 3.5 eV. *Physical Review C*, 49(4):1845–1858, 1994. doi:[10.1103/PhysRevC.49.1845](https://doi.org/10.1103/PhysRevC.49.1845).
- [3] E. Peik and M. Okhapkin. Nuclear clocks based on resonant excitation of  $\gamma$ -transitions. *Comptes Rendus Physique*, 16(5):516–523, 2015. doi:[10.1016/j.crhy.2015.02.007](https://doi.org/10.1016/j.crhy.2015.02.007).
- [4] B. Beck, J. Becker, P. Beiersdorfer, G. Brown, K. Moody, J. Wilhelmy, F. Porter, C. Kilbourne, and R. Kelley. Energy Splitting of the Ground-State Doublet in the Nucleus  $\text{Th}^{229}$ . *Physical Review Letters*, 98(14):1–4, 2007. doi:[10.1103/PhysRevLett.98.142501](https://doi.org/10.1103/PhysRevLett.98.142501).
- [5] B. R. Beck, C. Wu, P. Beiersdorfer, G. V. Brown, J. A. Becker, K. J. Moody, J. B. Wilhelmy, F. S. Porter, A. C. Kilbourne, and R. L. Kelley. Improved Value for the Energy Splitting of the Ground-State Doublet in the Nucleus  $^{229m}\text{Th}$ . In *12th International Conference on Nuclear Reaction Mechanisms*, Varenna, Italy, 2009. Available from: <https://e-reports-ext.llnl.gov/pdf/375773.pdf>.
- [6] G. A. Kazakov, V. Schauer, J. Schwestka, S. P. Stellmer, J. H. Sterba, A. Fleischmann, L. Gastaldo, A. Pabinger, C. Enss, and T. Schumm. Prospects for measuring the  $^{229}\text{Th}$  isomer energy using a metallic magnetic microcalorimeter. *Nuclear instruments & methods in physics research*, 735:229–239, 2014. doi:[10.1016/j.nima.2013.09.012](https://doi.org/10.1016/j.nima.2013.09.012).
- [7] L. von der Wense, B. Seiferle, M. Laatiaoui, J. B. Neumayr, H.-J. Maier, H.-F. Wirth, C. Mokry, J. Runke, K. Eberhardt, C. E. Düllmann, N. G. Trautmann, and P. G. Thirolf. Direct detection of the  $^{229}\text{Th}$  nuclear clock transition. *Nature*, 533(7601):47–51, may 2016. doi:[10.1038/nature17669](https://doi.org/10.1038/nature17669).
- [8] A. D. Ludlow, M. M. Boyd, J. Ye, E. Peik, and P. O. Schmidt. Optical atomic clocks. *Reviews of Modern Physics*, 87(2):637–701, 2015. doi:[10.1103/RevModPhys.87.637](https://doi.org/10.1103/RevModPhys.87.637).
- [9] N. Poli, C. W. Oates, P. Gill, and G. M. Tino. Optical atomic clocks. *arXiv*, page 69, 2014. arXiv:[1401.2378](https://arxiv.org/abs/1401.2378), doi:[10.1393/ncr/i2013-10095-x](https://doi.org/10.1393/ncr/i2013-10095-x).

- [10] F. Riehle. *Frequency standards - Basics and applications*. WILEY-VCH, 2004.
- [11] J.-P. Uzan. The fundamental constants and their variation: observational and theoretical status. *Reviews of Modern Physics*, 75(2):403–455, 2003. doi:10.1103/RevModPhys.75.403.
- [12] V. Flambaum. Enhanced Effect of Temporal Variation of the Fine Structure Constant and the Strong Interaction in Th229. *Physical Review Letters*, 97(9):1–3, 2006. doi:10.1103/PhysRevLett.97.092502.
- [13] J. Berengut, V. Dzuba, V. Flambaum, and S. Porsev. Proposed Experimental Method to Determine  $\alpha$  Sensitivity of Splitting between Ground and 7.6 eV Isomeric States in Th229. *Physical Review Letters*, 102(21):210801, 2009. doi:10.1103/PhysRevLett.102.210801.
- [14] E. V. Tkalya. Proposal for a nuclear gamma-ray laser of optical range. *Physical Review Letters*, 106(16):1–4, 2011. doi:10.1103/PhysRevLett.106.162501.
- [15] T. Bürvenich, J. Evers, and C. Keitel. Nuclear Quantum Optics with X-Ray Laser Pulses. *Physical Review Letters*, 96(14):142501, 2006. doi:10.1103/PhysRevLett.96.142501.
- [16] W.-T. Liao, S. Das, C. H. Keitel, and A. Pálffy. Coherence-Enhanced Optical Determination of the 229Th Isomeric Transition. *Physical Review Letters*, 109(26):262502, dec 2012. doi:10.1103/PhysRevLett.109.262502.
- [17] S. Das, A. Pálffy, and C. H. Keitel. Quantum interference effects in an ensemble of 229Th nuclei interacting with coherent light. *Phys. Rev. C*, 88(2):24601, 2013. doi:10.1103/PhysRevC.88.024601.
- [18] E. V. Tkalya, A. N. Zherikhin, and V. I. Zhudov. Decay of the low-energy nuclear isomer 229Th in solids (dielectrics and metals): A new scheme of experimental research. *Physical Review C*, 61:064308, 2000. doi:10.1103/PhysRevC.61.064308.
- [19] Webpage of the NuClock consortium. Available from: <http://www.nuclock.eu>.
- [20] S. G. Porsev, V. V. Flambaum, E. Peik, and C. Tamm. Excitation of the isomeric Th229m nuclear state via an electronic bridge process in Th+229. *Physical Review Letters*, 105(18):1–4, 2010. doi:10.1103/PhysRevLett.105.182501.
- [21] O. A. Herrera-Sancho, M. V. Okhapkin, K. Zimmermann, C. Tamm, E. Peik, A. V. Taichenachev, V. I. Yudin, and P. Głowacki. Two-photon laser excitation of trapped 232Th+ ions via the 402-nm resonance line. *Physical Review A*, 85(3):1–8, 2012. doi:10.1103/PhysRevA.85.033402.

- [22] O. A. Herrera-Sancho, N. Nemitz, M. V. Okhapkin, and E. Peik. Energy levels of Th<sup>+</sup> between 7.3 and 8.3 eV. *Phys. Rev. A*, 88(1):12512, 2013. doi:[10.1103/PhysRevA.88.012512](https://doi.org/10.1103/PhysRevA.88.012512).
- [23] C. Campbell, A. Steele, L. Churchill, M. DePalatis, D. Naylor, D. Matsukevich, A. Kuzmich, and M. Chapman. Multiply Charged Thorium Crystals for Nuclear Laser Spectroscopy. *Physical Review Letters*, 102(23):3–6, 2009. doi:[10.1103/PhysRevLett.102.233004](https://doi.org/10.1103/PhysRevLett.102.233004).
- [24] C. J. Campbell, A. G. Radnaev, and A. Kuzmich. Wigner crystals of Th229 for optical excitation of the nuclear isomer. *Physical Review Letters*, 106(22):1–4, 2011. doi:[10.1103/PhysRevLett.106.223001](https://doi.org/10.1103/PhysRevLett.106.223001).
- [25] M. S. Safronova, U. I. Safronova, A. G. Radnaev, C. J. Campbell, and A. Kuzmich. Magnetic dipole and electric quadrupole moments of the 229Th nucleus. *Physical Review A*, 88(6):60501, 2013. doi:[10.1103/PhysRevA.88.060501](https://doi.org/10.1103/PhysRevA.88.060501).
- [26] K. Zimmermann. *Experiments Towards Optical Nuclear Spectroscopy With Thorium-229*. PhD thesis, Leibniz Univ. Hannover, 2010. Available from: <http://edok01.tib.uni-hannover.de/edoks/e01dh10/634991264.pdf>.
- [27] J. T. Burke, R. J. Casperson, E. L. Swanberg, and D. Thomas. 229Th the Bridge Between Nuclear and Atomic Interactions. *LLNL-TR-463538*, 2010. Available from: <https://e-reports-ext.llnl.gov/pdf/459955.pdf>.
- [28] X. Zhao, Y. N. Martinez de Escobar, R. Rundberg, E. M. Bond, A. Moody, and D. J. Vieira. Observation of the Deexcitation of the 229mTh Nuclear Isomer. *Physical Review Letters*, 109(16):160801, 2012. doi:[10.1103/PhysRevLett.109.160801](https://doi.org/10.1103/PhysRevLett.109.160801).
- [29] E. Peik and K. Zimmermann. Comment on observation of the deexcitation of the Th229m nuclear isomer. *Physical Review Letters*, 111(018901), 2013. doi:[10.1103/PhysRevLett.111.018901](https://doi.org/10.1103/PhysRevLett.111.018901).
- [30] W. G. Rellergert, D. Demille, R. R. Greco, M. P. Hehlen, J. R. Torgerson, and E. R. Hudson. Constraining the evolution of the fundamental constants with a solid-state optical frequency reference based on the Th229 nucleus. *Physical Review Letters*, 104(20):1–4, 2010. doi:[10.1103/PhysRevLett.104.200802](https://doi.org/10.1103/PhysRevLett.104.200802).
- [31] G. A. Kazakov, A. N. Litvinov, V. I. Romanenko, L. P. Yatsenko, A. V. Romanenko, M. Schreitl, G. Winkler, and T. Schumm. Performance of a 229Thorium solid-state nuclear clock. *New Journal of Physics*, 14(8):083019, 2012. doi:[10.1088/1367-2630/14/8/083019](https://doi.org/10.1088/1367-2630/14/8/083019).
- [32] Alexander Gottwald and Roman Klein and Ralph Müller and Mathias Richter and Frank Scholze and Reiner Thornagel and Gerhard Ulm. Current

- capabilities at the Metrology Light Source. *Metrologia*, 49(2):S146, 2012. Available from: <http://stacks.iop.org/0026-1394/49/i=2/a=S146>.
- [33] R. A. Jackson, J. B. Amaral, M. E. G. Valerio, D. P. DeMille, and E. R. Hudson. Computer modelling of thorium doping in LiCaAlF<sub>6</sub> and LiSrAlF<sub>6</sub>: application to the development of solid state optical frequency devices. *Journal of Physics: Condensed Matter*, 21(32):325403, 2009. doi:10.1088/0953-8984/21/32/325403.
- [34] M. P. Hehlen, R. R. Greco, W. G. Rellergert, S. T. Sullivan, D. DeMille, R. a. Jackson, E. R. Hudson, and J. R. Torgerson. Optical spectroscopy of an atomic nucleus: Progress toward direct observation of the <sup>229</sup>Th isomer transition. *Journal of Luminescence*, 133:91–95, 2013. doi:10.1016/j.jlumin.2011.09.037.
- [35] W. Rellergert and S. Sullivan. Progress towards fabrication of <sup>229</sup>Th-doped high energy band-gap crystals for use as a solid-state optical frequency reference. *IOP Conference Series: Materials Science and Engineering*, 012005, 2010. doi:10.1088/1757-899X/15/1/012005.
- [36] J. Jeet, C. Schneider, S. T. Sullivan, W. G. Rellergert, S. Mirzadeh, A. Casanho, H. P. Jenssen, E. V. Tkalya, and E. R. Hudson. Results of a Direct Search Using Synchrotron Radiation for the Low-Energy <sup>229</sup>Th Nuclear Isomeric Transition. *Physical Review Letters*, 114(25):253001, 2015. doi:10.1103/PhysRevLett.114.253001.
- [37] A. Y. Peik, M. Kolbe, H. Kaser, T. Reichel, A. Gottwald, and E. Experimental search for the low-energy nuclear transition in <sup>229</sup>Th with undulator radiation. *New Journal of Physics*, 17(5):53053, 2015. Available from: <http://stacks.iop.org/1367-2630/17/i=5/a=053053>.
- [38] R. D. Shannon. Revised effective ionic radii and systematic studies of interatomic distances in halides and chalcogenides. *Acta Crystallographica Section A*, 32(5):751–767, 1976. doi:10.1107/S0567739476001551.
- [39] P. Dessovic, P. Mohn, R. A. Jackson, G. Winkler, M. Schreitl, G. Kazakov, and T. Schumm. <sup>229</sup>Thorium-doped calcium fluoride for nuclear laser spectroscopy. *Journal of Physics: Condensed Matter*, 26(10):105402, 2014. doi:10.1088/0953-8984/26/10/105402.
- [40] J. T. Mouhovski. Control of oxygen contamination during the growth of optical calcium fluoride and calcium strontium fluoride crystals. *Progress in Crystal Growth and Characterization of Materials*, 53(2):79–116, 2007. doi:10.1016/j.pcrysgrow.2007.03.001.
- [41] K.-T. Wilke and J. Bohm. *Kristallzüchtung*. Verlag Harri Deutsch, 1988.
- [42] H. J. Scheel. Historical aspects of crystal growth technology. *Jour-*

- nal of Crystal Growth*, 211(1):1–12, 2000. doi:[10.1016/S0022-0248\(99\)00780-0](https://doi.org/10.1016/S0022-0248(99)00780-0).
- [43] G. Tamman. *Lehrbuch der Metallographie*. Leipzig und Hamburg: Leopold Voss, 1914.
- [44] F. Stöber. Künstliche Darstellung großer, fehlerfreier Kristalle. *Z. Kristallogr.*, 61:299–314, 1925.
- [45] J. Obreimov and L. W. Schubnikov. Eine Methode zur Herstellung von Metall-Einkristallen. *Z. Physik*, 25:31–36, 1924.
- [46] F. Bouillon. Note sur la preparation de monocristaux metalliques. *Bull. Soc. chim. Belges*, 60:333–336, 1951.
- [47] P. W. Bridgman. The compressibility of thirty metals as a function of pressure and temperature. *Proc. Amer. Acad. Arts Sci.(Boston)*, 58:165–242, 1923.
- [48] D. C. Stockbarger. The production of large artificial fluorite crystals. *Trans. Faraday Soc.*, 5:294–299, 1949.
- [49] R. Nacken. Über das Wachsen von Kristallpolyedern in ihrem Schmelzfluss. *N. Jb. Mineral. Geol. Paläont. (Stuttgart)*, 2:133–164, 1915.
- [50] S. Kyropoulos. Ein Verfahren zur Herstellung großer Kristalle. *Z. anorg. allg. Chemie*, 154:308–313, 1926.
- [51] J. Czochralski. Ein neues Verfahren zur Messung der Kristallisationsgeschwindigkeit der Metalle. *Z. phys. Chemie*, 92:219–221, 1918.
- [52] W. C. Dash. Silicon crystals free of dislocations. *J. appl. Phys.*, 29:736–737, 1958.
- [53] J. Friedrich, L. Stockmeier, and G. Müller. Constitutional Supercooling in Czochralski Growth of Heavily Doped Silicon Crystals. *Acta Physica Polonica A*, 124(2):219–226, 2013. doi:[10.12693/APhysPolA.124.219](https://doi.org/10.12693/APhysPolA.124.219).
- [54] D. Yongjun, Z. Guoqing, S. Liangbi, Y. Weiqiao, and X. Jun. Growth of CaF<sub>2</sub> block and dome by gradient freeze technique. *Materials Letters*, 58(16):2157–2160, 2004. doi:[10.1016/j.matlet.2004.01.014](https://doi.org/10.1016/j.matlet.2004.01.014).
- [55] C. Chang, V. Yip, and W. Wilcox. Vertical gradient freeze growth of gallium arsenide and naphthalene: Theory and practice. *J. Cryst. Growth*, 22:247, 1974.
- [56] A. Molchanov. *Anlagenentwicklung und experimentelle Untersuchungen zur Züchtung von CaF<sub>2</sub>-Kristallen für die Mikrolithographie*. PhD thesis, Universität Erlangen-Nürnberg, 2005.

- [57] A. Molchanov, U. Hilburger, J. Friedrich, M. Finkbeiner, G. Wehrhan, and G. Müller. Experimental verification of the numerical model for a CaF<sub>2</sub> crystal growth process. *Cryst. Res. Technol.*, 37(1):77–82, 2002. Available from: [http://reichling.physik.uos.de/download{ }paper.php?paper=CrystResTech37p77\(2002\){ }Molchanov.pdf](http://reichling.physik.uos.de/download{ }paper.php?paper=CrystResTech37p77(2002){ }Molchanov.pdf).
- [58] A. Molchanov, O. Graebner, G. Wehrhan, J. Friedrich, and G. Müller. Optimization of the growth of CaF<sub>2</sub> crystals by model experiments and numerical simulation. *Journal of the Korean Crystal Growth and Crystal Technology*, 13(1):15–18, 2003.
- [59] G. Müller and J. Friedrich. Challenges in modeling of bulk crystal growth. *Journal of Crystal Growth*, 266(1-3):1–19, 2004. doi:10.1016/j.jcrysgro.2004.02.024.
- [60] S. Timoshenko and J. N. Goodier. *Theory of Elasticity*. MacGraw - Hill Book Company, Inc., 1982.
- [61] P. Görlich, H. Karras, and R. Lehmann. Über die optischen Eigenschaften der Erdalkalihalogenide vom Flußspat-Typ (I). *Phys. Stat. Sol.*, 1:389–440, 1961.
- [62] T. Tomiki and T. Miyata. Optical Studies of Alkali Fluorides and Alkaline Earth Fluorides in VUV Region. *Journal of the Physical Society of Japan*, 27(3):658–678, 1969. doi:10.1143/JPSJ.27.658.
- [63] G. Varlamov, G. Vasilchenko, V. Deshko, A. Karvatskii, and O. Khlebnikov. Thermophysical and optical properties of fluoride crystals and melts. *High Temperatures-High Pressures*, 21:647–656, 1989.
- [64] M. Modest. *Radiative Heat Transfer*. McGraw-Hill, New York, 1993.
- [65] J. Seebeck. CrysMAS User Manual. Available from: <http://www.iisb.fraunhofer.de/en/research{ }areas/materials/software{ }downloads.html>.
- [66] G. Müller. Experimental analysis and modeling of melt growth processes. *Journal of crystal growth*, 237-239:1628–1637, 2002. doi:10.1016/S0022-0248(01)02356-9.
- [67] P. Boiton, N. Giacometti, J. Sentailler, T. Duffar, and J. Nabot. Experimental determination and numerical modelling of solid–liquid interface shapes for vertical Bridgman grown GaSb crystals. *Journal of Crystal Growth*, 194(1):43–52, 1998. doi:10.1016/S0022-0248(98)00617-4.
- [68] M. Schreitl. Quantummetrology group wiki. Available from: <http://ati238-63.ati.tuwien.ac.at/thorium/doku.php?id=start>.
- [69] A. Molchanov, J. Friedrich, G. Wehrhan, and G. Müller. Study of the



- Oxygen Incorporation During Growth of Large CaF<sub>2</sub>-Crystals. *J. Crystal Growth*, 273:629–637, 2005. doi:10.1016/j.jcrysgr.2004.09.040.
- [70] A. Kaminskii. *Laser Crystals - Their Physics and Properties*. Springer-Verlag Berlin Heidelberg, 1975. doi:10.1007/978-3-540-70749-3.
- [71] P. P. Sorokin and M. J. Stevenson. Stimulated Infrared Emission from Trivalent Uranium. *Physical Review Letters*, 5(12):557–559, 1960. Available from: <http://link.aps.org/doi/10.1103/PhysRevLett.5.557>.
- [72] R. McLaughlin. Optical Spectra of Pu in CaF<sub>2</sub>. *The Journal of Chemical Physics*, 48(3):967, 1968. doi:10.1063/1.1668850.
- [73] L. Su, W. Yang, J. Xu, Y. Dong, and G. Zhou. Optical absorption properties and valence states of uranium in CaF crystals grown by TGT. *Journal of Crystal Growth*, 270(1-2):150–155, 2004. doi:10.1016/j.jcrysgr.2004.06.013.
- [74] J. B. Gruber, D. K. Sardar, L. D. Merkle, B. Zandi, R. Jarman, and J. A. Hutchinson. Spectroscopic properties of CaF<sub>2</sub>:U<sup>4+</sup> as a saturable absorber. *Journal of Applied Physics*, 90(8):3965–3972, 2001. doi:10.1063/1.1396833.
- [75] L. C. Nistor, S. V. Nistor, V. Teodorescu, and I. Voicu. The Distribution of Thorium in Fluorite Single Crystals. *Kristall und Technik*, 14(12):1525–1528, 1979. doi:10.1002/crat.19790141222.
- [76] V. Teodorescu, L. C. Nistor, and S. V. Nistor. Electron microscopy study of pure and doped synthetically grown CaF<sub>2</sub> crystals. *physica status solidi (a)*, 52(2):711–717, 1979. doi:10.1002/pssa.2210520244.
- [77] L. R. Bunney, N. E. Ballou, J. Pascual, and S. Foti. Quantitative Radiochemical Analysis by Ion Exchange. Anion Exchange Behavior of Several Metal Ions in Hydrochloric, Nitric, and Sulfuric Acid Solutions. *Analytical Chemistry*, 31(3):324–326, 1959. Available from: <http://dx.doi.org/10.1021/ac60147a001>, doi:10.1021/ac60147a001.
- [78] S. Stellmer, M. Schreitl, G. Kazakov, J. Sterba, and T. Schumm. Measuring the Th-229 nuclear isomer transition with U-233 doped crystals. *arXiv*, pages 1–12, 2015. arXiv:1511.07187.
- [79] National Nuclear Data Center. Available from: <http://www.nndc.bnl.gov/nudat2/>.
- [80] F. Karpeshin and M. Trzhaskovskaya. Impact of the electron environment on the lifetime of the <sup>229</sup>Thm low-lying isomer. *Physical Review C*, 76(5):1–10, 2007. doi:10.1103/PhysRevC.76.054313.
- [81] E. Browne and J. Tuli. Nuclear Data Sheets for A = 229. *Nuclear Data Sheets*, 109(11):2657–2724, 2008. doi:10.1016/j.nds.2008.10.001.

- [82] L. B. Su, J. Xu, W. Q. Yang, Y. J. Dong, J. Jiang, W. F. Li, G. Q. Zhou, H. J. Li, and J. L. Si. Study on the reduction of uranium and color centers in U:CaF<sub>2</sub> single crystals grown by the temperature gradient technique. *Chemical Physics Letters*, 399(1-3):47–52, 2004. doi:[DOI10.1016/j.cplett.2004.10.001](https://doi.org/10.1016/j.cplett.2004.10.001).
- [83] L. Su, W. Yang, J. Xu, Y. Dong, and G. Zhou. Investigation of multiple centers in U<sup>3+</sup>:CaF<sub>2</sub> single crystals. *Journal of Crystal Growth*, 273:234–240, 2004. doi:[10.1016/j.jcrysgro.2004.08.028](https://doi.org/10.1016/j.jcrysgro.2004.08.028).
- [84] L. Su, J. Xu, Y. Dong, W. Yang, G. Zhou, and G. Zhao. Characteristics and optical spectra of U:CaF<sub>2</sub> crystal grown by TGT. *Journal of Crystal Growth*, 261:496–501, 2004. doi:[10.1016/j.jcrysgro.2003.09.036](https://doi.org/10.1016/j.jcrysgro.2003.09.036).
- [85] J. Korkisch and F. Tera. Anion exchange separation of uranium, thorium and bismuth. *Fresenius' Zeitschrift für analytische Chemie*, 186(2):290–295, 1962. doi:[10.1007/BF00626136](https://doi.org/10.1007/BF00626136).
- [86] G. Jander, E. Schweda, R. Rossi, E. Blasius, and J. Strähle. *Jander/Blasius Lehrbuch der analytischen und präparativen anorganischen Chemie*. Hirzel, Stuttgart, 16 edition, 2006.
- [87] S. Stellmer, M. Schreitl, and T. Schumm. Radioluminescence and photoluminescence of Th:CaF<sub>2</sub> crystals. *Scientific Reports*, 5(15580):1–9, 2015. doi:[10.1038/srep15580](https://doi.org/10.1038/srep15580).
- [88] V. C. Takayuki Yanagida, Kyoung Jin Kim, Kei Kamada, Yuui Yokota, Shuji Maeo, Akira Yoshikawa, Noriaki Kawaguchi, Kentaro Fukuda, Nobuhiko Sarukura. Growth, Optical Properties, and Scintillation Light Yield of CaF<sub>2</sub>:Ce Crystals with Different Ce Concentration. *Japanese Journal of Applied Physics*, 49(3R):32601, 2010. doi:[10.1143/JJAP.49.032601](https://doi.org/10.1143/JJAP.49.032601).
- [89] B. Ullmann. Messung der Transmission von CaF<sub>2</sub> - Kristallen im ultravioletten Bereich - 157 nm, project work, TU Wien, 2011.
- [90] Gamma spectrum of <sup>233</sup>U and daughter nuclei, 2003. Available from: <http://www.radiochemistry.org/periodictable/gamma{ }spectra/pdf/u233.pdf>.
- [91] B. Ullmann. Characterisation of doped CaF<sub>2</sub> crystals towards a solid-state optical clock, diploma thesis, TU Wien, 2012.
- [92] M. Fritthum and A. Sas. Probenpräparation quaderförmiger CaF<sub>2</sub> und <sup>229</sup>Th:CaF<sub>2</sub> Kristalle, bachelor thesis, TU Wien, 2016.
- [93] VUV transmission of calcium fluoride, 2012. Available from: <http://www.crystran.co.uk/optical-materials/calcium-fluoride-caf2>.

- [94] Newport. Optical Materials. Available from: <https://www.newport.com/Optical-Materials/144943/1033/content.aspx>.
- [95] Korth GmbH. Data sheet calcium fluoride. Available from: <http://www.korth.de/index.php/material-detailansicht/items/10.html>.
- [96] C. Goerling, U. Leinhos, and K. Mann. Comparative studies of absorptance behaviour of alkaline-earth fluorides at 193 nm and 157 nm. *Applied Physics B*, 265:259–265, 2002. doi:10.1007/s003400200798.
- [97] C. Goerling, U. Leinhos, and K. Mann. Surface and bulk absorption in CaF<sub>2</sub> at 193 and 157 nm. *Optics Communications*, 249(1-3):319–328, 2005. doi:10.1016/j.optcom.2005.01.027.
- [98] K. Recker and R. Leckebusch. Vapour phase growth of CaF<sub>2</sub> and CaF<sub>2</sub>(U) single crystals. *J. Crystal Growth*, 9:274–280, 1971.
- [99] A. Horowitz, S. Biderman, G. Amar, U. Laor, M. Weiss, and A. Stern. The growth of single crystals of optical materials via the gradient solidification method. *Journal of Crystal Growth*, 85(1-2):215–222, 1987. doi:10.1016/0022-0248(87)90225-9.
- [100] J. Ko, S. Tozawa, A. Yoshikawa, K. Inaba, T. Shishido, T. Oba, Y. Oyama, T. Kuwabara, and T. Fukuda. Czochralski growth of UV-grade CaF<sub>2</sub> single crystals using ZnF<sub>2</sub> additive as scavenger. *Journal of Crystal Growth*, 222(1-2):243–248, 2001. doi:10.1016/S0022-0248(00)00928-3.
- [101] B. E. Kinsman and R. Hanney. Preparation and purification of metal fluorides for crystals and glasses. *Advanced Materials for Optics and Electronics*, 5(2):109–115, 1995. Available from: <http://doi.wiley.com/10.1002/amo.860050207>, doi:10.1002/amo.860050207.
- [102] H. Guggenheim. Growth of Highly Perfect Fluoride Single Crystals for Optical Masers. *Journal of Applied Physics*, 34(8):2482, 1963. doi:10.1063/1.1702768.
- [103] R. Pastor and K. Arita. Crystal growth of alkaline earth fluorides in a reactive atmosphere. *Materials Research Bulletin*, 10(6):493–499, 1975. doi:10.1016/0025-5408(75)90173-7.
- [104] Mikhail Polyanskiy. Refractive index database. Available from: <http://refractiveindex.info>.
- [105] K. Vogler, I. Kluft, T. Schroeder, U. Stamm, and K. Mann. Long-term test and characterization of optical components at 193 nm and 157 nm. *Proceedings of SPIE*, 4102(2000):255–260, 2000. Available from: <http://proceedings.spiedigitallibrary.org/proceeding.aspx?articleid=916562>.

- [106] S. B. Utter, P. Beiersdorfer, A. Barnes, R. W. Lougheed, J. R. Crespo López-Urrutia, J. A. Becker, and M. S. Weiss. Reexamination of the Optical Gamma Ray Decay in  $^{229}\text{Th}$ . *Phys. Rev. Lett.*, 82(3):505–508, 1999. doi:[10.1103/PhysRevLett.82.505](https://doi.org/10.1103/PhysRevLett.82.505).
- [107] R. W. Shaw, J. P. Young, S. P. Cooper, and O. F. Webb. Spontaneous Ultraviolet Emission from  $^{233}\text{Uranium}$  /  $^{229}\text{Thorium}$  Samples. *Phys. Rev. Lett.*, 82(6):1109–1111, 1999. doi:[10.1103/PhysRevLett.82.1109](https://doi.org/10.1103/PhysRevLett.82.1109).
- [108] W. A. Hargreaves. Optical spectra of  $\text{U}^{2+}$ ,  $\text{U}^{3+}$  and  $\text{U}^{4+}$  ions in calcium fluoride crystals. *Phys. Rev. B*, 44(10):5293–5295, 1991. doi:[10.1103/PhysRevB.44.5293](https://doi.org/10.1103/PhysRevB.44.5293).
- [109] O. Kittelmann and J. Ringling. Intensity-dependent transmission properties of window materials at 193-nm irradiation. *Optics Letters*, 19(24):2053–2055, 1994. doi:[10.1364/OL.19.002053](https://doi.org/10.1364/OL.19.002053).
- [110] S. A. Slattery and D. N. Nikogosyan. Two-photon absorption at 211 nm in fused silica, crystalline quartz and some alkali halides. *Optics Communications*, 228(1–3):127–131, 2003. doi:<http://dx.doi.org/10.1016/j.optcom.2003.09.086>.
- [111] D. J. Huntley. An explanation of the power-law decay of. *Journal of Physics: Condensed Matter*, 18:1359–1365, 2006. doi:[10.1088/0953-8984/18/4/020](https://doi.org/10.1088/0953-8984/18/4/020).
- [112] M. Beutler, M. Ghotbi, F. Noack, and I. V. Hertel. Generation of sub-50-fs vacuum ultraviolet pulses by four-wave mixing in argon. *Optics letters*, 35(9):1491–1493, 2010. doi:[10.1364/OL.35.001491](https://doi.org/10.1364/OL.35.001491).
- [113] C. Tscherne. Untersuchung strahlungsinduzierter Lumineszenz reiner und Th-dotierter  $\text{CaF}_2$ -Kristalle im UV-Bereich, diploma thesis, TU Wien, 2014.
- [114] P. Rodnyi. *Physical Processes in Inorganic Scintillators*. CRC Press, 1997.

# Curriculum vitae

## Matthias Schreitl

born: 23.12.1984  
in Mistelbach  
Nationality: Austria  
Address: Neustiftgasse 108/31  
1070 Vienna  
Email: matthias.schreitl@gmail.com

### EDUCATION

- 2011 Admission to the **Vienna Doctoral Program on Complex Quantum Systems (CoQuS)**
- since 2010 PhD position at the Institute of Atomic and Subatomic Physics, Vienna University of Technology,  
topic: *Growth and characterization of (doped) calcium fluoride crystals for the nuclear spectroscopy of Th-229*,  
Supervision: Univ. Prof. Dr. Thorsten Schumm
- 2010 **Diploma in Technical Physics**  
at the Vienna University of Technology
- 2009 to 2010 Diploma thesis at the Institute of Atomic and Subatomic Physics, Vienna University of Technology,  
topic: *Creating and purifying ultracold degenerate gases using hyperfine transitions*,  
Supervision: Prof. Hannes-Jörg Schmiedmayer
- 2003 to 2010 Technical Physics study  
at the Vienna University of Technology  
(interrupted for 1 year of national civilian service),  
additional courses attended in Biology at the University of Vienna
- 2003 **Diploma from Austrian secondary school**  
qualifying for university admission

## STAYS ABROAD

- 10-11/2015 **University of Michigan, Ann Arbor (USA)**  
Laboratory work on ion trapping of  $^{229}\text{Th}^{3+}$   
in the group of Prof. Alex Kuzmich
- 01-02/2013 **Fraunhofer IISB Erlangen**  
05/2012 Setup and initial operation of the furnace for crystal growth,  
01/2012 Training for the growth of calcium fluoride crystals
- 10/2011 **Max-Born-Institut für Nichtlineare Optik  
und Kurzzeitspektroskopie, Berlin**  
Measurement of luminescence and transmission properties  
of (thorium-doped) calcium fluoride crystals  
under pulsed UV laser radiation  
(Project: LASERLAB-Europe)
- 2008/2009 **EPFL, Lausanne (Switzerland)**  
Semester abroad (Erasmus student exchange)

## LIST OF PUBLICATIONS

- S. Stellmer, M. Schreitl, G. Kazakov, J. Sterba, T. Schumm:  
*Measuring the  $^{229}\text{Th}$  nuclear isomer transition with  $^{233}\text{U}$ -doped crystals*,  
arXiv: 1511.07187 (2015), to be published in Phys. Rev. A.
- S. Stellmer, M. Schreitl, T. Schumm:  
*Radioluminescence and Photoluminescence of  $\text{Th}:\text{CaF}_2$  crystals*  
Scientific Reports, 5:15580 (2015).
- P. Dessovic, P. Mohn, R. Jackson, G. Winkler, M. Schreitl, G. Kazakov, T.  
Schumm:  *$^{229}\text{Th}$  Thorium-doped calcium fluoride for nuclear laser spectroscopy*,  
Journal of Physics: Condensed Matter, 26 (2014), 1054021 - 1054029.
- M. Gring, M. Kuhnert, T. Langen, T. Kitagawa, B. Rauer, M. Schreitl, I. Mazets,  
D. A. Smith, E. Demler, H.-J. Schmiedmayer:  
*Relaxation and Prethermalization in an Isolated Quantum System*,  
Science, 337 (2012), 1318 - 1322.
- G.A. Kazakov, A. Litvinov, V. Romanenko, L. Yatsenko, A. Romanenko, M.  
Schreitl, G. Winkler, T. Schumm:  
*Performance of a  $^{229}\text{Th}$  Thorium solid-state nuclear clock*,  
New Journal of Physics, 14 (2012), 083019.